MEASURING AND EVALUATING PROGRESSIVE EPOXY DEBONDING IN BONDED INSULATED RAIL JOINTS

BY

DANIEL CHARLES PELTIER

B.S.E., Princeton University, 1998

THESIS

Submitted in partial fulfillment of the requirements
for the degree of Master of Science in Civil Engineering
in the Graduate College of the
University of Illinois at Urbana-Champaign, 2008

Urbana, Illinois

Adviser:

Associate Professor Christopher P. L. Barkan

ABSTRACT

Deterioration and failure of bonded insulated rail joints (IJ's) under heavy axle loads impose high costs on North American railroads. Many IJ failures are preceded by the loss of a portion of the epoxy bond that holds the joint bars to the rails. This deterioration, referred to here as "progressive epoxy debonding", begins near the center of the joint and spreads outward with time and traffic. Progressive epoxy debonding reduces the IJ's longitudinal strength and vertical stiffness, contributing to problems such as insulator wear, ballast and subgrade degradation, increased dynamic loads, and cracks in the rail or joint bar.

This thesis describes laboratory experiments performed on a set of IJ's that had varying amounts of progressive epoxy debonding, with the goal of providing knowledge that would be useful for maintenance planning. Greater understanding of IJ degradation and improved techniques for measuring IJ condition would allow a better balance of three important goals: replacing failing IJ's before they create a safety hazard or operational disruption, extracting maximum use from each IJ before its replacement, and scheduling maintenance activities to optimize the use of labor and track time.

The debonded regions of the test IJ's were examined visually by disassembling the joints, and typical geometric characteristics of the region were noted. On average, the specimens had more extensive debonding on the upper and lower portions of the rail / joint-bar interface than along the web of the rail. The debonded area on the field and

gauge sides was generally about equal, but one rail end typically had more debonding than the other.

The accuracy of several techniques for estimating the debonded area of an in-track IJ was also evaluated. One technique, based on visual inspection of the exterior of the joint, is already used in practice but had not been formalized and quantified. It was shown to be capable of producing reasonably accurate results, if implemented properly. Another approach was developed that uses information on the deformation of the joint under longitudinal loads to infer the extent of debonding. Finite element analysis suggested that a small amount of deformation data, collected with wireless strain gauges and extensometers, could be used to implement a fully automated, continuous monitoring system, but laboratory experiments show that further work would be needed to achieve satisfactory accuracy.

Finally, the vertical stiffness of deteriorating IJ's was studied in some detail. A statistical model of the relationship between the size of the debonded area and the static vertical stiffness of the joint was developed by matching laboratory test data to a simple "rotational spring" model of rail joint functionality. Additionally, a tendency of IJ's to stiffen under high applied bending loads was noted, investigated, and attributed to compressive forces developing in the rail heads and endpost.

The ability to measure debonding to a known degree of accuracy, and an understanding of the effect of debonding on IJ performance, will improve railways' ability to monitor the condition of in-track IJ's and replace deteriorating ones at an appropriate time.

To Carrie

ACKNOWLEDGEMENTS

The research described in this thesis was conducted under the auspices of the Railroad Engineering Program in the Department of Civil and Environmental Engineering. It was funded in part by a Strategic Research Initiative grant from the Association of American Railroads. In addition, my first year of study was supported by a CN Research Fellowship in Railroad Engineering. This endowed fellowship, which is not linked to any sponsored research projects, has been critical in several recent research projects, including this one. It has allowed students, particularly new ones, time to discover interesting problems and define an approach before applying for project funding.

Dr. Christopher P. L. Barkan, Associate Professor and George Krambles Faculty Fellow, served as my graduate adviser. As is typically the case, he was instrumental in making this research possible. He deserves particular credit for allowing his students to pursue their interests, even when those interests lead outside of his principal research focuses.

Most of the laboratory work for this project was conducted at the Newmark Structural Engineering Laboratory (NSEL). Dr. Grzegorz Banas, Laboratory Coordinator, assisted in the design of the testing equipment and instrumentation. The Civil and Environmental Engineering Machine Shop, under Supervisor Timothy Prunkard, constructed the test frames, built the necessary fixtures, cut and drilled the test specimens as necessary, and provided various other services throughout.

John Zeman, currently a graduate student in the Railroad Engineering Program, assisted in instrumenting test specimens for these experiments, while pursuing his Bachelor's degree. Graduate students Benjamin Freid, Darwin Shafer, and Athaphon Kawprasert aided in various field activities. Other graduate and undergraduate students affiliated with the Railroad Engineering Program offered valuable insight and criticism at various points throughout the life of the project. Kim Hagemann, Railroad Program Coordinator, handled the formal thesis review and deposit process after I left campus.

This research was originally conceived as an investigation of railroad applications for low-cost, wireless engineering sensors (described in Chapter 3). Dr. Stephen Downing, Lecturer, and Dr. Darrell Socie, Professor Emeritus, both of the Department of Mechanical Science and Engineering, were the lead researchers on this sensor technology. They also provided expertise on the more general subject of instrumentation systems.

From industry, David Davis of the Transportation Technology Center, Inc. (TTCI) stands out for his contribution. Mr. Davis, along with his colleague Muhammad Akhtar, provided enormous amounts of technical information and advice on the subject of insulated rail joints and track maintenance in general. TTCI also provided the two unused insulated joints that served as control specimens in these tests.

W. Thomas Urmson and Patrick Boario of Portec Rail Products, Inc., along with Sidney Shue of and Korhan Ciloglu of L.B. Foster, provided critical technical information on the insulated joints studied.

Various railroaders assisted in the acquisition of test specimens: T. Brian Matthews of the Norfolk Southern Railway; Henry Lees, John Bosshart, Thomas O'Connor, Travis J. Roma, and John Bainter of the BNSF Railway; Ken Lewis, Edward Sparks, Gale Free, and Raymond Zenisek of CSX Transportation; and John Tuckett, then with CN. Many of these people also provided valuable insight into the practice of insulated joint maintenance. Additionally, Samuel Risley, Edward Lange, and Ralph Claypool of the Norfolk Southern Railway assisted in field investigations related to this research.

My new daughter Lucy contributed highly vocal feedback on the writing process itself, and provided a welcome distraction from the stressful endgame.

Most critically, my participation in railroad engineering research would have been impossible without the generous and selfless cooperation of my wife Carrie, who agreed with some reluctance to let me pursue this particular passion, but provided vital and sincere support once the decision was made.

TABLE OF CONTENTS

LIST OF FIGURES

LIST OF TABLES

CHAPTER 1: INTRODUCTION

Deterioration and failure of bonded insulated rail joints (IJ's) impose substantial costs on North American railroads. On lines with heavy axle loads and high tonnage, IJ's have shorter service lives than any other track component except high-angle crossing diamonds (Davis et al. 2005). The direct costs of IJ replacement are high, but the indirect cost of taking busy mainline track out of service for maintenance may be even more important. On the other hand, a deteriorating IJ that is not replaced in a timely manner creates the potential for intermittent, fail-safe malfunctions in the signaling system, or even a derailment. Understanding when to replace a deteriorating IJ therefore is important for the safety and serviceability of the railroad, as well as the efficiency of maintenance operations.

There are three priorities to be considered when scheduling IJ replacement:

1.) To minimize direct cost, IJ's should not be replaced if they are not close to failure.
2.) To minimize indirect cost, deteriorating IJ's should be replaced before they disrupt railroad operations.
3.) To minimize both direct and indirect costs, replacement should be scheduled in advance so as to optimize the use of track time and labor.

These priorities tend to conflict when planning maintenance. However, better information may enable improved decisions and a more efficient balance. For instance, better knowledge about the probability that a certain IJ will fail would help railroad

managers identify the point at which the risk of disruptive failure outweighs the cost of replacement.

Previous work on insulated joints has tended to focus on understanding the causes of deterioration within a joint (e.g. Kabo et al. 2006, Himebaugh et al. 2007, Nicoli et al. 2007) or designing a joint with a longer service life (e.g. Plaut et al. 2007, Akhtar and Davis 2006 and 2007, Davis et al. 2007). The experiments described in this thesis instead examined the effect of a common form of deterioration on the behavior of an existing, widely-used joint design. While this information may contribute to a better understanding of the causes of deterioration, and thereby aid in the search for improved designs, the primary focus is on developing information about current IJ designs and enabling better maintenance practices.

1.1 Rail joints, insulated joints, and bonded insulated joints

Railroad track performs best when there is a smooth, level interface between the wheels and rail. Any localized variation in the running surface excites the train / track system, generating dynamic forces that may damage the wheels and / or track.

For well over a century, the most common discontinuity in the smooth running surface of the rail was the rail joint, where two pieces of rail are joined end-to-end. Kerr (2003) gives a concise history of changes in rail joint design; in modern times, almost all have been of the double-lap joint design, with a pair of splice bars bolted to the two rail sections (Figure 1.1). These bars are variously referred to as “joint bars”, “fish plates”, or, for certain designs, “angle bars”.

Figure 1.1: Typical bolted rail joint.

Bolted rail joints require extensive maintenance for several reasons. First, wear on the interfaces between rail and joint bar causes loss of bolt tension and necessitates regular tightening of the nuts (Hay 1982). Second, each joint forms a point of low bending stiffness in the rail. Since the rail acts as a beam to distribute wheel loads over several crossties, a point of low rail stiffness tends to concentrate loads on the ties near that point (AREA 1980). The increased deflection at the joint may also contribute to the development of low-frequency dynamic loads, as wheels move down at the joint and then back up to the normal loaded elevation of the rail. This effect will be magnified if the increased tie loads lead to greater settlement or loss of elastic stiffness in the ballast and subgrade under the joint. Finally, the small gap between one rail and the other creates high-frequency impact loads as wheels pass over it. These impacts cause high stresses in the rail, especially in the rail head and near the bolt holes, which promote crack initiation and growth. Impacts also tend to cause plastic deformation of the rail head at the gap,

which creates a localized “dip” in the running surface and further increases dynamic loads (Jenkins et al. 1974).

These problems led to the widespread adoption of continuously welded rail (CWR), in which adjacent rail sections are welded together with no mechanical joint. However, the most commonly used traffic-control systems in North America rely on various kinds of DC and coded-DC track circuits to detect the presence of a train within a signal block. The boundaries between blocks are defined by a pair of “insulated joints”, one on each rail. Each IJ consists of two rails joined end-to-end but separated with electrical insulation. The insulation prevents the flow of electric current from one rail to the other, separating the adjacent track circuits. (Insulated joints are also used for the train detection circuits of some highway-grade-crossing active warning devices, although IJ-free grade-crossing circuits are available and widely used on mainline track.)

The need for IJ’s is the principal reason that a large number of rail joints remain in mainline track in North America and other regions that use similar track circuits. Bolted joints installed temporarily as part of certain maintenance procedures are also common, but are generally removed before deterioration becomes problematical.

Before the adoption of CWR, the most common insulated joint designs were similar to a typical bolted rail joint, except that various kinds of insulating material were inserted to prevent electricity from flowing between the steel components (Figure 1.2). A solid insulator called an “endpost” was inserted between the two rail ends. Other kinds of polymer, fabric, or composite insulators were used to separate the rails, joint bars, and track bolts, thus preventing the electrical current from taking an alternate path from one

rail, through the joint bars, and into the other rail (Hay 1982). These joints were subject to the same problems as a non-insulated bolted joint, plus additional failure modes related to worn or cracked insulators.

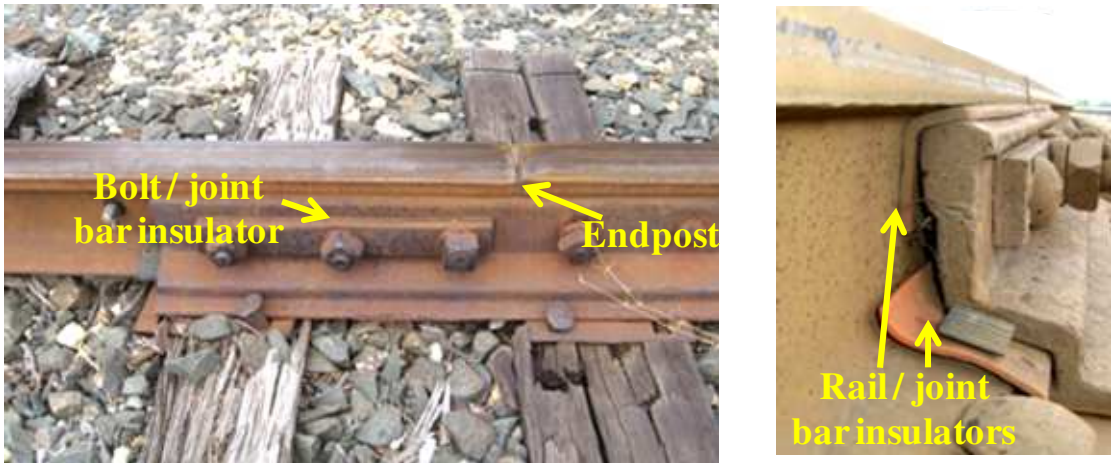

(a) (b)

Figure 1.2: Typical bolted insulated joint. (a) Side view, showing endpost (insulator between rails) and insulator between bolts and joint bars. (b) End view, showing insulator between rail and joint bar.

The adoption of CWR led to further problems with IJ's. Bolted joints allow for some thermal expansion and contraction in the rail, relieving some of the stress that would develop in a fully restrained rail. The elimination of non-insulated joints created higher rail longitudinal forces. These longitudinal forces caused new failure modes to appear in the remaining, insulated joints.

To reduce problems at insulated joints in CWR, the "bonded insulated joint" was developed (Figure 1.3). This type of joint is similar to a traditional insulated joint: a solid endpost (usually fiberglass) separates the rail ends, the bolts are separated from the rail

by insulating bushings, and the rails are separated from the joint bars by a woven fiber fabric. However, in a bonded joint, the insulating fabric is glued to the rails and the joint bar with a strong epoxy. The bolts remain, but their previous function – to hold the joint bars to the rails – is accomplished by the epoxy bond. This relatively small change greatly affects the mechanics of the joint. In a bolted joint, resistance to shear along the rail / joint-bar interface comes from friction, with the normal stress provided by the pretension in the bolts. When friction is inadequate to resist the shear load, shear stresses develop in the bolts themselves. In a bonded joint, shear stresses are transferred between rail and joint bar via the epoxy. This results in joints that deform much less under high longitudinal loads, with several important benefits:

Figure 1.3: Typical bonded insulated joint.

1.) The occurrence of broken bolts is reduced, because the bolts are not subjected to large shear stresses.
2.) Reactive forces do not develop at the bolt holes in the rails or joint bars, reducing the occurrence of bolt-hole cracks.
3.) The rail gap size stays approximately constant, rather than becoming very wide, which could lead to higher impact loads, or very narrow, which could squeeze the endpost and increase the possibility of electrical contact between the rail ends.

Additionally, the transfer of shear stress through an epoxy bond, rather than through friction, reduces the wear on both the insulator and the metal surfaces. In a perfectly-functioning bonded joint, the insulator will not wear out and the bolts will maintain their pretension, greatly reducing routine maintenance requirements.

1.2 Insulated joints in heavy-axle load service

A bonded joint's increased resistance to shear deformation between the rail and joint bar also contributes to the vertical bending stiffness of the joint. Bonded IJ's are often stiffer than bolted, non-insulated joints, even though the joint bars used in a bonded IJ have a different shape and a lower moment of inertia (Cox 1993) (Figure 1.4). (Joint bars in a bolted joint have an approximately symmetrical section in order to reduce out-of-plane bending deformation, while the bars in a bonded joint fit against the rail web to maximize the bond surface.) Nonetheless, a bonded IJ still has less vertical stiffness than a weld and constitutes a discontinuity in the running surface. A wheel passing over an IJ is likely to

cause both high- and low-frequency dynamic loads, which can damage the joint itself or the track substructure. Furthermore, the epoxy is subject to deterioration that can reduce its effectiveness.

(a) (b)

Figure 1.4: Joint bar sections. (a) Bolted joint. (b) Bonded insulated joint.

Davis et al. (2005) found that the average service life of IJ's North American heavy haul railroads is shorter than any other component of the track system except high-angle crossing diamonds. "On high tonnage routes, bonded IJ's may be replaced within as little as 12 to 18 months with direct costs of thousands of dollars per mile per year," and even higher indirect costs due to service disruptions while the joints are replaced. Failure mode analysis revealed that many failed IJ's suffered from more than one type of

damage, including loss of insulating ability, cracked bolts, battered rail ends, and cracked joint bars. It was also noted that local problems with track support, such as fouled ballast, often occurred near insulated joints in track that had otherwise good substructure. This was attributed to both high dynamic loads and increased track deflection.

1.3 Progressive epoxy debonding

Davis et al. (2005) also observed that many of the failed bonded IJ's suffered from a problem that is variously described as "debonding" or "unzipping", and will be referred to in this thesis as "progressive epoxy debonding". This deterioration occurs when the bond between the epoxy and metal fails over a part of the rail / joint-bar interface, so that the insulator is no longer fully bonded to the rail and / or joint bar. In the region of debonding, shear stresses are not transmitted as effectively between the rail and the joint bars. Because the metal surfaces are no longer sealed by the epoxy, they may begin to oxidize; the rust that forms may create internal stresses that could further damage the bond in the region. Debonding was referred to as the first step in the "most typical failure scenario of bonded IJ's in HAL service."

Progressive epoxy debonding usually begins near the center of the joint, adjacent to the endpost. With continued wheel loadings and environmental exposure, the debonded area tends to grow, spreading out towards the ends of the joint bars. As it grows, the stiffness of the joint in response to vertical loads decreases, allowing greater relative displacement between components. The insulators may degrade, contributing to electrical failure. Furthermore, the loss of bond surface decreases the longitudinal

strength of the joint. Extensive debonding and high longitudinal loads can cause the remaining bond to rupture, leaving what is essentially a traditional bolted insulated joint. This condition is sometimes referred to as a "pull-apart", because the lack of an epoxy bond allows the rails to slip relative to the joint bars; the slippage is usually only enough to engage the bolts, but it can be seen with the naked eye. In this thesis, such a condition is referred to as "complete failure of the epoxy bond". Joints with complete epoxy failure are subject to all of the problems described above for bolted joints, such as wide rail gaps, broken track bolts, and bolt-hole cracks. In fact, they may be weaker than a conventional bolted joint, because the shape of the joint bar is optimized for maximizing the bond surface rather than for sustaining contact loads (Figure 1.4).

1.4 Evaluating and measuring epoxy debonding

There have been a number of proposals for improving the service life of bonded IJ's in heavy haul service, including changes in joint materials, joint bar shape, rail gap size and shape, and track support. Many of these show promise (Akhtar and Davis 2007, Davis et al. 2007). Nonetheless, deterioration of insulated joints remains a common problem. Railroads need information and tools to help them manage the problem in such a way as to reduce disruptive failures while still extracting maximum service life from each joint.

This thesis includes several investigations into fundamental questions about progressive epoxy debonding. Chapter 2 describes an empirical investigation into the shape of the debonded region. The results show that debonding is often more extensive towards the upper and lower edges of the rail / joint-bar interface than at the bolt line, and

that debonding is not equally extensive on all four rail / joint-bar interfaces within a joint. This information is important for understanding how debonding progresses, how it might affect the strength of the joint, and how to model the mechanical effects of the deterioration.

The remainder of Chapter 2 and all of Chapters 3 and 4 address the question of how to measure the size of the debonded area in a joint. Measurement is critical both for identifying developing problems in the field and for future studies of how deterioration progresses over time. In Chapter 2 I test existing visual methods for quantifying debonding, identify the most accurate method, and calculate its expected accuracy. Chapter 3 describes a proposed technique for estimating the debonded area with data from simple engineering sensors such as strain gauges and extensometers. Finite element modeling is used to formulate a theoretical basis for this technique. In Chapter 4 I test this theory in the laboratory, calculate the accuracy of the proposed technique, and suggest revisions and improvements that could be applied to future efforts. Together these chapters describe several tools, ranging from simple but labor-intensive to sophisticated and automated, that can be used to quantify the condition of the epoxy bond in an IJ with progressive debonding.

If the amount of debonding in a joint is known and the progression of debonding can be predicted, the question still remains of how much debonding should be tolerated before a joint is replaced. Chapter 5 addresses one part of this question by quantifying the effects of debonding on the vertical stiffness of an IJ. Laboratory tests are used to derive a mathematical correlation between debonding and stiffness. An existing analytic model

by Cox (1993) is adapted to demonstrate the effects of this loss of stiffness on several important quantities such as the maximum tie load under a joint.

The final chapter addresses several broad conclusions that can be drawn from this research and proposes additional studies that would further improve railroads' ability to manage the problem of bonded IJ deterioration.

CHAPTER 2: CHARACTERIZATION OF DEBONDED REGIONS AND TESTING OF VISUAL INSPECTION TECHNIQUES

2.1 Introduction

Modeling the effects of progressive epoxy debonding on bonded insulated joints (IJ's), either mechanistically or empirically, requires an ability to characterize typical IJ debonding conditions. This ensures that the model has the parameters necessary to reflect the variability of the physical system. Furthermore, the application of such models in railway maintenance requires a non-destructive way to assess the actual condition of each particular joint.

This chapter describes a visual analysis of IJ's with varying amounts of epoxy debonding. The purpose of this investigation is to answer several questions that have not been adequately addressed in the published literature:

1.) What is the typical shape of the debonded region? How does it vary within a given IJ and across a set of IJ's?
2.) Can visual inspection of the exterior of an intact IJ yield accurate information about the state of the epoxy bond on the hidden, interior surfaces? If so, what metrics should be used, and how should they be interpreted?

The first question has been addressed previously in general terms. Davis et al. (2005) conducted an investigation of IJ failure modes based on destructive disassembly of failed joints. They reported that epoxy debonding typically begins near the endpost and, over time, spreads outward towards the ends of the joint bars. However, they did not quantitatively describe the size or shape of the debonded region.

The second question is one that has also been considered in practice but not in any published studies that I am aware of. Railroaders and suppliers have noticed certain visual cues that indicate when an IJ is deteriorating, and have developed empirical rules using those cues as the basis for maintenance procedures. Quantification of the relationship between visual cues and objective measures of debonding will contribute to the scientific and engineering understanding of IJ's and development of improved designs and maintenance practices.

In this study, insulated joints with varying degrees of epoxy debonding were collected, measured and analyzed, and then disassembled in order to directly view the condition of the epoxy bond. The data were analyzed to quantify the shape of a "typical" debonded region and the variability between different joints. Additionally, the accuracy of one commonly used visual method for estimating debonding was tested.

2.2 Methodology

Test specimens

A set of insulated joints, including a short section of the rail on either side of the joint, were obtained from various Class 1 North American railroads and suppliers. Two of these were new, unused, factory-manufactured IJ plugs, referred to here as the "control specimens". These were assumed to have no epoxy debonding. A number of other IJ's were obtained from four Class I railroads. These joints had been subject to unknown amounts of traffic before being removed from track for unknown reasons. Six of these were selected (the "test specimens") based on visual indications suggesting varying

amounts of epoxy debonding. Of these six test specimens, four had been in service in the Illinois / Indiana region of the United States, while two came from a high-tonnage coal line in the western United States.

The control specimens came from two suppliers, and consequently had different joint bar sections. The joint bar length and bolt spacing for both designs were identical. The six test specimens each had a joint bar that matched one or the other control specimen. All samples used RE136 rail, except for one test specimen that had RE132 rail (AREMA 2000b). These two rail sections are similar enough that the joint bars on the smaller specimen were the same as the other specimens from that supplier. The slight difference in rail section is not considered important for this research.

The total area of the rail / joint-bar interfaces was 314,000 mm^2 for Supplier A and 322,000 mm^2 for Supplier B.

The specimens were labeled as follows:

- The first letter (C or T) indicates whether the specimen is a control (unused) or test (deteriorated) joint.
- The second letter (A or B) indicates the supplier. This determines both the shape of the joint bar and the insulator / epoxy materials used in its construction.
- A one-digit number differentiates between test specimens from the same supplier. Thus, TA2 indicates the second test specimen from supplier A.

The eight specimens included one control and three test specimens from each supplier. The two control specimens are referred to as CA1 and CB1, and the six test specimens were labeled TA1, TA2, TA3, TB1, TB2, and TB3.

Visual inspection

The most widely used method for detecting epoxy debonding in a bonded IJ is visual inspection of the joint's exterior. The FRA requires visual inspections of all rail joints in continuously welded track at least two to four times per year depending on traffic (CFR 2007a). These inspections must look for any of the following problems or symptoms:

1.) Visible cracks in the joint bar.
2.) Loose, bent, or missing bolts.
3.) Excessive rail end batter or rail end mismatch.
4.) Excessive longitudinal rail movement in or near the joint, "including but not limited to; wide rail gap, defective joint bolts, disturbed ballast, surface deviations, gap between tie plates and rail, or displaced rail anchors."

In a bonded insulated joint, "excessive longitudinal rail movement" is also an indication of complete epoxy failure on at least two of the four rail / joint-bar interfaces, which allows the rail to slip relative to the joint bars by an amount equal to the play in the bolt holes. This situation is undesirable, as the system is not designed to carry loads in this manner. Repeated loadings under these conditions may cause insulation failures, broken bolts, and bolt-hole cracks.

If the rail is in tension when the IJ is inspected, the clearest symptom of a complete bond failure is a loose endpost and a wide gap between the rail ends (Figure 2.1a). Another symptom is an obvious longitudinal shift in the position of the end of the joint bar relative to the rail (Figure 2.1b). None of the six test specimens analyzed in this

chapter showed any such symptoms, indicating that they had experienced progressive debonding but not complete epoxy failure.

(a)

(b)

Figure 2.1: Visual signs of a complete epoxy failure. (a) Wide rail gap. (Note that bond wires were added after the joint failed, in order to prevent intermittent signal disruptions.) b) Movement of joint bar end relative to rail.

Most railroads have inspection programs for mainline insulated joints that exceed FRA requirements. Signal maintainers generally conduct inspections every 30 to 90 days. The American Railway Engineering and Maintenance-of-Way Association (AREMA) publishes a recommended practice for visual inspection of bonded IJ's that includes looking for:

1.) Metal flow across the endpost.

2.) Reversed spike heads.

3.) Missing, cracked, worn, or broken insulation. (AREMA 2000a)

Unfortunately, most of the insulation in a bonded IJ is hidden between the rails and the joint bars. Only the top and bottom edges of the insulator / epoxy layer are visible, between the top of the joint bar and the rail head or the bottom of the joint bar and the rail base.

Despite this limitation, the bead of excess epoxy and the small section of the epoxy / insulator layer visible along the top of the joint bar provides useful information about progressive epoxy debonding on the interior surfaces. The outer edge of the bond layer near the endpost appears to pull away and break off from the joint as the interior surfaces debond. This exterior separation is probably a symptom rather than a direct cause of the deterioration on the interior surfaces, although it is possible that loose edges allow more water to penetrate into the joint. All six test specimens had at least some amount of damage to the upper edge of the insulator layer.

In this investigation, damage to the edge of the insulator and to the bead of excess epoxy was classified into two types: missing and loose (Figure 2.2).

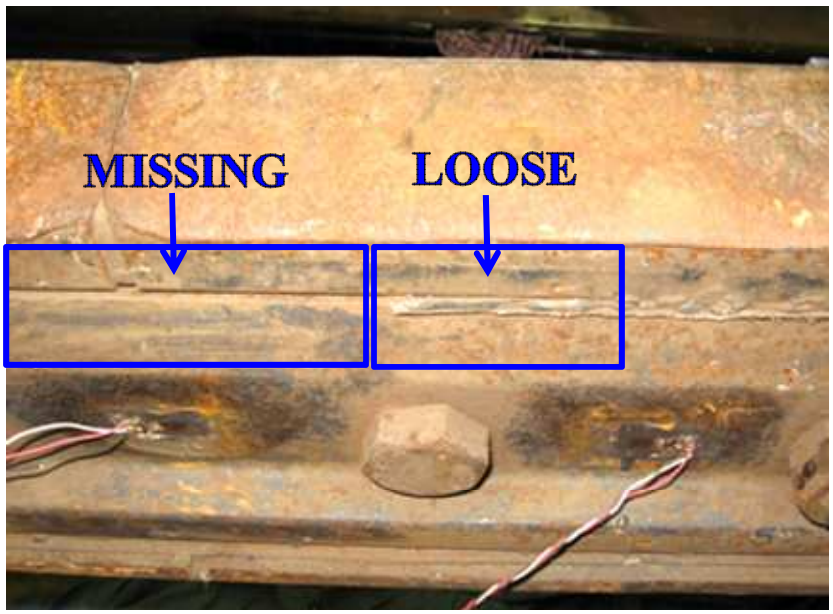

(a)

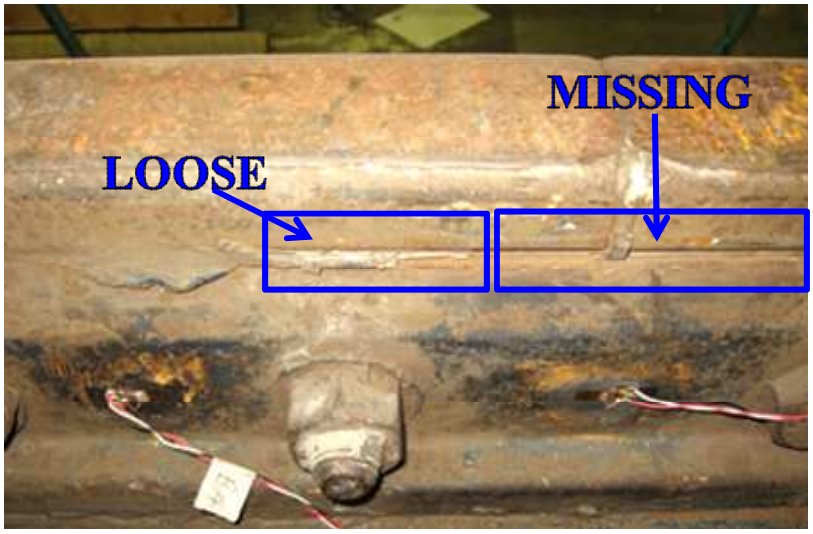

(b)

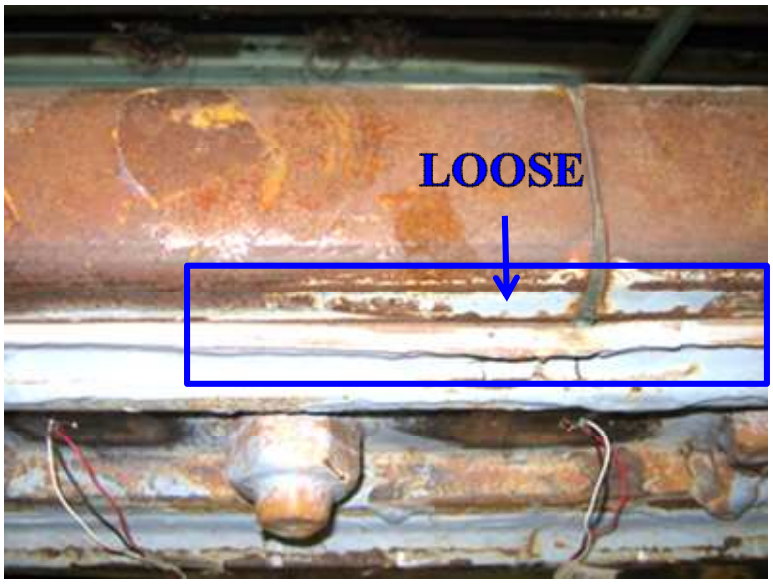

(c)

Figure 2.2: Classifications of damage to the top edge of the insulator layer. (a) Loose and Missing. (b) Loose and Missing. (c) Loose only.

1.) **Missing** means that no epoxy or insulator was visible at the top edge of the joint bar. This does not necessarily imply that the insulation between the rail and joint bar had worn away, only that the outside edge – the part that fills the space between the fillets on the top outer edge of the joint bar and the bottom outer edge of the rail head – had broken off.

2.) **Loose** means that the outside edge of the insulator or epoxy was present but no longer sealed to the metal surfaces. In other words, this section of the edge of the insulator layer was pulling away from the joint.

Generally damage of both types extended outward from the endpost, with the region of missing insulator (if any) occurring closest to the endpost and the region of loose insulator occurring adjacent to the missing section. This suggests that the outer edge of the insulator and excess epoxy tends to loosen before eventually cracking off.

In consideration of this, two damage metrics were adopted:

1.) The distance from the endpost to the end of the missing epoxy, denoted V_m for "missing".
2.) The distance from the endpost to the end of the missing or loose epoxy, denoted V_d for "damaged". V_d is equal to V_m plus the length of loose epoxy.

Destructive disassembly of the test specimens

The six test specimens were disassembled by removing the bolts with a cutting torch and separating the joint bars. Removing the joint bars from a bonded IJ is difficult, especially for joints with little or no deterioration. Sufficiently degraded joints were separated by driving a thin masonry chisel along the web of the rail between the rail and the bar. Less degraded joints were loaded in 3-point, lateral (out-of-plane) bending to around 400 kN, until the tension-side bar separated. For the strongest joints, the same procedure was used, except that the compression-side bar was first sawed in half at the rail gap. In the latter case, only one of the two joint bars was removed.

The interior surfaces of the joint were then examined. Areas of progressive epoxy debonding can be identified visually in a disassembled joint (Davis et al. 2005). These regions have a reddish or brown color due to oxidation on the unsealed metal surfaces. Areas where the metal is visible, but shiny and unoxidized, show where the epoxy pulled away from the metal only during disassembly. Such a surface appearing on the rail will usually be matched at a corresponding location on the joint bar by clean epoxy or insulating fibers, and vice versa. Finally, areas with clean, exposed fibers on both sides

indicate that the insulator fabric itself fractured, implying that it is still bonded to both the rail and joint bar. Thus, a dark or reddish color indicates an area that debonded before disassembly, while a light, epoxy-colored, or shiny surface indicates a part of the layer that stayed bonded until disassembly.

For each test specimen, the distance from the endpost to the first intact epoxy was measured along nine horizontal lines – three on the underside of the rail head, three on the web, and three on the top side of the base (Figure 2.3a). These measurements were repeated for each of the four rail / joint-bar interfaces, on both the rail and the corresponding joint bar. (For two joints, TB1 and TB2, only one joint bar was successfully removed; therefore, only two rail / joint-bar interfaces were available for measurement.) When the measured distance on the rail differed from the measured distance on the joint bar, the maximum value was used. These one-dimensional measurements were then used to estimate the shape and area of the debonded regions.

There is a degree of subjectivity in some cases. Three patterns in particular introduced some uncertainty:

1.) Areas where small dark red or brown patches were speckled with other light-colored patches.
2.) Areas with dark brown or black, but not reddish, discoloration. All of the metal surfaces should have been cleaned and grit-blasted before the epoxy was applied, and should have remained clean and shiny while sealed beneath the epoxy. A dark color could simply mean that some carbon or dirt was present when the joint was assembled. It could also result from some chemical process in the curing epoxy, which might or might not affect bond strength. Given that such areas tend to

occur in proximity to heavily rusted areas, they might also show where the surface has debonded and been exposed to air and moisture, but not long enough for visible rust to form.

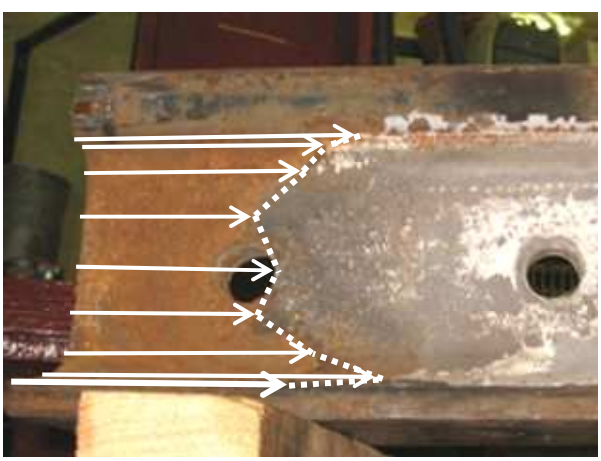

(a)

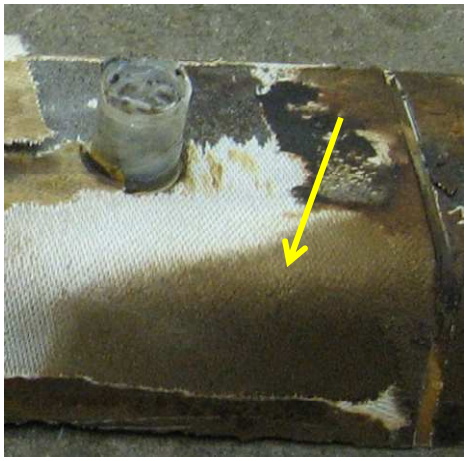

(b)

(c)

Figure 2.3: Disassembled IJ's. (a) Measuring the debonded region. (b) Dirt between layers of the insulator fabric. (c) Inclusive versus Strict debonding.

3.) In one case, the insulating fabric split, revealing dirt between the two layers (Figure 2.3b). A split between layers of the insulator normally implies that the epoxy remains secured to the metal surfaces, and is therefore not debonded. The presence of dirt, however, strongly suggests that the split occurred and grew while the joint was in service, rather than during the disassembly procedure.

The third condition probably suggests a loss of integrity of the layer that would have an effect on IJ performance similar to that of debonding between epoxy and metal; therefore, this area was included in measurements of the "debonded region". It is more difficult to say what effect the other two conditions would have on joint performance. Because it is unknown whether these ambiguous regions truly represent a loss of epoxy bond, two sets of measurements are used throughout this thesis. One set, called the "Inclusive" measurement of debonding, included all areas with dark discoloration or heavy speckling. The other set of measurements, referred to as "Strict" debonding, included only those areas where reddish brown rust or dirt covered all or most of the surface. An example of the difference between the two measurement sets is shown in Figure 2.3c. The area of the debonded region measured using the Inclusive criteria is referred to as A_i, while the area measured using the Strict criteria is A_s.

It is also worth noting that the surfaces exposed by disassembly differ in appearance between the two IJ manufacturers, due to the materials and assembly processes used by each. Debonding was easier to identify on test specimens from Supplier B, where the areas of intact epoxy bond tended to be silver or white in color, than on those from Supplier A, where bonded areas often had a yellow or brown hue.

In most cases, some debonding also occurred near the outer ends of the joint bars, spreading inwards towards the endpost. These areas were also measured, but turned out to be small in relation to the corresponding debonded region near the endpost. These areas were not included in the reported results or considered in the analysis.

2.3 Size and shape of debonded regions

Total area and distribution

The total area of the debonded region (A_i or A_s) was measured for each test specimen (Table 2.1). This is the simplest single statistic for representing the extent of epoxy debonding in a rail joint. Note that the total debonded area for a joint is the sum of the debonded areas on each of the four bonded rail / joint-bar interfaces.

Table 2.1: Debonded areas.

SPECIMEN	A_i (mm^2 × 1,000)	A_s (mm^2 × 1,000)
TA1	99	58
TA2	134	79
TA3	180	160
TB1*	34	21
TB2*	20	8
TB3	140	111

* Estimated from measurement of one side only

A_i versus A_s

Because A_i is defined to include some areas not included in A_s, the ratio A_s:A_i will always be less than or equal to 1 for all rail / joint-bar interfaces. For the test specimens studied,

the average ratio A_s:A_i was 0.67. The maximum value of this ratio was 0.95, the minimum was 0.36, the median was 0.69, and the standard deviation was 0.17. The difference between these two measurements of debonding is large enough that they must be analyzed individually.

Distribution of the Debonded Area Within a Joint

There are four interfaces formed between the two rails and the two joint bars, and the extent of debonding may vary between interfaces. IJ behavior might be sensitive not only to the total amount of debonding over all four interfaces, but also to the distribution of debonding over these interfaces. For instance, the longitudinal strength of the joint is likely to be determined by the two interfaces with the weakest remaining bond strengths, because slippage can occur when the bond fails at only two interfaces.

Some nomenclature must be defined in order to state the questions of interest. I use the term "side" to denote the interfaces associated with one joint bar, so that the interfaces between the field-side joint bar and both rails are on one "side", while the interfaces between the gauge-side joint bar and both rails are on the opposite side. The term "end" denotes the interfaces associated with one particular piece of rail. To an observer looking at one side of the joint, one "end" will be on the left, and the other on the right.

The two questions of interest are whether the debonded area is equal on both sides, and whether it is equal on both ends. The ratio of the debonded area on one side (or end) to that of the other side (or end) is shown in Table 2.2. The numerator is always the

larger of the two values; a ratio of 1 implies that both sides have the same amount of debonding, while a ratio of 2 implies that one side has twice as much debonding as the other.

Table 2.2: End vs. end and side vs. side distribution ratios of the debonded area. The larger debonded area always goes in the numerator.

	A_i		A_s	
SPECIMEN	End : End	Side : Side	End : End	Side : Side
TA1	1.14	1.21	1.57	1.13
TA2	1.57	1.10	1.97	1.02
TA3	1.60	1.07	1.58	1.01
TB1	1.61		2.21	
TB2	1.15		1.12	
TB3	1.42	1.02	1.70	1.01
AVERAGE	1.41	1.10	1.69	1.04

Practitioners have noted that one end of an IJ often appears more deteriorated than the other, especially on tracks with directional traffic or heavier tonnage in one direction. It is also possible that more debonding might occur on one side than the other, given the presence of lateral loads in the track. On the other hand, even if there is no systematic difference in debonding between the two sides, some random variation will occur. Therefore, it is necessary to analyze the data carefully in order to determine whether differences in the amount of debonding are systematic or the result of random variation.

Difficulty arises in trying to pool the data from different specimens. One concern is that the total amount of debonding varies widely between specimens, which could overwhelm the differences between interfaces within a joint. Therefore, the analysis was

performed not on the actual debonded area of each interface, but on the proportion of the joint's total debonded area that lies on each interface.

Another problem is that the specimens lack a natural orientation. For each joint, random variation makes it likely that there will be more debonding on one side than on the other. If the field side has more debonding in all the joints, then it could be said that the field side generally has more debonding than the gauge side. On the other hand, if some specimens have more debonding on the field side and others have more on the gauge side, then the variation is likely to be due to random chance alone. But for the test specimens studied in this analysis, the field and gauge sides are unknown. This makes it difficult to distinguish between systematic differences and random variation.

One way to avoid this problem is to use the multi-factor Analysis of Variance technique, abbreviated ANOVA. Using the ANOVA test on a single specimen gives the amounts of variation between interfaces that can be attributed to side, end, and random error. (Technically, the third term is not "random error" but rather the "interaction" of side and end – the variation between debonding on "opposite corners" of the IJ. For the butt-end joints studied here, it was assumed that the physical interaction effects would be negligible, so that any measured interaction should instead be attributed to random error.) "Variation" is represented by a positive-definite sum-of-squares term that depends only on the magnitude of the differences between each interface.

Each of the two variation measurements (side and end) for a single specimen has only one degree of freedom, making the typical F-test too weak to be useful. But because the variation is always positive, the ANOVA results from the individual samples can be

pooled together without concern for orientation – the results from one specimen never cancel out the results from another. The results from each specimen were summed to produce the total sample variations due to side, end, and random error. Because there were four specimens (TA1, TA2, TA3, and TB3) with complete debonding data available, each of the pooled sums had four degrees of freedom. F-statistics and p-values were computed from these pooled sums (Table 2.3).

Table 2.3: Two-factor ANOVA results.

	A_i				A_s			
	SSQ	DOF	$F_{4,4}$	p	SSQ	DOF	$F_{4,4}$	p
Side	0.003	4	0.28	0.12	0.001	4	0.66	0.37
End	0.034	4	2.98	0.84	0.068	4	45.59	0.99
Error	0.011	4			0.001	4		

The results showed much more variation in debonding between ends of the joint than between sides. In fact, the low p-values strongly suggest the variation in debonding between the field and gauge sides was due to random error rather than a systemic difference.

Removing the "side" factor from the analysis improves the power of the test for the remaining "end" factor, because it allows the random error to be estimated with greater certainty. A one-factor analysis (Table 2.4) showed that the tendency for one end of the joint to have more debonding than the other was statistically significant. It is unknown whether these test specimens had been exposed to directional traffic, but the

results are consistent with practitioners' observations that one end tends to degrade faster than the other.

Table 2.4: One-factor ANOVA results.

	A_i				A_s			
	SSQ	DOF	$F_{4,4}$	p	SSQ	DOF	$F_{4,4}$	p
End	0.034	4	4.65	0.97	0.068	4	54.77	0.99
Error	0.015	8			0.002	8		

Shape of the debonded region

In addition to the distribution of debonding over the different rail / joint-bar interfaces, some consideration must be given to the shape of the debonded region. As noted above, debonding tends to begin near the endpost and grow outward towards the edges of the joint bar; however, the interface between bonded and debonded is not necessarily a straight vertical line. It more commonly has a "V" or "U" shape (Figure 2.4a), with debonding extending farther along the top and bottom of the interface than along the bolt line.

The shape can be described using the following measurements:

- *H* is the average distance from the endpost to the first intact epoxy along the upper part of the interface, where the joint bar meets the underside of the rail head;
- *W* is the average distance from the endpost to the first intact epoxy along the part of the interface adjacent to the rail web; and

- *B* is the average distance from the endpost to the first intact epoxy along the bottom of the interface, where the joint bar meets the top of the rail base.

The characteristic shape in Figure 2.4a corresponds to values of *H* and *B* that are larger than *W*. It appears that debonding tends to begin along the upper and lower edges of the interface (Figure 2.4b) – that is, *H* and *B* grow to a certain value while *W* remains small. After a certain amount of degradation all three measurements start to grow equally, so that $H - W$ and $B - W$ stop increasing.

Table 2.5 shows summary statistics of the relevant measurements of $H - W$ and $B - W$ for each rail / joint-bar interface of each test specimen. Average and median values were generally close to 30 mm and approximately one standard deviation above zero. (The sole exception was the $H - W$ measurement for Inclusive debonding, which had similar average and median values but larger variance.) It is difficult to draw strong statistical conclusions from these numbers, because the four interfaces of each joint may not be independent, but it does appear that debonding tends to be more extensive near the top and bottom of the insulator layer than at the center.

Table 2.5: Difference between extent of debonding on different parts of the rail / joint-bar interface as measured from the endpost (mm).

	Inclusive		Strict	
	$H - W$	$B - W$	$H - W$	$B - W$
Average	35	27	24	35
Median	26	28	20	31
Maximum	179	78	75	85
Minimum	-89	-22	-3	-6
Std. Dev.	62	27	21	27

(a)

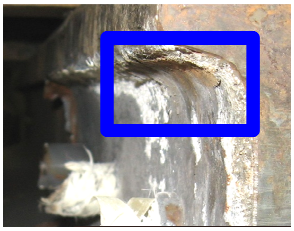

(b)

Figure 2.4: Shape of debonded region. (a) Debonding (dark area) extends top and bottom of interface. (b) Onset of debonding at endpost.

This conclusion is consistent with several known features of the debon process. Finite element modeling has suggested that, in a fully bonded IJ subje wheel loads, the shear and peel stresses that presumably promote debonding ar near the top and bottom edges of the epoxy (Himebaugh et al. 2007). The sam could be expected to continue as the epoxy bond recedes from the endpost. Th

bottom regions are also more exposed to moisture, which has been experimentally demonstrated to hasten the debonding process (Nicoli et al. 2007).

2.4 Effectiveness of visual inspection

The visual inspection conducted in this study examined the top edge of the insulator layer where it is visible between the rail and joint bar. The debonding patterns observed in the disassembled IJ's suggested that inspecting only this part of the bond might be somewhat misleading. In some cases, disassembling the joint showed that the outer edge of the insulator layer had debonded from the filleted edges on the rail or joint bar, but that this debonding did not extend past the fillets (Figure 2.5). More generally, the tendency for debonding to extend farther along the top of the interface than along the center is a potential problem for a measurement based only on the top edge. However, comparing the results of the pre-disassembly inspection with the post-disassembly debonding measurements showed that the visual metric V_d can in fact be used to estimate the area of the debonded region with reasonable accuracy.

Estimates of debonding along a single rail / joint-bar interface

The visual inspection metrics V_m and V_d for each rail / joint-bar interface are presented in Tables 2.6 and 2.7, with the sides arbitrarily labeled A and B and the ends labeled L and R.

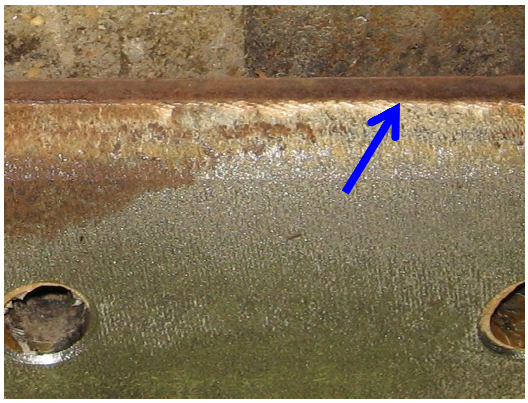

Figure 2.5: Debonding behind visible edge of insulator without corresponding debonding on hidden surface.

Table 2.6: Visual inspection results – V_m (mm from endpost)

	Joint bar A		Joint bar B	
Specimen	Left	Right	Left	Right
CA1	0	0	0	0
TA1	0	30	0	0
TA2	170	100	180	80
TA3	210	220	150	290
CB1	0	0	0	0
TB1	0	0	0	0
TB2	0	0	0	0
TB3	150	80	140	50

Table 2.7: Visual inspection results – V_d (mm from endpost)

	Joint bar A		Joint bar B	
Specimen	Left	Right	Left	Right
CA1	0	0	0	0
TA1	60	90	50	110
TA2	170	100	180	80
TA3	210	220	230	300
CB1	0	0	0	0
TB1	90	30	80	30
TB2	30	80	0	0
TB3	250	150	200	100

Plotting these measurements versus the debonded area of each interface revealed a strong correlation (Figure 2.6). The relationship between V_d and debonding appears linear over the whole range of measurements, so a straight line, constrained to pass through the origin, was fit to the data. Analysis of V_m was complicated by the fact that, for many interfaces with measurable debonding, $V_m = 0$. It does appear that V_m has a linear relationship with debonding when it is non-zero, but the correlation is not as strong as for V_d. Therefore, V_d is a more useful indicator of debonded area than V_m.

V_d correlates more strongly with A_s than with A_i. Thus, estimates of A_s based on V_d will be more accurate than estimates of A_i.

Estimates of debonding over an entire IJ

The purpose of visual inspection is to estimate debonding using the visual metrics, and so a goal of the analysis was to develop confidence intervals for that estimate. Unfortunately, it is difficult to create confidence intervals from the above data because they may not be independent: it is physically plausible that damage to the edge of the insulator layer on one end or side of the joint might be affected by debonding on the other end or side. Attempts to test for independence yielded ambiguous results.

As an alternative, it is possible to estimate the debonded area of a whole joint, by pooling data from all four interfaces. This results in data points that can be assumed to be independent and therefore allows the calculation of confidence intervals. The total debonded area for each joint was plotted versus the sum of V_d over the four rail / joint-bar interfaces of that joint and a line was fit to these totals (Figure 2.7). (A similar analysis

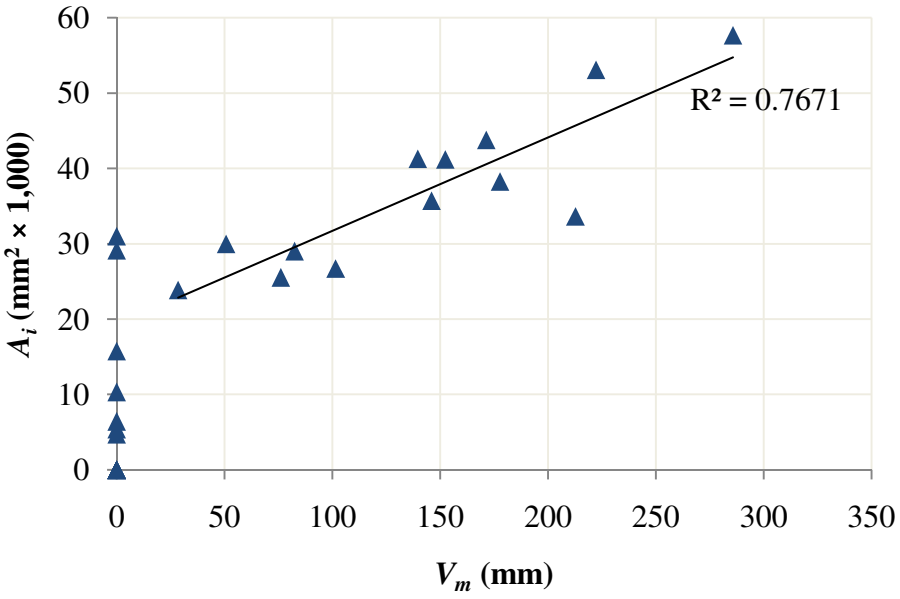
60
50
40
30
20
10
0
0
50
100
150
200
250
300
350
R² = 0.7671
A_i (mm² × 1,000)
V_m (mm)

(a)

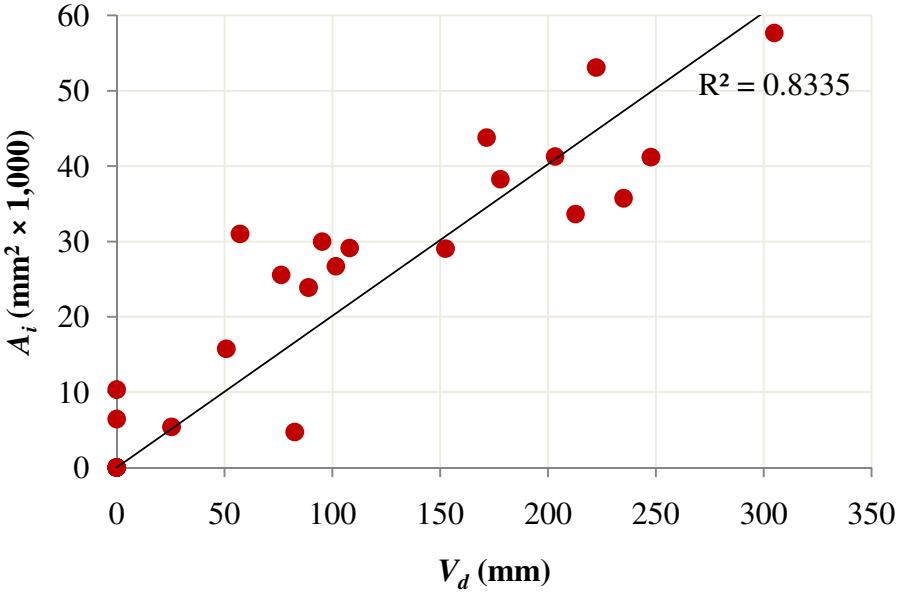
60
50
40
30
20
10
0
0
50
100
150
200
250
300
350
R² = 0.8335
A_i (mm² × 1,000)
V_d (mm)

(b)

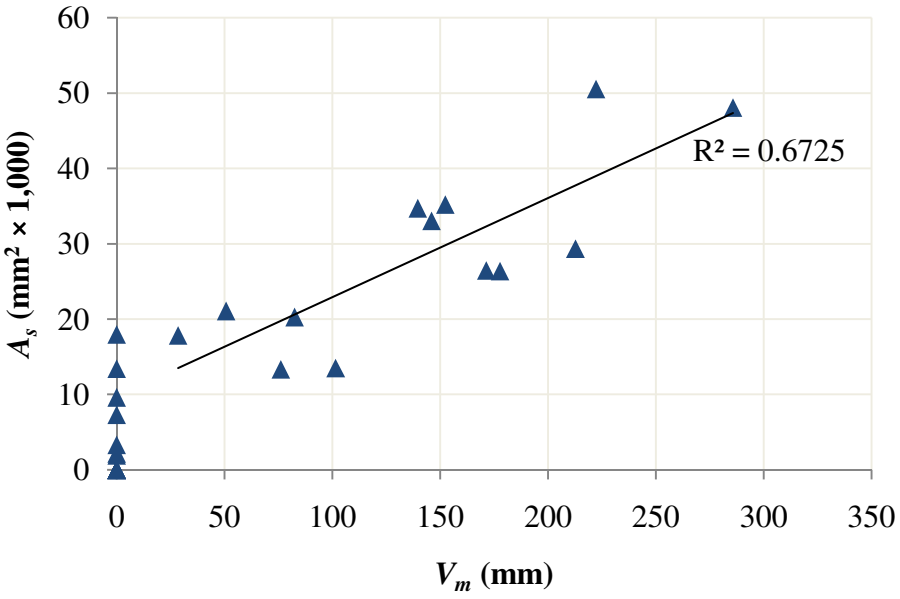

(c)

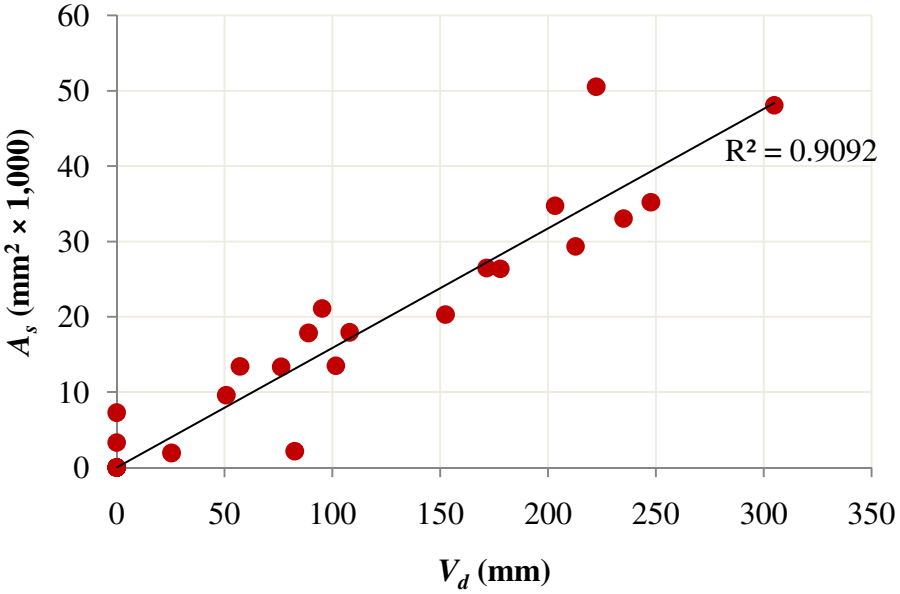

(d)

Figure 2.6: Actual debonding versus visual inspection metrics for each rail / joint-bar interface. (a) A_i versus V_m. (b) A_i versus V_d. (c) A_s versus V_m. (d) A_s versus V_d.

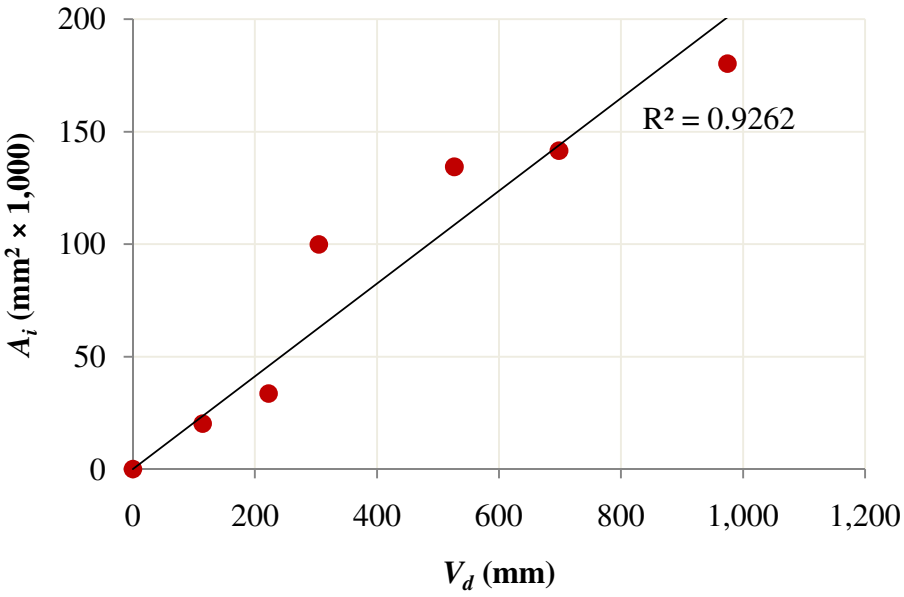

(a)

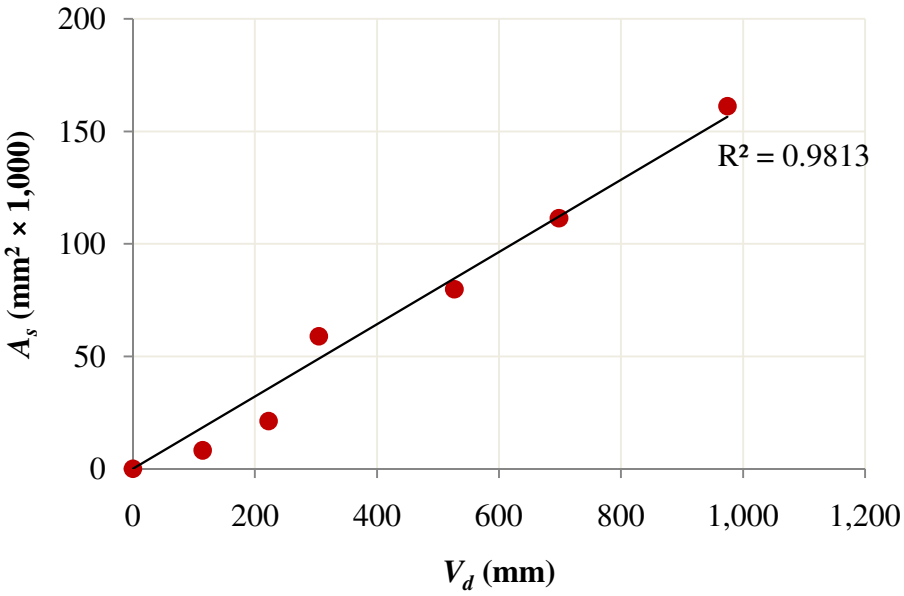

(b)

Figure 2.7: Actual debonded area versus V_d for whole joints. (a) A_i. (b) A_s.

using V_m had too few non-zero data points to derive meaningful results.) The debonded area of a particular joint can be estimated by multiplying the sum of V_d on all four interfaces by the slope of this line. Analyzed in this manner, it is reasonable to assume that the residual of each estimate is independent of the others. This allows computation of an 80% confidence interval using Student's t statistic with the standard deviation of the residuals (Table 2.8).

Table 2.8: Equations for estimating A_i and A_s from V_d.

Debonding criteria	80% confidence interval
Inclusive	$A_i = V_d \times 206$ mm $\pm$ 27,000 mm^2
Strict	$A_s = V_d \times 161$ mm $\pm$ 11,000 mm^2

Visual damage versus average extent of debonding

Railroaders sometimes state (based on visual inspection) that a joint is "debonded out to" a certain distance, implying that the length of the missing or damaged edge is equivalent to the extent of the debonding underneath. To some extent, this represents a simplification, because the actual debonded region extends outward by different amounts on the top, middle, and bottom parts of the rail / joint-bar interface. A_i and A_s are area measurements (mm^2) while V_d is a linear measurement (mm).

It is, however, possible to define an "average debonded distance" by considering a rectangle with the same area as the actual debonding region (Figure 2.8). The height of this rectangle is equal to the parametric length from the top of the rail / joint-bar interface

to the bottom. I will call the rectangle's length the Inclusive or Strict "debonded distance", denoted D_i or D_s.

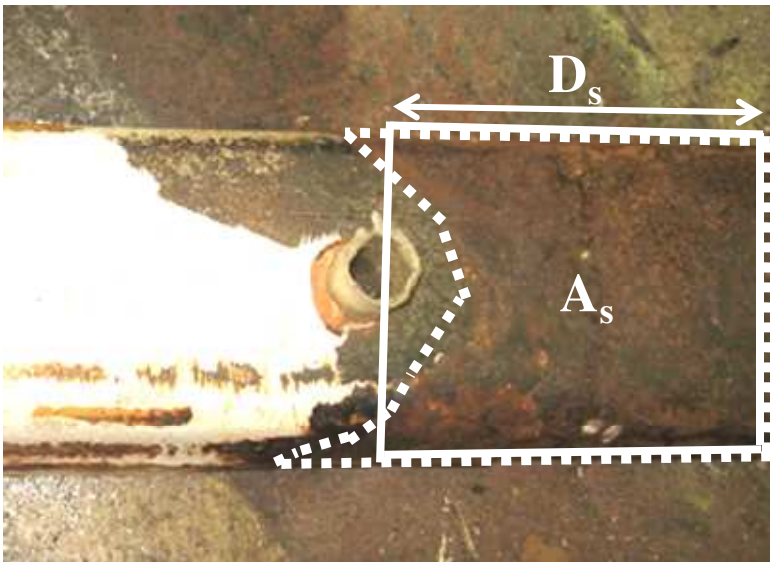

Figure 2.8: Defining the Strict debonded distance. The dotted line defines the actual Strict debonded region, with area A_s. The rectangle has area A_s and length D_s.

The height of the rectangle is approximately equal to 175 mm for each test specimen, so $D_i = A_i$ / 175 mm and $D_s = A_s$ / 175 mm. Substituting this value into the equations of Table 2.8 gives the relationship between V_d and D_i or D_s (Table 2.9), including confidence intervals. V_d was, in fact, quite close to the "average debonded distance" under this definition: on average, it was about 18% less than D_i and 8% more than D_s.

Table 2.9: Equations for estimating D_i and D_s from V_d.

Debonding criteria	80% confidence interval
Inclusive	$D_i = V_d \times 1.18 \pm 157$ mm
Strict	$D_s = V_d \times 0.92 \pm 65$ mm

2.5 Conclusions

Subjectivity of measurements of the debonded region

Although it is possible to learn a great deal about the state of progressive epoxy debonding in an IJ by disassembling it and examining the rail / joint-bar interfaces visually, some judgment and interpretation is needed to determine the exact shape of the debonded region. Because the meaning of some visual phenomena was unclear, two different criteria for determining the debonded region (Inclusive and Strict) were used to calculate the debonded area (denoted A_i or A_s). Of the two, the Strict criteria yielded more consistent statistical measurements of the shape of the debonded region and correlated better with the visual inspection metric V_d, although this does not necessarily imply that the Strict area is more important to the performance or likelihood of failure of a given joint.

Shape and distribution of debonded region

Epoxy debonding tends to begin at the endpost near the top and / or bottom edge of the joint bar. At some point debonding also begins to affect the part of the insulator layer adjacent to the rail web, but it generally remains more extensive on the upper and lower portions. On average, debonding extends about 30 mm farther along these parts of the

interface that match the head and base of the rail than along the web, but there was considerable variation between specimens. The variability was greater when using the Inclusive measurement of debonding than when using the Strict measurement.

Debonding occurs on all four rail / joint-bar interfaces within a joint. The size of the debonded region does not vary significantly between the field side and the gauge side. However, there is a significant tendency for one end of the joint to have more debonding than the other end.

Visual inspection

Two visual inspection metrics were defined for each rail / joint-bar interface based on the appearance of the upper edge of the insulator layer, where it is visible between the rail head and the top of the joint bar. V_m is the distance from the endpost to the first visible epoxy or insulator, even if it has pulled loose from the surface. V_d is the distance from the endpost to part of the insulator layer edge that is intact, in its original position, and not separated from either metal surface.

V_d turned out to be more useful than V_m, largely because V_m tends to remain zero until the debonded area becomes sufficiently large. V_d begins to increase with very little debonding.

V_d correlated well with A_s and, to a lesser extent, A_i. One millimeter of missing or loose top edge corresponded to 206 mm^2 of A_i and 161 mm^2 of A_s. These relations allow the debonded areas A_i and A_s for the entire joint to be estimated to within ± 27,000 mm^2

and ± 11,000 mm^2 respectively. It also appears that the V_d measurement of a single rail / joint-bar interface will provide a good estimate of the debonded area of that particular interface.

CHAPTER 3: DEFORMATION UNDER LONGITUDINAL LOAD AS A BASIS FOR AUTOMATED ESTIMATES OF EPOXY DEBONDING

3.1 Introduction

Every component of railroad track other than the subgrade has a finite service life, and the replacement of worn-out components is a continual part of the railroad maintenance process. A replacement plan must balance at least three conflicting priorities: minimizing the frequency of replacement, avoiding disruptive failures, and allowing enough lead time for the work to be scheduled efficiently. Replacing track components costs the railroad both directly, for materials and labor, and indirectly, in the form of track occupancy, so it is important to avoid premature replacement. On the other hand, to keep the railroad in good working order and to avoid safety problems or service disruptions, components must be replaced before they fail. Finally, maintenance work that can be scheduled in advance tends to cost less both directly and indirectly than work conducted on short notice.

Better knowledge about the remaining service life and probability of failure allows maintenance planners to balance these three competing priorities more effectively. Railroads conduct extensive inspections of their physical assets, including track, structures, and rolling stock, in order to detect failing components before they cause disruptions. Because of the uncertainty involved in estimating remaining serviceability, more frequent inspections allow for longer service life with less disruptive failure. Similar benefits can be gained by collecting information or applying algorithms that improve predictions of remaining life.

As noted in Chapter 2, current inspection practices for bonded insulated joints include looking for signs of bond failure, such as wide rail gaps or broken bolts. Joints with these symptoms may be at risk of developing disruptive (but fail-safe) signal problems as well as serious safety problems. Visual inspection can also be used to measure the extent of progressive epoxy debonding, using careful measurements of damage to the top edge of the epoxy / insulator layer. Because epoxy debonding progresses over time, these measurements may enable the railroad to track IJ deterioration and estimate remaining life or probability of failure. This would allow maintenance planners to schedule IJ replacement in a more timely and efficient manner. At least one North American Class 1 railroad has codified the use of visual estimates of debonding in its maintenance standards.

On the other hand, visual inspection has drawbacks. The most critical is that a detailed inspection of an IJ is a time-consuming task, in part because these joints are dispersed over the entire signalized portion of the rail network. The economic benefit of such labor-intensive inspections diminishes rapidly with increasing inspection frequency. The necessity to examine the epoxy edge close up, looking for the subtle separation between epoxy and steel, may also affect a lone worker's ability to conduct the inspection safely without obtaining track authority. In the United States, a lone worker can only foul the track without positive authority from the dispatcher if he avoids "occupy[ing] a position or engag[ing] in any activity that would interfere with the worker's ability to maintain a vigilant lookout for, and detect the approach of, a train" (CFR 2007b).

It is also unclear how consistently and accurately the visual inspection metrics could be collected in the field. The results in Chapter 2 show that the length of loose or

missing epoxy along the top edge of the joint bar correlates well with the size of the debonded area. However, those results were obtained using a single inspector in an indoor, unchanging environment. Several variables, such as the individual doing the inspection and the lighting conditions, might add variability to field results and reduce the accuracy of the debonding estimates.

A research project was undertaken to investigate the feasibility avoiding some of these difficulties with a fully automated method of detecting and measuring progressive epoxy debonding in bonded insulated joints. The goal was to develop a system of inexpensive, unattended, maintenance-free engineering sensors whose data could be used to provide continual estimates of the size of the debonded region as it initiates and grows.

In this chapter I present an overview of the system's design and describe the numerical modeling that provides the theoretical basis for inferring the debonded area from the sensor measurements. Chapter 4 then describes laboratory tests that were conducted to test the model's accuracy. The sensor system itself remains under development, and is expected to begin limited field testing in the near future.

3.2 Deformation sensors

Although vision-based metrics are useful, they may not be practical for a fully-automated epoxy debonding measurement system. The technology to inspect the top edge of the epoxy / insulator layer using computer vision systems is probably achievable: it does not appear to be intrinsically harder than the problem of detecting cracks in non-bonded joint bars, for which a system is already available (Berry et al. 2007). The economic feasibility

of such a system is less clear. To obtain the high frequency of inspection that would enable good prediction of failure, a vehicle-mounted computer vision system would consume an excessive amount of track time.

If there were a widely deployed computer vision system capable of performing many other inspection tasks simultaneously, and if a debonding estimation feature could be added at low marginal cost, then the overall system might be able to justify the costs of frequent inspections. Automated, vision-based systems are being considered for a number of other track inspection tasks (Sawadisavi 2008), but it is not clear how these systems will be integrated or whether additional features could be added for low cost. Furthermore, many of these tasks, such as measurement of rail profile or ballast shoulder width, might not benefit significantly from high-frequency repetition, and thus would not help to justify the cost of short inspection intervals.

An alternative approach in the case of discrete components such as insulated joints is to use simple, inexpensive, low-maintenance equipment that can be installed at the component location and left in place. This approach enables continuous, automated data collection without disrupting railroad operations.

The low-cost, low-maintenance requirement limits the types of sensors that can be included in a leave-in-place system, but two common engineering sensors qualify: the strain gauge, and the strain-gauge-based extensometer. Both of these measure localized deformation in a specified dimension at a specified location. These devices require little or no maintenance after installation, can be adapted for use in difficult environments, and have potential service lives exceeding those of most insulated joints used in heavy axle

load service. Strain gauges have already been used to measure IJ deformation for certain research applications (Li et al. 2006).

Conventional strain gauges have some disadvantages that make them infeasible for large-scale applications such as monitoring progressive epoxy debonding in the field. While the gauges themselves are inexpensive and can be sealed against harsh environments, signal conditioning and data logging equipment appropriate for long-term use in an outdoor environment is costly. Strain gauges also require skill and effort to install in the field. Finally, a great deal of wiring would be required to connect the sensors, located on the IJ itself, to the data logger and power supplies, which would be located outside the track structure. This wiring is vulnerable to damage, especially if the sensors are to be left in place during tie or ballast renewal operations.

To address these general problems with strain gauges, research is underway to develop wireless, semi-autonomous, self-networking strain gauges, built from inexpensive commodity parts and designed for quick and easy field installation (Socie and Barkan 2008). These sensors include a set of foil strain gauges (arranged to compensate for various sources of noise, such as thermal strains), a low-power microprocessor, a low-power radio, and a battery, all in a sealed, weatherproof package of a few square centimeters (Figure 3.1). Each sensor can measure, store, and process digital deformation data, spontaneously join wireless networks using the Zigbee® radio protocol, and exchange messages and data with other devices on the network.

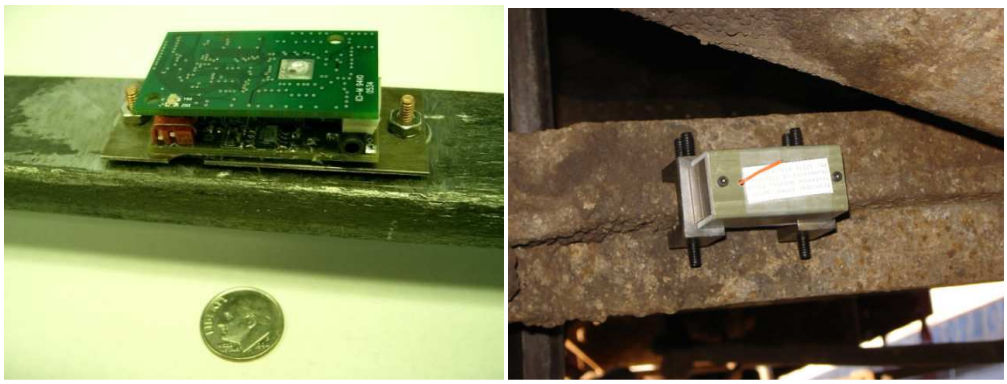

(a) (b)

Figure 3.1: Wireless strain gauges. (a) Attached to steel bar, protective casing removed. (b) Attached to railroad car brake beam.

The radios and network protocol used by these sensors are designed for low-energy devices. Radio range is short (less than 100 m), and the protocol allows them to spend most of their time in a low-energy sleep state. The energy required for the sensors used in an epoxy debonding monitoring system could probably be obtained by harvesting it from environmental sources such as vibrations or the track circuit itself.

The wireless strain gauges, unlike a traditional foil gauge, have a pair of discrete mounting points at the ends, 55 mm apart. These points can be attached to the surface using any desired method that will hold them tightly and securely in place. Extensive surface preparation is not necessary. The output of the sensor is the relative displacement of these two points divided by the (fixed) distance between the points. If the two mounting points are attached to the same surface, the sensor acts as a strain gauge. If the mounting points are attached to two different surfaces – such as the two different rails in a rail joint – the device can function as an extensometer. Extension is computed by multiplying the strain times the fixed gauge length.

3.3 Inferring debonding from deformation

When a portion of the epoxy in a glued insulated joint debonds from the rail or joint bar, it loses some or all of its ability to transfer shear stresses between the steel components. By affecting the stress distribution, debonding also alters the deformation of the system under a given load. Therefore, information about the deformation of the joint under a known load may allow inferences about the size of the debonded region. Given new deformation-measuring sensors (strain gauges and extensometers) that are practical to use in such an environment, the important question is: what measurements give information about the state of epoxy debonding, and what do particular values of those measurements indicate?

IJ's generally experience two kinds of loads in service: wheel loads from passing trains, and thermal loads – mostly longitudinal – from the restrained expansion and contraction of the rails. The deformation of the joint under wheel loads depends on variables that are external to the joint itself, such as car weight and suspension, track modulus, and train speed. Thus it would be difficult to infer debonding based on the deformation under these loads. On the other hand, the deformation of an IJ in response to a thermal load depends mostly on the magnitude of the load and the configuration of the joint itself, including the internal stress transfer mechanisms such as the epoxy bond. Therefore, deformation of the joint under longitudinal loads appears more useful for inferring information about epoxy debonding.

Deformation sensors would preferably be placed at locations that have three properties:

1.) The deformation at the location under a longitudinal load varies with the extent of epoxy debonding.
2.) For better calibration, the deformation should *not* be sensitive to any other loads acting on the joint.
3.) To allow some tolerance in sensor installation, they should be located away from sharp strain gradients.

The locations considered in this analysis are shown in Figure 3.2. The two "sides" of the joint (as defined in Chapter 2) are arbitrarily labeled A and B, with the ends labeled L and R (for "left" and "right") based on what an observer would see while standing on side A. Strain gauge locations are on the outside surface of each joint bar halfway between each pair of bolts. (In order to match the laboratory conditions in Chapter 4, this anaylsis uses 6.35 mm strain gauges; the 55 mm sensors shown in Figure 3.1 would yield slightly different numbers.) The strain on the outside surface of the A joint bar adjacent to the rail gap is designated A1. Working outward towards the ends of the joint bar, the next locations are designated A2L and A2R, and the outermost are A3L and A3R. Matching locations named B1, B2L, B2R, B3L, and B3R are directly opposite on the other joint bar.

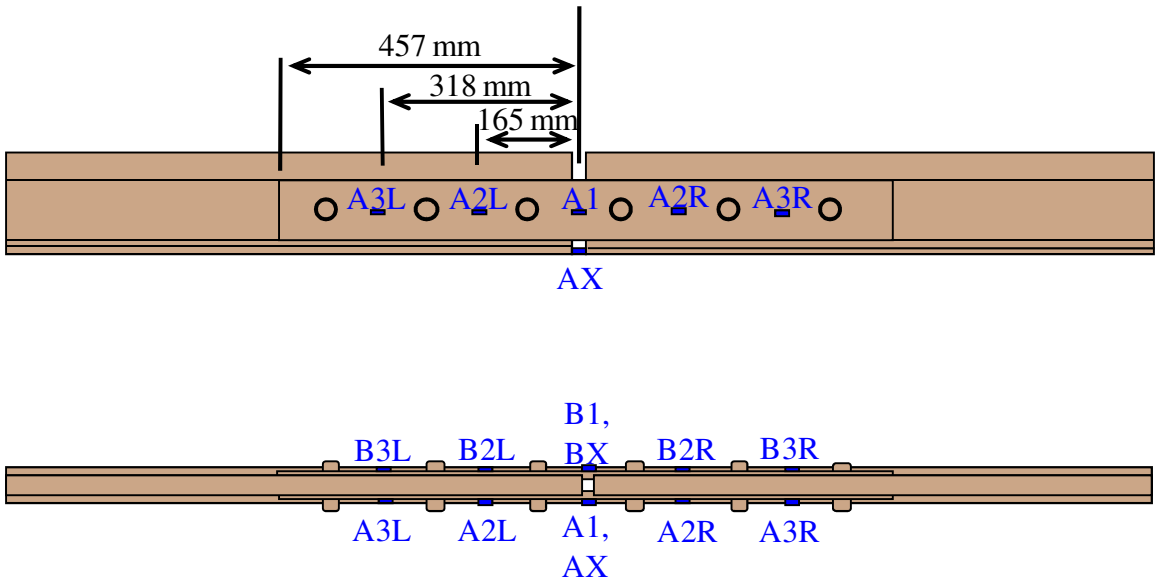

Figure 3.2: Locations for strain and extension measurements.

Because these locations are near the neutral axis of the joint, vertical bending loads in the rails will not significantly affect strain values. By averaging the strain at each A-side location with its corresponding B-side partner, the effects of any lateral bending forces will also be minimized. The locations are as far as possible from the stress-concentrating bolt holes so that strain gradients will be relatively mild. Therefore, the locations on the joint bar surface satisfy properties (2) and (3). Concerning property (1), it is shown below that the strain at some (but not all) of these locations is affected by the extent of epoxy debonding.

The amount by which the ends of the rails elastically separate under load is measureable by extensometers placed across the gap at the base of the rail, one on each side of the joint. These extension measurements are termed AX and BX. Lateral bending loads can again be factored out by averaging the two measurements together. Unfortunately, these locations are located far from the neutral axis and will be sensitive

to vertical bending loads. Whether this presents a difficulty will depend on the magnitude and variability of vertical bending loads that develop in the rail under thermal loads. Theoretically a second pair of extensometers at the rail head could be used to factor out vertical bending loads, but in practice extensometers at such a position would be exposed to damage from trains and maintenance activities.

Because the measured deformations from the two sides of the joint are averaged together to factor out lateral bending strains, it is convenient to define some composite or average measures as well. Composite measurements S1, S2L, S2R, S2, S3L, S3R, and S3 are based on average strains across the two joint bars, and composite X is based on the average of the two extensometer readings (Table 3.1). More precisely, these S and X composites are "strain (or extension) coefficients", as described in section 3.4, rather than absolute strain measurements; but, in each case, they are based on the average measured values at two or more locations.

Table 3.1: Composite deformation measurements.

Composite	Defined from
S1	A1, B1
S2L	A2L, B2L
S2R	A2R, B2R
S2	S2L, S2R
S3L	A3L, B3L
S3R	A3R, B3R
S3	S3L, S3R
X	AX, BX

3.4 Mechanical Analysis

The premise behind the automated debonding measurement system is that the stress state of the joint will be measurably altered by epoxy debonding. Thus some means must be adopted for predicting the state of stress for a bonded IJ under longitudinal loads.

The basic mechanics of conventional bolted rail joints were well understood as early as the 1930's (AREA 1980). More recent work on conventional joints has focused on contact stresses and dynamic effects caused by the discontinuity in the rail running surface and rail stiffness (e.g. Jenkins et al. 1974, Suzuki et al. 2005). Because bolted joints allow some relative motion between the rail ends, less emphasis has been placed on longitudinal loads. Recent work by the Association of American Railroads and the Virginia Polytechnic Institute and State University analyzed different designs for bonded IJ's, including those subjected to longitudinal loads, but did not consider the effects of epoxy debonding on the joint mechanics (Li et al. 2006, Akhtar and Davis 2007, Plaut et al. 2007, Himebaugh et al. 2007).

Finite element model

A numerical approach using the finite element analysis program ABAQUS 6.5 was used to study the effects of debonding on IJ mechanics. The model consisted of two 1,650 mm sections of RE136 rail (AREMA 2000b); two 915 mm joint bars; and a thin layer between the rails and each joint bar representing the combined insulator and epoxy materials. Where appropriate, symmetry planes were used to reduce the size of the model.

The bolts and the endpost, which are usually assumed to have no structural role, were excluded. The bolt holes were included because they affect joint bar strains.

A linear-elastic constitutive model was used for all materials. The steel parts (rails and joint bars) were assigned a Young's modulus E = 207 GPa and a Poisson's ratio of ν = 0.3. The properties for the epoxy material were E = 4.8 GPa and ν = 0.34. This value of E is twice as stiff as that used by Plaut et al. (2007) and Himebaugh et al. (2007), but provided a better match with the experimental results described in Chapter 4. Since the goal of the analysis was not to calculate stresses within the epoxy itself, but rather the measurable deformation on the exterior surfaces of the joint, a precise value for epoxy stiffness was not critical.

For areas of intact epoxy bond, the epoxy layer was tied to both the joint bar and the rail using ABAQUS TIE constraints, which constrain all degrees of freedom on the epoxy surface to those on the metal surface. Debonded areas were represented by removing the relevant epoxy surface nodes from the TIE constraint between the rail and the epoxy and adding CONTACT interactions instead, which transmit compressive forces only. Contact surfaces make a model nonlinear, and require an iterative analysis to find a solution that satisfies the requirements of static equilibrium.

The contact surfaces in the model were frictionless, meaning no shear stress at all developed between the rail and the epoxy in the debonded region. Since some friction is likely to develop at these surfaces, the frictionless model may overestimate the effects of debonding on stress distribution. To model friction would require some way to compute

the residual normal stresses generated as the epoxy cures, which is beyond the scope of this thesis.

The confining action of the bolts was modeled by applying a 220 kN load in a 3 mm thick ring around each bolt hole, similar to previous finite element IJ modeling (Plaut et al. 2007, Himebaugh et al. 2007). The model was not very sensitive to the magnitude of the bolt load, but the presence or absence of confinement did measurably affect the results for certain scenarios. After this load was applied, a second analysis step added a concentrated longitudinal tensile force at the neutral axis of the rail. The output of the model was the additional deformation due to this second step, which is what would be measured by a strain gauge applied to an assembled IJ.

Linearity and load magnitude

Experimentation with different load magnitudes showed that, despite the technically nonlinear nature of the problem, the model predicted a linear relationship between the deformation at any given location and the magnitude of the longitudinal load. Because of this linear relationship, the relevant measurements S1, S2, X, etc. are presented as strain (or extension) per kilonewton of applied longitudinal force, referred to in this thesis as the "strain coefficient" (or "extension coefficient").

Strain gauges and extensometers measure the change in deformed shape between two points in time; the change in load must also be measured. In an actual in-track IJ, this could most easily be accomplished by placing appropriately-oriented strain gauges at the neutral axis of the rail near the joint bars. Note that knowledge of the absolute stress state

or rail neutral temperature is not required, again owing to the approximately linear nature of the deformation / load relationship.

3.5 Effect of debonding on joint bar strain and rail gap extension

Chapter 2 described the typical shapes of the debonded region. Debonding begins near the endpost and grows outward. The exact shape of the debonded region varies, often extending farther along the bottom side of the rail head and the top side of the rail base than along the rail web. One end of the joint typically has more debonding than the other end, but there is no significant difference in the debonded area of the field and gauge sides.

The first case to consider is the simplest one, where the debonded region takes on a rectangular, symmetrical shape. “Rectangular” means that debonding extends equally far on the head, web, and base sections of the rail / joint-bar interface. In terms of the symbols introduced in Chapter 2, rectangular implies that $H = W = B$. Furthermore, the debonded region can be described in terms of either the area of the debonded region or the distance from the endpost to the edge of the intact bond. “Symmetrical” means that the pattern is the same on both ends of the joint. Symmetrical debonding can be modeled using a single rail / joint-bar interface, which greatly reduces the computation time.

Joint bar strain

Figure 3.3a shows a contour plot of the strain in one-half of one joint bar when a fully-bonded IJ is subject to a 180 kN tensile load. The other three joint bar halves would have the same pattern due to symmetry. Figures 3.3b through 3.3d show the predicted strain contours with 18,000 mm^2, 54,000 mm^2, or 100,000 mm^2 of epoxy debonding extending symmetrically from the endpost. These numbers include debonding on all four rail / joint-bar interfaces, not only the one modeled. The inside face of the joint bar has an approximate length from top to bottom of 175 mm; therefore, the debonded areas represent a distance from endpost to intact epoxy bond of 25, 75, and 140 mm, respectively. The shaded areas superimposed on the plots indicate the debonded region, and the strain gauge locations A1, A2R, and A3R are labeled.

Figure 3.4 shows the predicted strain coefficients S1, S2, and S3 for different amounts of rectangular, symmetrical debonding. In this symmetrical case, S1, S2, and S3 are equal to the strain at A1, A2R, and A3R divided by the input load. Generally speaking:

1.) Debonding causes increased strains on the outside surface of the joint bar.
2.) The amount of debonding required to affect the strain at a certain location increases with the distance from the endpost to that location. S1 is more affected by small amounts of debonding than S2, and S2 is more sensitive to small and moderate amounts of debonding than S3.
3.) Comparing the results to Figure 3.2, strains S1 and S2 appear to reach a maximum once debonding extends about 75 mm past the location of the strain gauges.

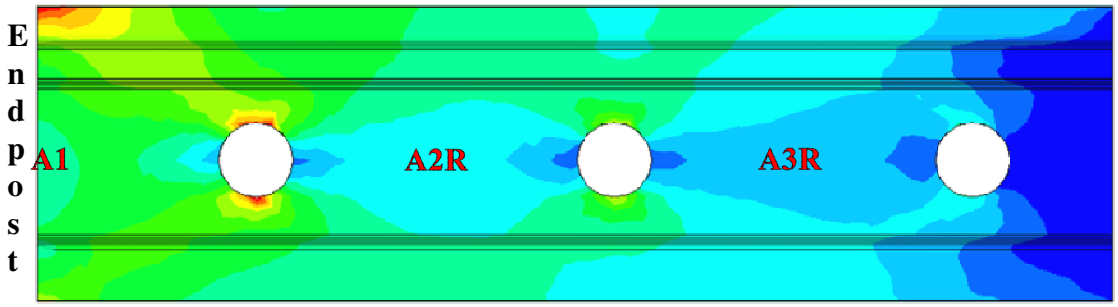
End post
A1
A2R
A3R

(a)

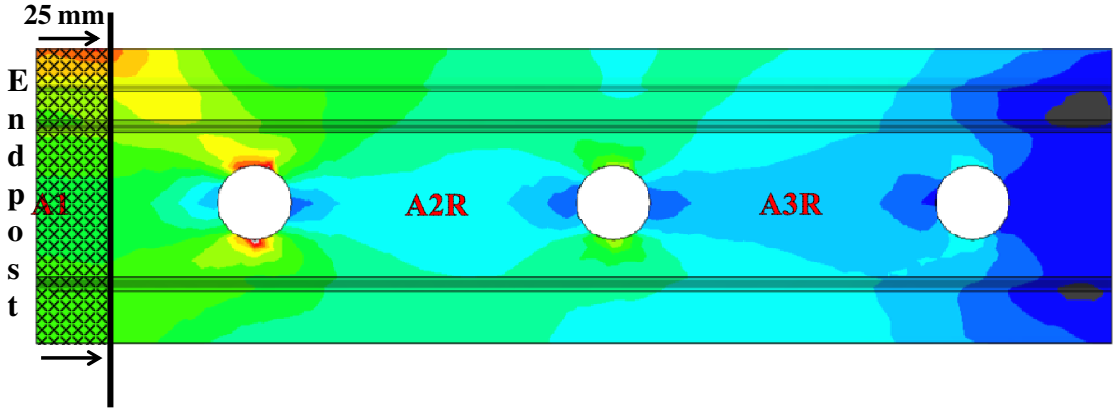
25 mm
End post
A1
A2R
A3R

(b)

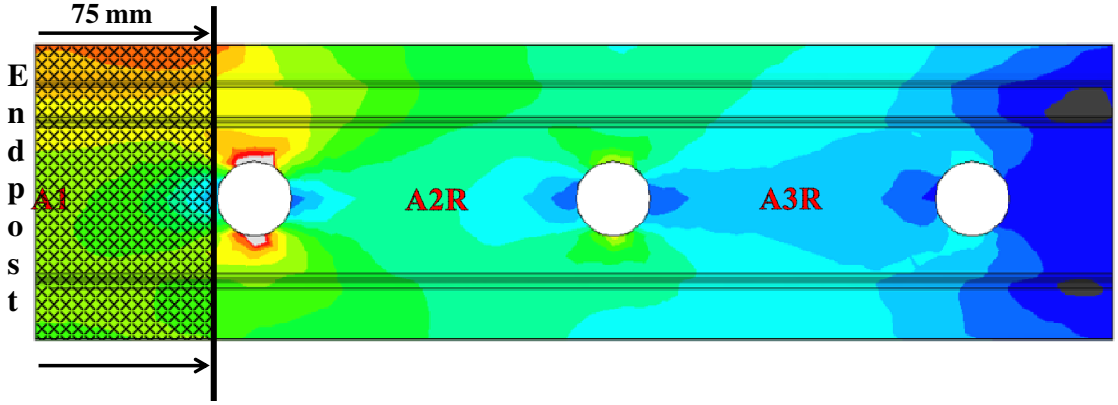
75 mm
End post
A1
A2R
A3R

(c)

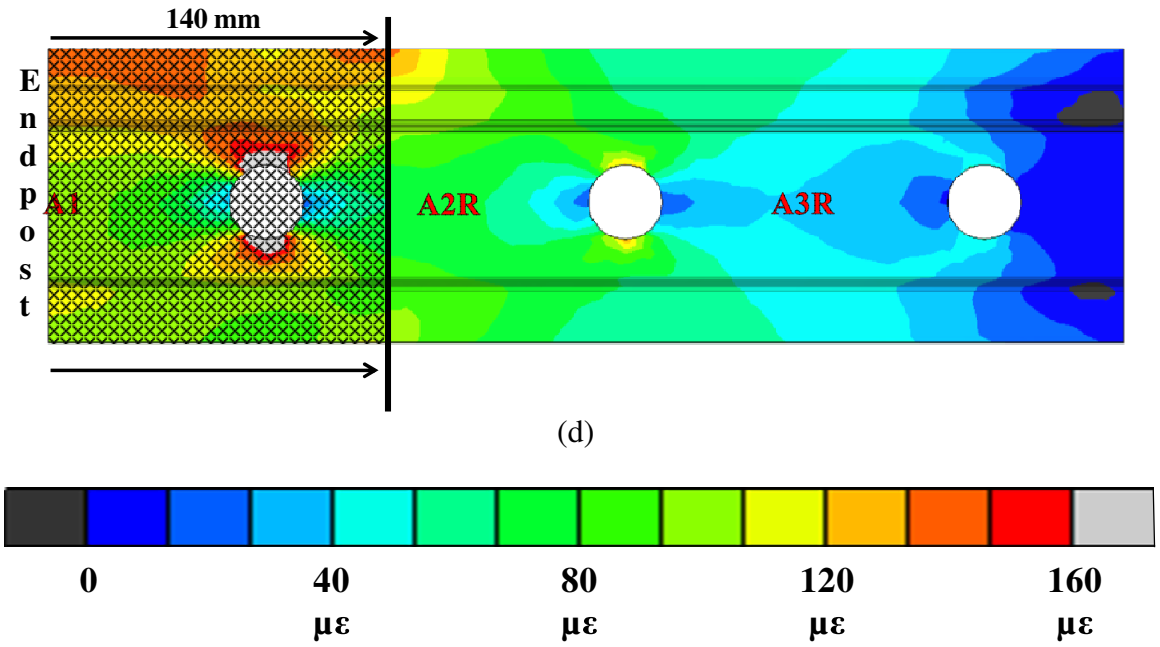

Figure 3.3: Strain contours in joint bar. 180 kN tension load, rectangular symmetrical debonding. (a) Fully bonded joint. (b) 18,000 mm^2 debonding. (c) 54,000 mm^2 debonding. (d) 100,000 mm^2 debonding.

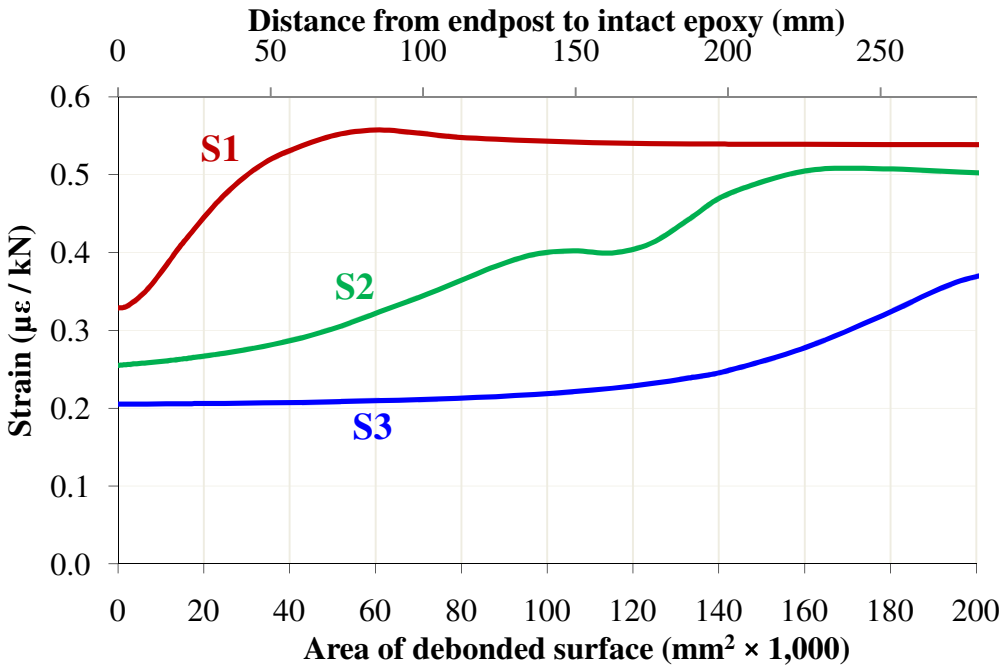

Figure 3.4: Strain coefficients S1, S2, and S3 as a function of rectangular, symmetrical debonding.

The results for S2 and S3 are straightforward. The entire longitudinal load must be transferred from the rail to the joint bar within the area of intact epoxy. The majority of the load transfer actually occurs near the edges of the intact epoxy layer (Himebaugh et al. 2007). For this reason, the amount of force carried by the joint bars at A2R or A3R is not much affected by small amounts of debonding. Furthermore, because shear stresses are relatively low in epoxy near these locations, stress on the inside surface is about the same as stress on the outside surface. On the other hand, as the debonded region grows and the edge of the epoxy approaches A2R or A3R, the joint bar at that location starts to bear a greater portion of the load, increasing the strain.

The increase in S1 requires a different explanation. Simple force-balance equations imply that the total tensile force over the cross-sectional area of the joint bar is constant at the rail gap, regardless of debonding. The increased strains at A1 due to debonding result from a change in the distribution of stress across the joint bar cross-section. Figure 3.5 shows how the stress distribution at the center of the joint bar changes as debonding progresses to about 75 mm from the endpost. Stress that is concentrated near the inside surface of the joint bar in a fully bonded joint becomes more evenly distributed in the lateral direction as the debonded region grows. After the debonded region extends 75 mm from the endpost, further debonding does not affect the stresses over this cross-section, and the strain at A1 stops increasing. This local stress distribution also explains why the strain at locations A2R and A3R continues to increase after the line of intact epoxy has progressed slightly past the gauge location.

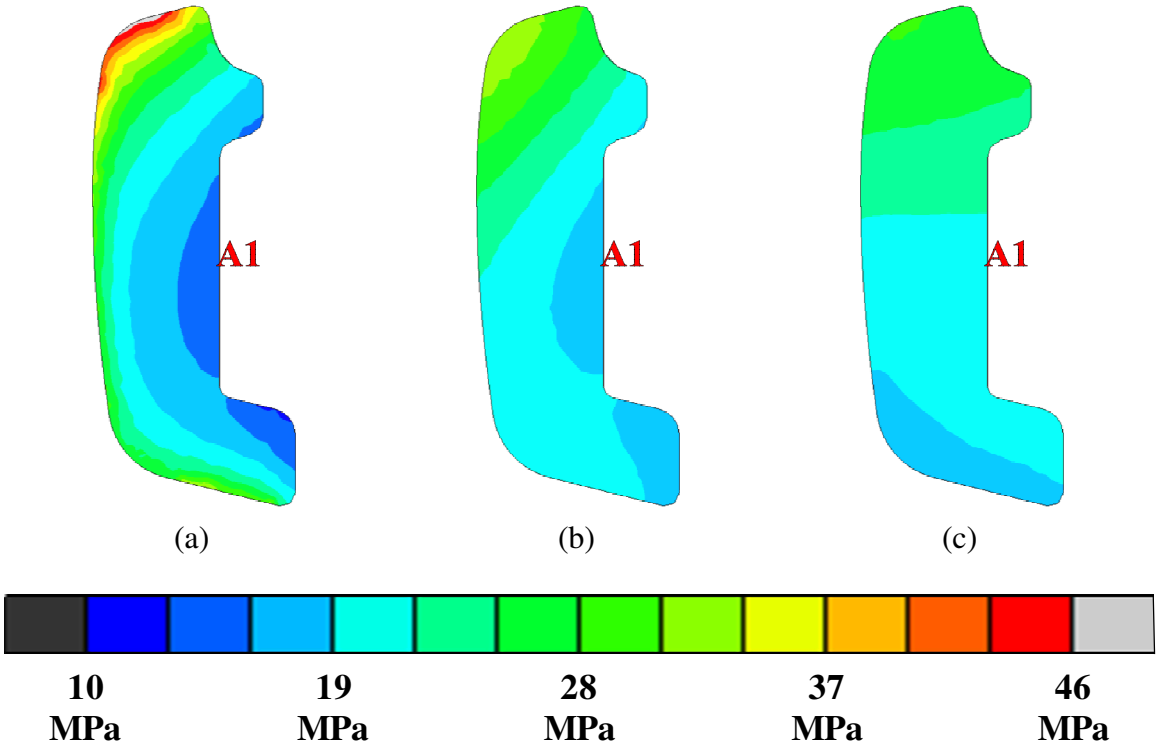

Figure 3.5: Longitudinal stress at center of joint bar. 180 kN tension load, rectangular symmetrical debonding. (a) Fully bonded joint. (b) 18,000 mm^2 debonding. (c) 54,000 mm^2 debonding.

Rail gap extension

Figure 3.6 shows the elastic relative movement between the two rail ends as measured by the extension coefficient X for different amounts of rectangular, symmetrical debonding under a tensile load. Any loss of bond near the endpost causes the relative movement to increase. Furthermore, it continues to increase with large amounts of debonding. This gives X an advantage over joint bar strains as an indicator of debonding, because each location on the joint bar is sensitive only to debonding within a certain region. As noted previously, however, X has the disadvantage of being sensitive to non-longitudinal forces that might develop in the rail, due to its location far from the neutral axis.

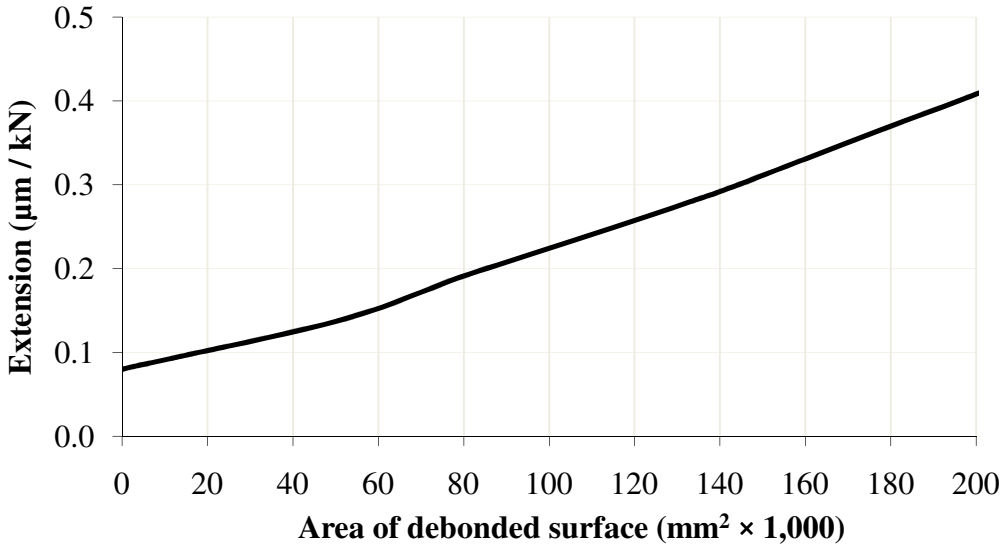

Figure 3.6: Extension coefficient X as a function of rectangular, symmetrical debonding.

3.6 Effect of irregular debonding patterns

The preceding section assumed a rectangular, symmetrical debonded area extending outward from the endpost toward the edges of the joint bar. As noted in Chapter 2, the actual debonded region varies from joint to joint. The accuracy of debonding estimates based on deformation measurements will suffer if the relationship between debonded area and deformation is highly dependent on the unknown shape or distribution of the debonded area. Therefore the effects of common variations on the predicted deformation measurements must be considered.

Extra debonding on the head and base surfaces

When an IJ is subjected to a vertical wheel load, stress in the epoxy layer is concentrated at the top and bottom of the interface, where it is adjacent to the bottom side of the rail head and the top side of the rail base (Himebaugh et al. 2007). Perhaps because of this, and perhaps because of greater exposure to water infiltration, the debonding along these surfaces is often more extensive than the debonding along the web. The analysis in Chapter 2 showed that, on average, debonding extends about 30 mm farther near the top and bottom of the rail / joint-bar interface (measurements H and B) than along the section adjacent to the rail web (W), and differences as large as 75 mm were not uncommon.

Figure 3.7 compares the effects of this difference versus the original, rectangular shape for measurements S1, S2, and X. The solid lines, taken from Figures 3.4 and 3.6, show the curves for the rectangular, symmetrical case. The dotted lines show the results of debonding that starts on the head and base, extends out to 25 mm on those surfaces, and then grows equally along the head, base, and web. The dashed lines represent debonding that begins on the head and base and extends 75 mm out from the endpost before proceeding equally along the three surfaces. Note that the difference between the rectangular, symmetrical case and the case with $H - W = B - W = 25$ mm is generally small. On the other hand, a 75 mm difference does matter: increases in H and B do not affect S1 and S2 as much as they affect the total debonded area. Because such cases appear to be the minority, the rectangular symmetrical curve will be used as the basis for making inferences about the debonded area. However, for the minority of IJ's that do have large values of $H - W$ and $B - W$, the estimated debonding based on measurements S1 and S2 will be lower than the actual debonding.

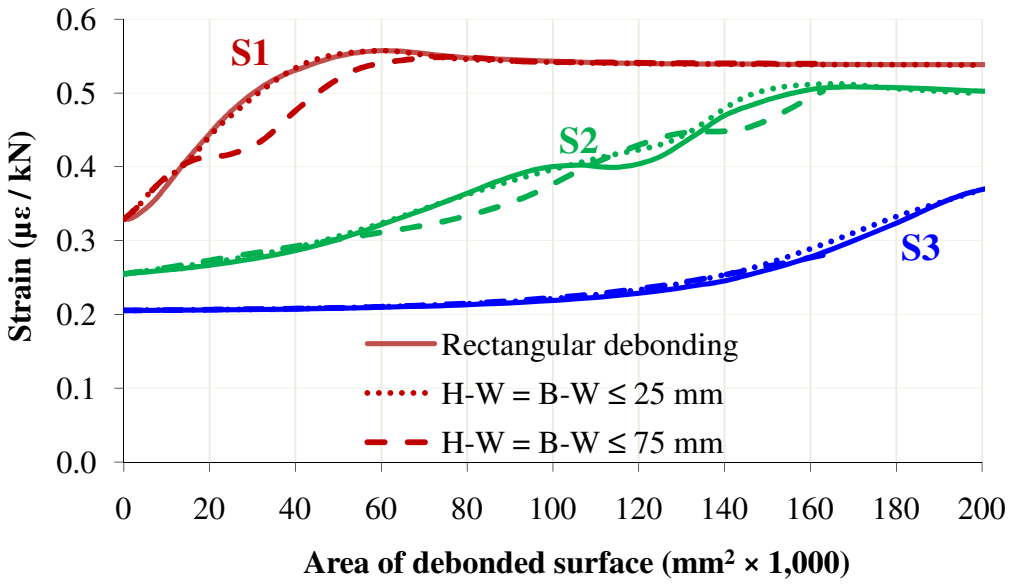

(a)

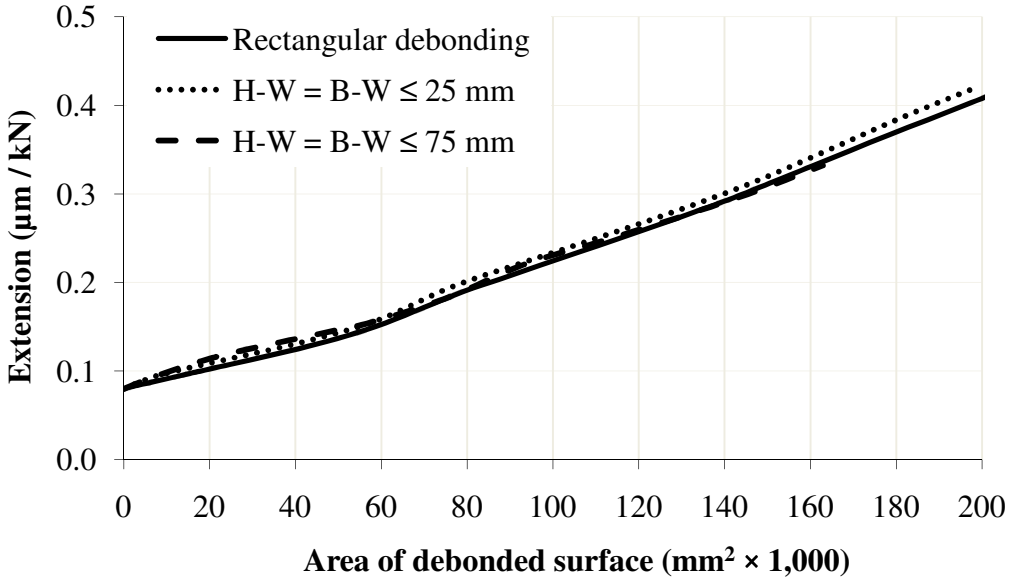

(b)

Figure 3.7: Deformation when debonding is more extensive on head and base than on web. (a) Joint bar strain coefficients. (b) Rail gap extension coefficient.

The X metric, like S1 and S2, is mostly unaffected by $H - W$ and $B - W$ values of 25mm. On the other hand, when the total debonded area is small, $H - W$ and $B - W$ values of 75 mm cause X to be higher than it would for a rectangular debonded region

with the same total area. For these cases, the estimated debonded area based on the X measurement would be higher than the actual area.

More debonding on one end

Chapter 2 also noted that the debonded area is often greater on one end of the joint than the other. On average, one end had about 58% of the total debonded area. As noted above, strains on the exterior surface of the joint bar depend on two factors: the total force carried in a particular part of the joint bar, and the stress distribution across the joint bar section at that location. For locations sufficiently far from the endpost, neither of these factors will be affected by debonding on the opposite end of the joint. For instance, A2R and B2R will not be affected by debonding on the L end of the joint. Therefore, the measurements S2L, S2R, S3L, and S3R can be considered representative of the debonded area on one end of the joint only. Using S2R to estimate the debonding area may result in an estimate that is either too high or too low, depending on whether the R side has more or less debonding than the L side. Using S2L would have the opposite effect. On the other hand, the average of the estimates produced by S2R and S2L would be very close to the actual debonded area.

S1 and X have the potential to be affected by debonding on either end. A series of scenarios were considered in which debonding was 50% more extensive on one rail end than on the other. For these scenarios, the relationships between S1 and X and the total debonded area were found to be the same as in the symmetrical case. These

measurements were affected only by the total debonded area, not by the distribution of that area over the ends.

Debonding at the ends of the joint bar

When an IJ is subjected to wheel loads, high epoxy stresses also develop near the outer edges of the joint bars, far away from the endpost (Himebaugh 2007). In some cases debonding can also occur in this region. As noted in Chapter 2, the extent of this debonding is small compared to debonding near the endpost.

Small debonded regions at the outer edges of the joint have no effect on S1, S2, or X, because such debonding causes little change in either the total load in the joint bar or the local stress distribution at those locations. The only measurements affected by such debonding are A3L, A3R, B3L, and B3R, which will start to decrease as the debonded region reaches about 50 mm away from the edge of the joint bar. It is shown in section 3.7 that, for debonding extending outward from the endpost, these measurements do not start to increase by a useful amount until the debonded area is larger than 150,000 mm^2. Unfortunately, joints with large amounts of debonding extending from the endpost are also presumably the most likely to have significant amounts of debonding near the edge of the joint bar. Therefore debonding in the two regions will tend to cancel each other out, preventing A3L, A3R, B3L, and B3R from being useful for estimating debonding in either region.

Consequently, inferences about the debonded area will be made using only the S1, S2, S2L, S2R, and X coefficients, which are insensitive to edge debonding. Only

debonding extending from the endpost outward will be included in the estimated debonded area.

3.7 Estimating debonding from measured deformation

Previous sections describe the deformations that would result from a given amount of debonding. This knowledge must be turned into an algorithm for making inferences about the amount of debonding based on the measured deformation. Such an algorithm will compare the value of one or more deformation measurements to the appropriate debonding versus deformation curves in Figure 3.4 or 3.6. Depending on which strain or extension coefficient is used, the estimate may be more or less accurate. The usefulness of each measurement can be studied by considering its "sensitivity".

Sensitivity

The sensitivity of a certain strain or extension coefficient is defined as its derivative with respect to the area of the debonded region. Sensitivity determines the precision of any inferences made using that coefficient: the estimate produced by a high-sensitivity coefficient will not be greatly affected by small measurement errors. The sensitivity of each coefficient, like the coefficient itself, is a function of the total debonded area.

The sensitivity of measurements S1, S2, and S3 is graphed in Figure 3.8a. Because these three measurements have the same units and would be measured with

identical 6.35 mm strain gauges, the sensitivities can be compared directly. S1 is the most sensitive to changes in debonding until the total debonded area reaches about 47,000 mm^2. After that, S2 is the most sensitive until debonding reaches about 150,000 mm^2. There is a gap (between about 100,000 and 120,000 mm^2) where none of the three locations have particularly good sensitivity, so any estimates based on joint bar strains will have trouble distinguishing between these areas. For the rectangular, symmetrical case, this corresponds to debonding that extends about 150 mm away from the endpost – the location of gauges A2L, B2L, A2R, and B2R.

S3 becomes the most sensitive measurement when the debonded area exceeds about 150,000 mm^2. As described in section 3.6, because of the possibility of debonding near the edge of the joint bar, S3 is unlikely to be useful for estimating debonding. The sensitivity of S2 drops to zero at around 160,000 mm^2. Therefore the finite element model suggests that it will be impossible to distinguish between debonded areas larger than about 160,000 mm^2 using the joint bar strain measurements considered in this study.

The total area of the bonded surfaces in a new IJ is about 320,000 mm^2, but only one of the six test specimens in Chapter 2 had 160,000 mm^2 or more of debonding. It is likely that joints with this much debonding are already in danger of suffering complete epoxy failure under high tensile loads. Therefore the upper limit on the range of debonding estimates using joint bar strain measurements is probably high enough to track most of the progressive portion of the epoxy deterioration.

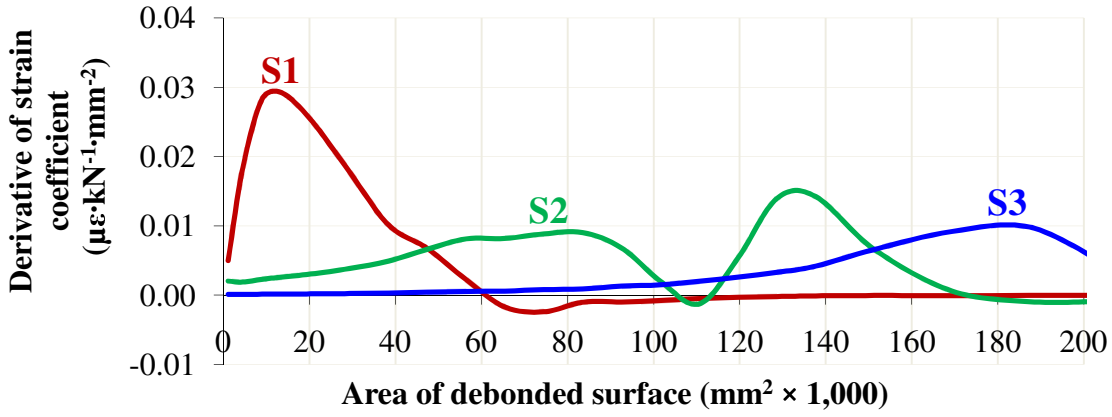

(a)

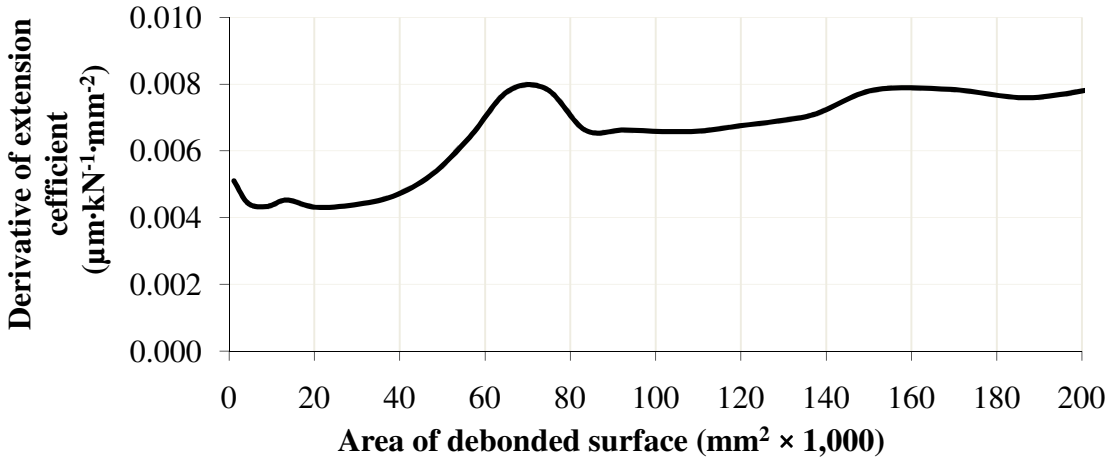

(b)

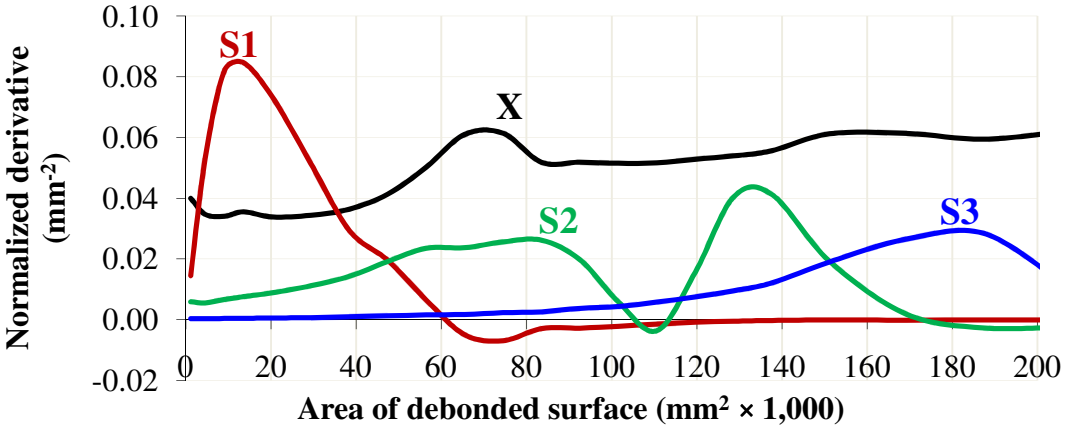

(c)

Figure 3.8: Derivative of strain and extension coefficients with respect to area of the rectangular, symmetrical debonded region. (a) Joint bar strain coefficients. (b) Rail gap extension coefficient. (c) Derivative divided by coefficient value when debonded area is 45,000 mm^2.

Because the derivative of strain with respect to debonding is mostly non-negative, it is possible to use strain rather than debonding to define the range over which a particular measurement is sensitive. S1 is the most sensitive measurement if debonding is less than 48,000 mm^2. If the debonding is greater than 48,000 mm^2, S1 is never less than 0.53 με / kN (Figure 3.4). Therefore, if S1 is less than 0.53 με / kN, it is in its "sensitive" range, and should give accurate estimates of the debonded area. If S1 is greater than 0.53 με / kN, then the debonded area is at least 40,000 mm^2; but if the area is this large, then S2 is sensitive to further increases in debonding (Figure 3.8a). Therefore, if S1 is less than 0.53 με / kN, its value is indicative of the debonded area; if it is greater than 0.53 με / kN, S2 will provide a better estimate. On the other hand, if S2 exceeds 0.50 με / kN, then the debonded area is greater than 160,000 mm^2 (Figure 3.4). For such large areas, S2 also has low sensitivity (Figure 3.8a).

Unlike joint bar strains, the sensitivity of the extension measurement X is more consistent over the range studied (Figure 3.8b). As noted previously, this suggests that the single extension measurement could be used to measure a wide range of different debonded areas, in contrast to the larger set of sensors needed for joint bar strains.

To compare the sensitivities of the joint bar strain coefficients with that of the rail gap extension coefficient, they must be normalized to account for the different units and measurement devices. This is accomplished by dividing the sensitivity of each coefficient by the coefficient value at some useful point. Figure 3.8c shows the sensitivity normalized to the value expected with a moderate amount (45,000 mm^2) of debonding. Using this comparison, the extensometer is more sensitive than the strain gauges, except in early stages of debonding, where S1 provides a more sensitive measurement.

Which measurements to use

Because the extension measurement X has consistently high sensitivity, a sensor system that uses two extensometers (AX and BX) would appear to be capable of estimating the debonded area. Such a system would likely be less expensive than a system using strain gauges on the joint bars, which would require six sensors (A1, B1, A2L, A2R, B2L, and B2R) to achieve sensitivity over a wide range of debonded areas. Furthermore, the extension measurements, unlike the joint bar strains, are sensitive even when the debonded area is greater than 160,000 mm^2. The caveat is that X would be affected by any vertical bending moments present in the rails when the measurements are taken. It is unclear whether this would be a serious consideration in the field. If vertical bending moments develop that are not predictably linked to the longitudinal tensile load, they will introduce a confounding variable into the relationship between rail gap extension and debonding. A system based on joint bar strains would avoid this difficulty.

It should be noted that, regardless of whether the system uses rail gap extension or joint bar strain, some means of estimating the change in tensile load between two points in time, such as a strain gauge on the rail web, must also be employed. On the other hand, the finite element model suggests that the strain measurements A3L, A3R, B3L, and B3R are not useful for estimating the debonded area, and need not be included in a sensor system.

Arriving at a single estimate of the debonded area

The exact procedure for estimating the total surface area of the debonded region depends on the set of sensors used. A system that uses extensometers AX and BX would estimate the debonded area (excluding any debonding near the outer edges of the joint bars) using the following algorithm:

1.) Calculate the extension coefficient X, which is the average of the change in AX and BX since some previous point in time divided by the change in tensile load: $X = (\Delta AX + \Delta BX) / (\Delta P_{tens})$

2.) Draw a horizontal line through the point on the Y-axis of Figure 3.6 corresponding to the measured X. Find where this line intersects the curve, and draw a vertical line from this intersection down to the X-axis. This point on the X-axis is the estimated debonded area.

A system consisting of strain gauges A1, B1, A2L, A2R, B2L, and B2R would use a similar algorithm:

1.) Calculate strain coefficients S1, S2L, and S2R from the changes in strain and the change in tensile load.

2.) If $S1 < 0.53$ με/ kN, proceed as above, using the curve labeled S1 in Figure 3.4.

3.) Otherwise, draw horizontal lines through the Y-axis of Figure 3.4 corresponding to the measured values of S2L and S2R. Find where these points intersect the curve labeled S2, and draw vertical lines from the intersection points down to the X-axis. The estimated debonded area is the average of these two values.

3.8 Examples

Table 3.2 shows two examples of possible debonded regions for a typical IJ. These patterns both have more debonding on the head and base of the rail than on the web – slightly more than the average difference given in Chapter 2. They also have approximately 1.5 times as much debonding on the R end as on the L end.

Table 3.2: Debonded region for Examples 1 and 2. Extent measured in mm from endpost to intact epoxy; area measured in mm^2 × 1,000.

		Example 1		Example 2	
End	Surface	Extent	Area	Extent	Area
Left	Web	10	1.7	86	15.1
Left	Head, Base	60	10.0	124	20.7
Right	Web	29	5.0	137	24.1
Right	Head, Base	79	13.3	175	29.2
Left	All		11.8		35.8
Right	All		18.3		53.3
Both	All		30.1		89.1

According to the finite element model used in this study, when IJ's with these debonded regions are subjected to longitudinal loads, the strain and extension coefficients would be as shown in Table 3.3. Suppose that these measurements are known, but the original debonding data (Table 3.2) are not. Can the debonded area be inferred from the strain coefficients?

Table 3.3: Finite element deformation results for Examples 1 and 2.

Strain coefficients	Example 1 (με / kN)	Example 2 (με / kN)
S1	0.473	0.546
S2L	0.276	0.344
S2R	0.290	0.402

Extension coefficient	Example 1 (μm / kN)	Example 2 (μm / kN)
X	0.126	0.215

The estimation procedure for Example 1 is shown in Figure 3.9. The actual debonded region modeled has an area of 30,000 mm^2. Because S1 < 0.53 με/ kN, S1 is used (Figure 3.9a) to arrive at an estimated debonded area of 25,000 mm^2. Alternatively, the extension coefficient X can be used (Figure 3.9b) to arrive at an estimate of 42,000 mm^2.

Example 2 has a debonded area of 89,000 mm^2. S1 > 0.53 με/ kN, so S2L and S2R are used instead of S1. Based on S2L, the estimated debonded area would be 71,000 mm^2; using S2R, it would be 117,000 mm^2 (Figure 3.10a). Averaging these together, the estimated debonded area is 94,000 mm^2. The estimated debonded area based on X would also be 94,000 mm^2 (Figure 3.10b).

In these examples, estimates of the debonded area were accurate to within ± 10,000 mm^2, or about 3% of the original bond area. This error is inherent in the procedure even if the finite element model is assumed to be a perfect representation of IJ mechanics; it results from the variability in the shape and distribution of debonded areas described in Chapter 2.

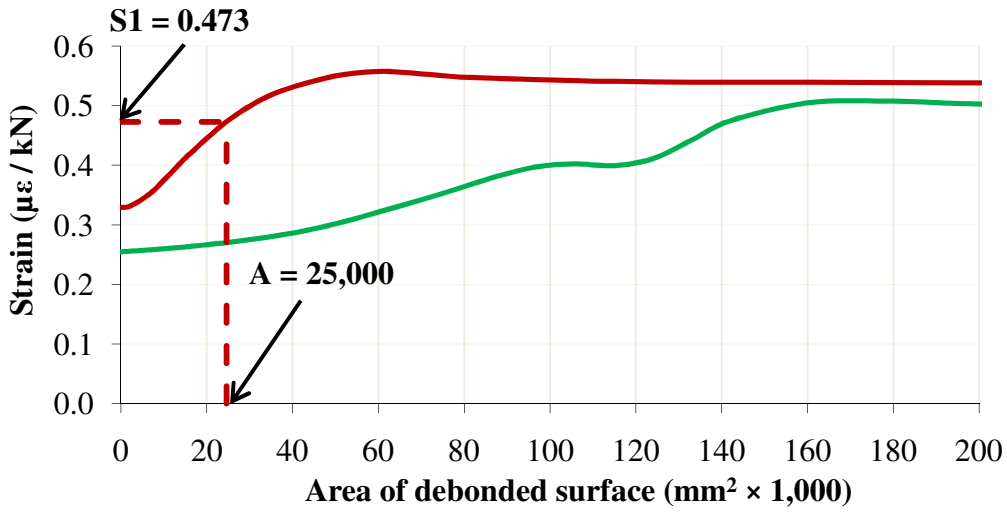

(a)

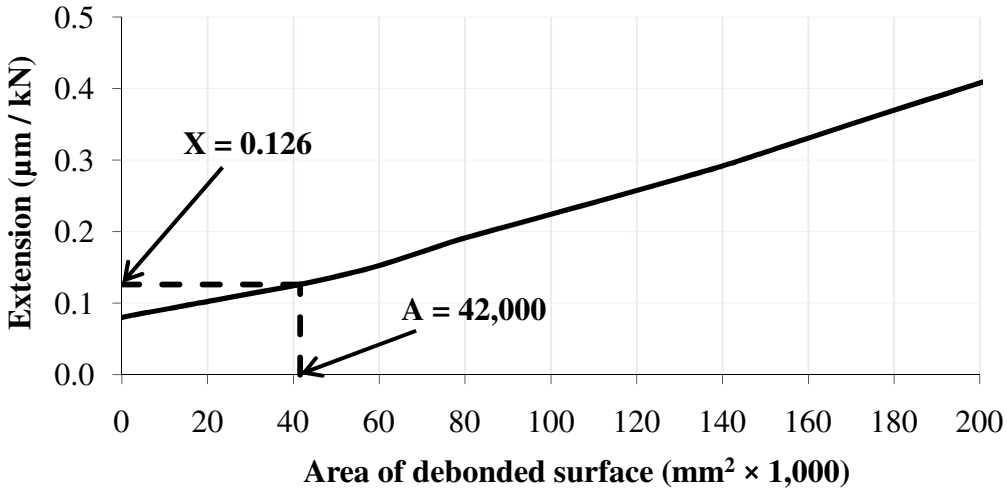

(b)

Figure 3.9: Estimating debonding for Example 1. (a) Using joint bar strain coefficients. (b) Using the rail gap extension coefficient.

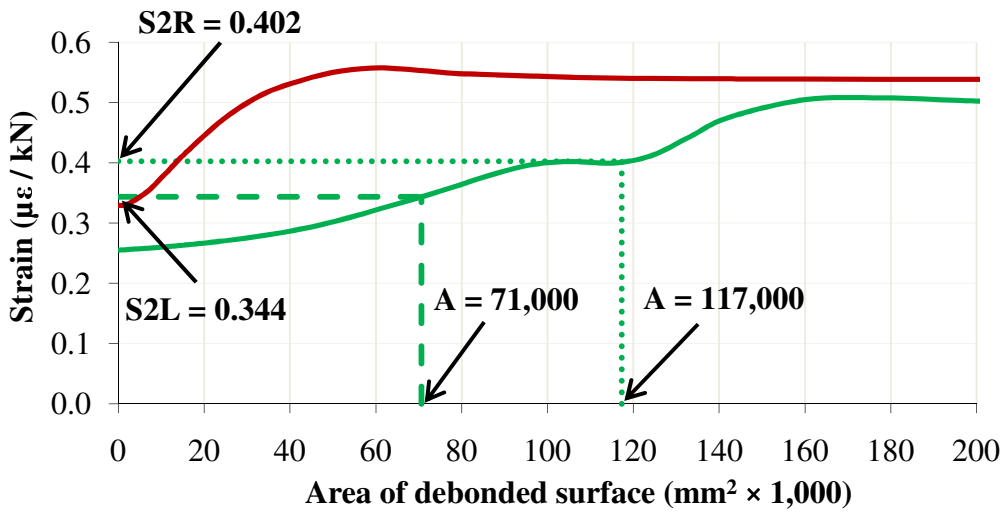

(a)

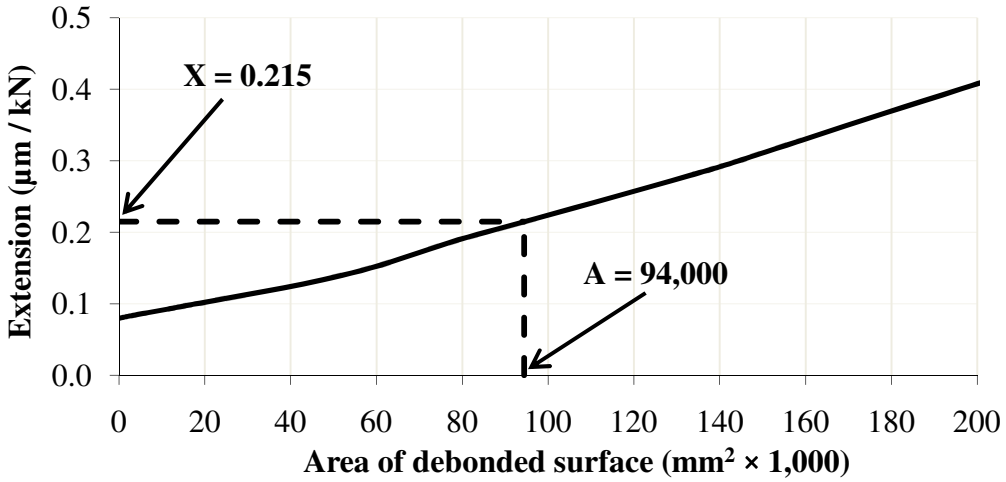

(b)

Figure 3.10: Estimating debonding for Example 2. (a) Using joint bar strain coefficients. (b) Using the rail gap extension coefficient.

3.9 Conclusions

The deformation of a bonded IJ under a tensile load changes based on the extent of epoxy debonding near the endpost. Computer modeling suggests that either of two approaches can be used to estimate the area of the debonded region based on measurements of IJ

deformation. These techniques could serve as the basis for a fully automated system for measuring the progression of epoxy debonding in a bonded insulated rail joint in track.

One approach measures strains at six locations on the outer surface of the joint bars. Small amounts of debonding lead to measurable increases in the strain at two of these locations. Larger amounts of debonding increase the strain at the other four locations. The other approach measures the small amount of elastic increase in the gap between the rail ends; the gap widens more under load when the debonded area increases. This technique uses two extensometers placed at the base of the rail. Both also require some additional means of measuring changes in the rail longitudinal load, such as a strain gauge on the web of the rail. However, assuming that the deformation has a linear relationship with the load magnitude, knowledge of the rail neutral temperature is not necessary.

Both techniques have limitations. The computer model suggests that errors in the estimate of the debonded area of at least 10,000 mm^2 will be common based on variability in the shape and distribution of the debonded region. Measurements using extensometers at the rail base have an additional limitation: the results will be distorted by any thermally-induced vertical bending loads in the rail. All these results are based on a relatively simple model that does not capture frictional forces along a debonded interface, and require empirical verification. This verification is the subject of Chapter 4.

CHAPTER 4: EXPERIMENTAL TESTS OF A TECHNIQUE FOR MEASURING EPOXY DEBONDING IN INSULATED RAIL JOINTS

4.1 Introduction

Chapter 3 described a nondestructive, automated method for estimating the surface area of the debonded epoxy within a bonded insulated joint (IJ). Because debonding changes the stress state and deformation of a joint under a given load, information about the state of the epoxy can be inferred using deformation sensors such as strain gauges and extensometers. Computer modeling suggests that a relatively small number of sensors placed at critical locations on the joint can provide an estimate of the debonded surface area, with a theoretical maximum accuracy of around ± 10,000 mm^2 out of a total bond area of 320,000 mm^2.

This chapter describes a set of experiments testing that proposed indirect measurement technique. These tests were conducted on a set of sample insulated joint specimens with varying amounts of debonding. The IJ's were subjected to longitudinal tensile loads, and their elastic deformation was measured at the critical locations identified by the computer model. The joints were then disassembled and the actual debonded areas determined by visual inspection of the interior surfaces. The specimens used, and the observations of the debonded regions after disassembly, were described in Chapter 2.

In this chapter, the relationship between the actual amount of debonding A_i or A_s (Chapter 2) and the deformation measurements is compared to the theoretical relationship predicted by the computer modeling described in Chapter 3. The output of the algorithm

for estimating the debonded area that was also described in Chapter 3 is compared to the actual debonded area, and some corrections are introduced based on the experimental data.

4.2 Literature review

Previous research on bonded insulated joints used a number of computer models that describe the response of an IJ to various loads (e.g. Chen and Kuang 2002, Wen et al. 2005, Kabo et al. 2006, Steenbergen 2006, Plaut et al. 2007, Himebaugh et al. 2007), but few had any published experimental verification. There are several papers describing empirical research into the dynamics of rail joints, but these did not consider bonded insulated joints or longitudinal loadings (AREA 1980, Jenkins et al. 1974, Suzuki et al. 2005). Several studies addressed the expected load environment and the failure modes of glued insulated joints, but did not relate their findings to the details of IJ mechanics (Davis et al. 2005, Akhtar and Davis 2007).

In the 1990's Cox and Kerr developed several relatively simple analytic models of the response of a bonded IJ to vertical loadings and performed some experimental verification (Cox 1993, Kerr and Cox 1999). Their research is relevant to the issues addressed in Chapter 6 and will be discussed there. They did not consider longitudinal loadings or the effects of epoxy debonding.

4.3 Test procedure

Specimens tested

The specimens used in the testing, including the semantics of the specimen names, were described in Chapter 2.

Strain and extension under longitudinal load

Each test sample was cut so that the total length of the IJ and attached rail was approximately 3 m. Longitudinal loads were then applied using a specially constructed test frame consisting of two reaction blocks, one 450 kN servo-hydraulic actuator, and a load cell (Figure 4.1). Fixtures were built to attach the ends of the test specimen to the frame. The actuator was free to swivel horizontally but restrained in the vertical direction. Although the system was designed to impart only tensile loads, measurements showed that small transverse and vertical bending moments developed at the specimen ends. The effect of these extraneous loads is discussed in Section 4.4.

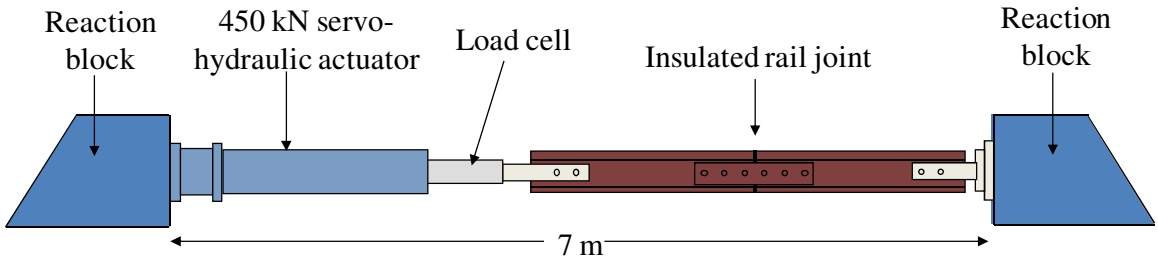

Figure 4.1: Tension testing frame.

Twelve 6.35 mm strain gauges and one 152.4 mm averaging extensometer were applied to the specimens, oriented longitudinally (Figure 4.2). Six strain gauges on the rails, outside the limits of the joint bar, measured the actual input loads to the joint. The other six strain gauges, labeled A1, B1, A2R, B2R, A3R, and B3R, were placed on the joint bars in line with the bolt holes, centered between the four innermost bolts. The averaging extensometer was placed across the gap between the rails, with one element on the A side and one on the B side; the reported value was the average extension in the two elements. This measurement gives a reasonable estimate of the extension measurement X defined in Chapter 3, despite the relatively long gauge length.

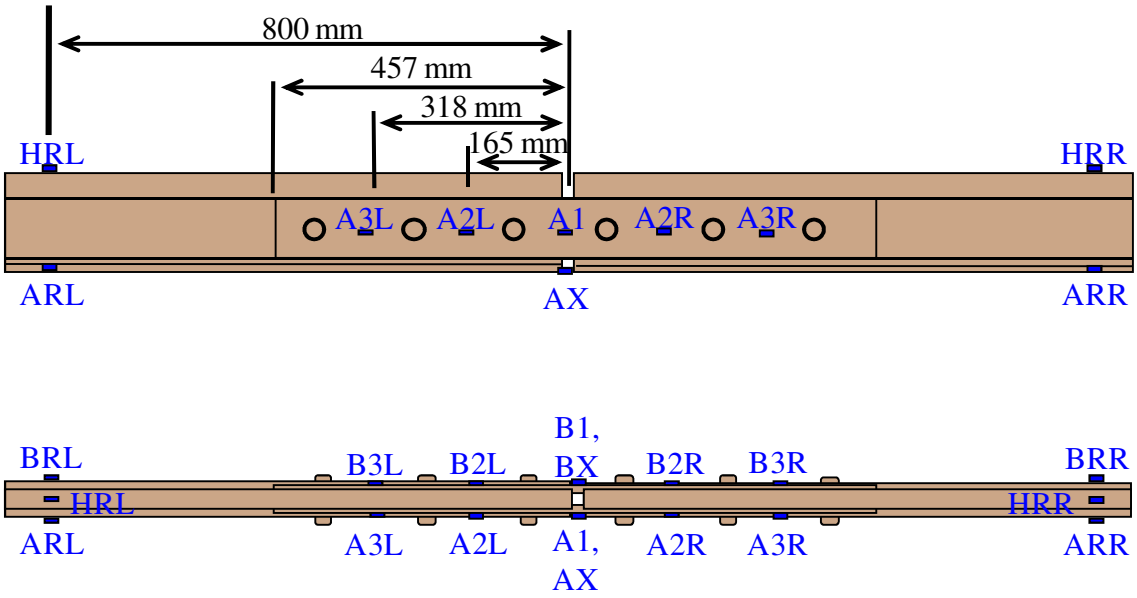

Figure 4.2: Sensor locations and names.

Longitudinal tensile loads of up to 400 kN were applied and released at a rate of between 5 and 20 kN per second, with several load cycles applied to each specimen. No

plastic deformation was observed, nor did the load rate have any noticeable effect. The resulting load / deformation curve is considered to be representative of static loading, exclusive of any long-term creep effects.

Destructive disassembly of the test specimens

After the load tests were completed, each test specimen was disassembled and inspected, and the debonded region measured according to both Inclusive and Strict criteria (Chapter 2).

4.4 Data processing and extraction

Asymmetrical deformation and unintended loadings

Figure 4.3a shows a typical load vs. strain curve for these tension tests. The two strains, A1 and B1, were measured at the center of the two joint bars (Figure 4.2). Note that the curves are not straight and the strains on the two joint bars were slightly different. This is because the forces actually imparted by the test frame were themselves nonlinear and asymmetrical. Both ends of the test specimen were somewhat constrained in the lateral, vertical, and rotational directions, allowing the test frame to impart lateral and vertical bending and cantilever forces into the specimen. This is evident from the strains in the rail outside the joint bar limits (Figure 4.3b): the strains at the bottom of the rail (ARL and BRL on the left rail; ARR and BRR on the right rail) were also nonlinear and asymmetrical.

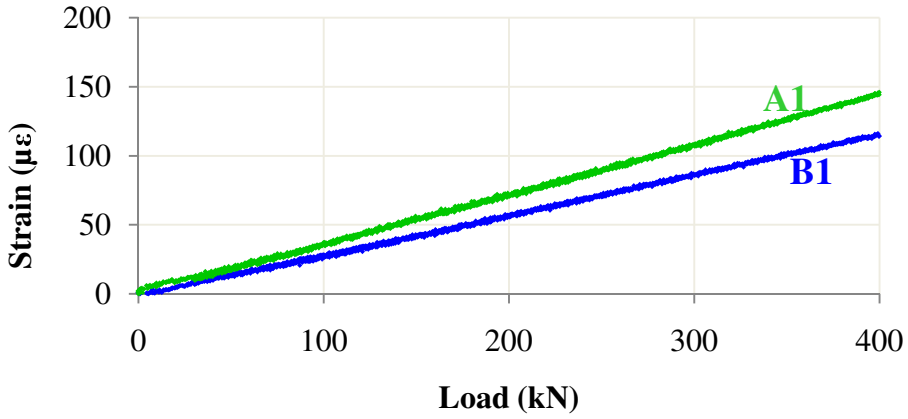

(a)

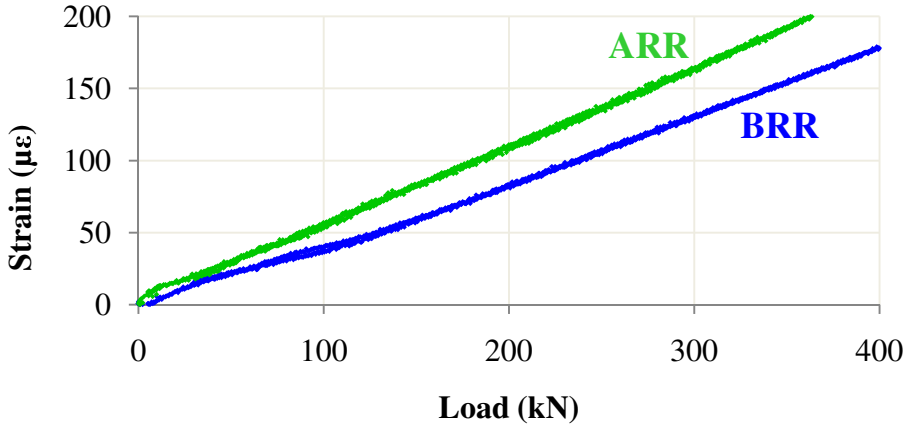

(b)

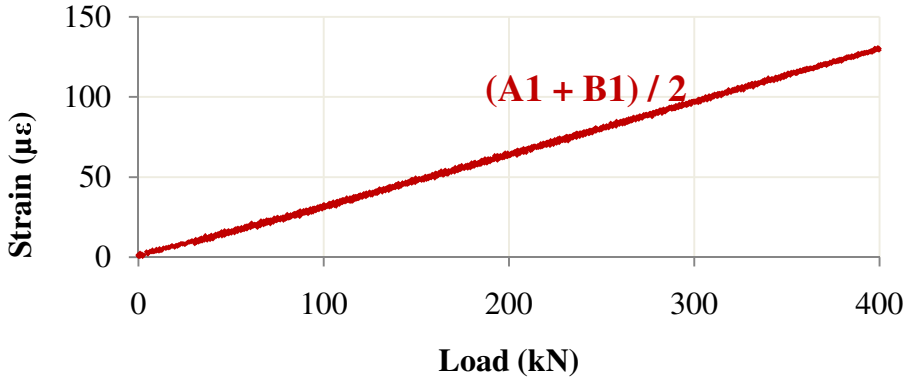

(c)

Figure 4.3: Strain versus load at various locations on specimen CA1. (a) A1 and B1. (b) RA and RB. (c) (A1 + B1)/2.

As suggested in Chapter 3, the strain in the two joint bars can be averaged together to produce a measurement that is relatively insensitive to applied lateral bending moments. In addition, because A1 and B1 are near the neutral axis of the joint bars, small vertical bending loads (such as those that might develop from thermal expansion or contraction) have little effect. The average of strains A1 and B1 is more linear relative to the applied tensile load than each individual strain (Figure 4.3c). For this specimen and this range of loadings, any change in the tensile load ΔF will produce approximately the same change in the average strain reading $(\Delta A1 + \Delta B1)/2$. The ratio of $(\Delta A1 + \Delta B1)/2$ to ΔF is the strain coefficient S1, defined in Chapter 3.

Unlike the joint bar strain gauges, the extensometer position X is not near the neutral axis of the joint bar and may be affected by vertical bending moments in the rail. To correct for the presence of vertical bending moments, a numerical adjustment was applied to the measured extensometer values. The actual applied vertical moment was measured using strain gauges on the rail outside the joint bar (HRL, ARL, BRL, HRR, ARR, and BRR). The amount of extension expected in a fully-bonded joint due to the applied bending moment was estimated using the finite element model from Chapter 3, and the result was subtracted from the raw extension measurements to produce the corrected values. This correction noticeably improved the linearity of extensometer results. Whether or not these corrections are needed in a measurement system depends on how much thermally-induced vertical bending moment develops in the field.

Linearity

A bonded insulated joint is a relatively complicated mechanical system, with numerous components that may come in and out of contact depending on how the system deforms. These contact surfaces interact via some combination of normal and friction forces. Furthermore, the epoxy / insulator layer itself probably has non-linear, anisotropic material properties. On the other hand, the algorithm given in Chapter 3 for estimating the debonded area depends on the assumption of a linear relationship between applied tensile loads and deformation. This assumption must be verified from the experimental data.

Recall that linearity was used to produce strain and extension coefficients from actual strain readings: $S1 = \Delta(A1 + B1) / 2\Delta F$, etc. Experimentally, the coefficients can be derived by fitting a linear model to the measured data: $(A1 + B1) / 2 = S1 \times F + r$, where r is a normally distributed random variable representing experimental error. The suitability of this model can be measured using the common goodness-of-fit measurement R^2. To avoid bias, this approach requires that the strain / load data points be evenly distributed over the range being studied. The nature of the servohydraulic controller used for the test is such that, in order to meet this condition, it is best to apply the regression only to data in the middle of the load cycle – between 45 kN and 390 kN of applied tension.

A linear curve was fit to the results from each control and test specimen. The minimum R^2 value for any reported strain coefficient – S1, S2L, and S2R – was 0.990, which occurred only for one coefficient of one specimen. All other R^2 values for joint bar

strains were above 0.997. The corrected extension measurement X was not quite as linear: all but one specimen had $R^2 > 0.978$, but the remaining specimen was much lower at 0.945. Nonetheless, these values were considered high enough to proceed on the assumption of a linear relationship between deformation and applied force over the range of tensile forces considered.

In some cases, especially for IJ's with greater amounts of debonding, some of the strain versus load curves showed significant hysteresis effects. Because the loading and unloading rates were identical in each test, the loading and unloading curves contain approximately the same number of data points. The curve-fitting procedure splits the difference between them and still produces a reasonably close fit. To achieve the same results using an in-track IJ subjected to thermal loads, the loading and unloading data would have to be balanced through careful data processing in order to achieve a consistent linear fit.

4.5 Results

Strain and extension coefficients

The strain and extension coefficients extracted from the raw data are presented in Table 4.1. Strain coefficients are given in units of microstrains per kN, and extension coefficients in micrometers per kN, as in Chapter 3.

Table 4.1: Strain and extension results.

Supplier	Specimen	Strain coefficients (με/ kN) S1	S2L	S2R	Extension coefficient (μm / kN) X
A	CA1	0.328	0.260	0.254	0.085
	TA1	0.447	0.297	0.313	0.137
	TA2	0.530	0.373	0.470	0.221
	TA3	0.515	0.336	0.300	0.151
B	CB1	0.317	0.249	0.250	0.065
	TB1	0.384	0.283	0.273	0.070
	TB2	0.427	0.276	0.280	0.066
	TB3	0.515	0.408	0.380	0.191

Comparison to finite element predictions

In Chapter 3, finite element analysis was used to predict the relationships between strain or extension coefficients and the size of the debonded area. Strain coefficient versus debonding curves were presented for a single type of IJ. Laboratory specimens consisted of two different types of IJ's (from suppliers A and B), with different joint bar shapes. Although the strain curves for both types of joints are similar, for maximum accuracy both were modeled and the test results for each specimen compared to the appropriate model. The only difference between the two models was the shape of the joint bars and the resulting shape of the epoxy layer.

The measured strain and extension coefficients were compared to those predicted by the computer model (Figures 4.4 - 4.6). Alternative versions of the data based on the Inclusive and Strict definitions of debonding are included in the plots.

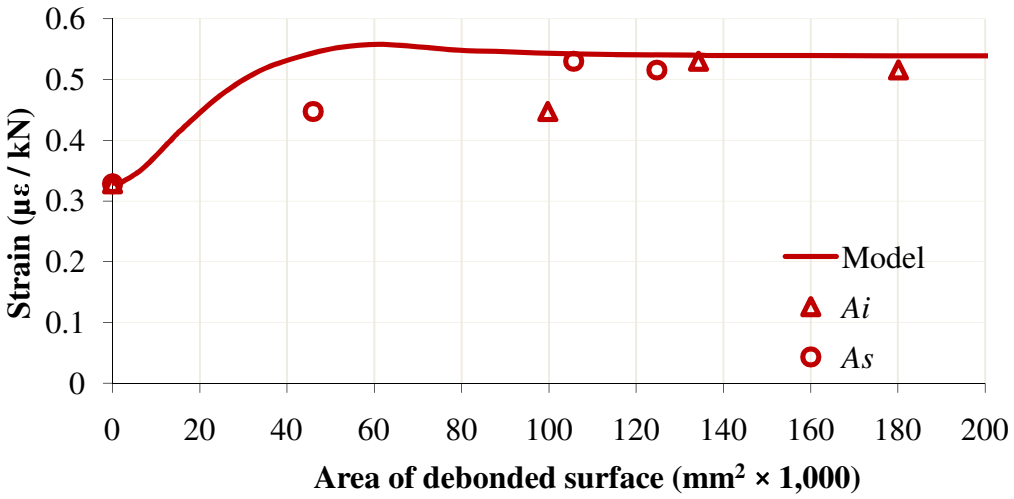

(a)

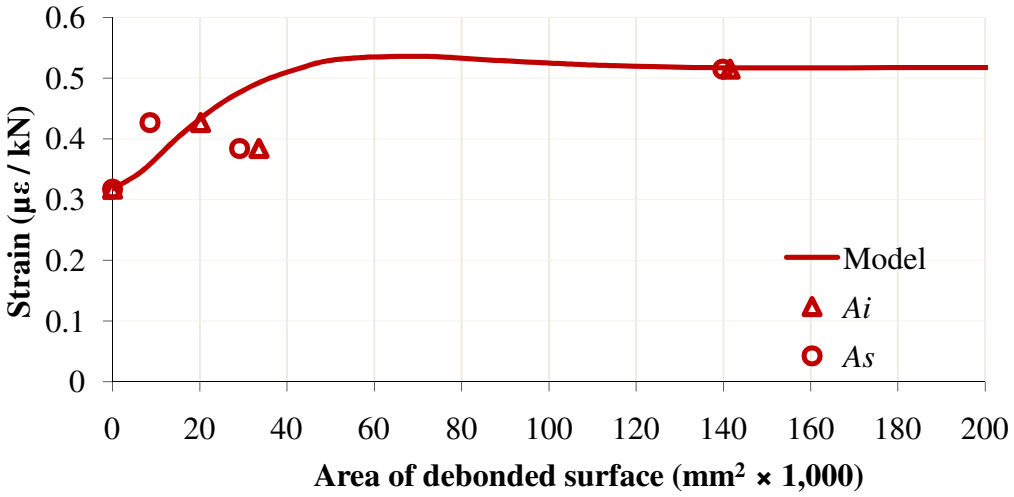

(b)

Figure 4.4: Predicted versus actual strain coefficient S1 as a function of debonding. (a) Supplier A. (b) Supplier B.

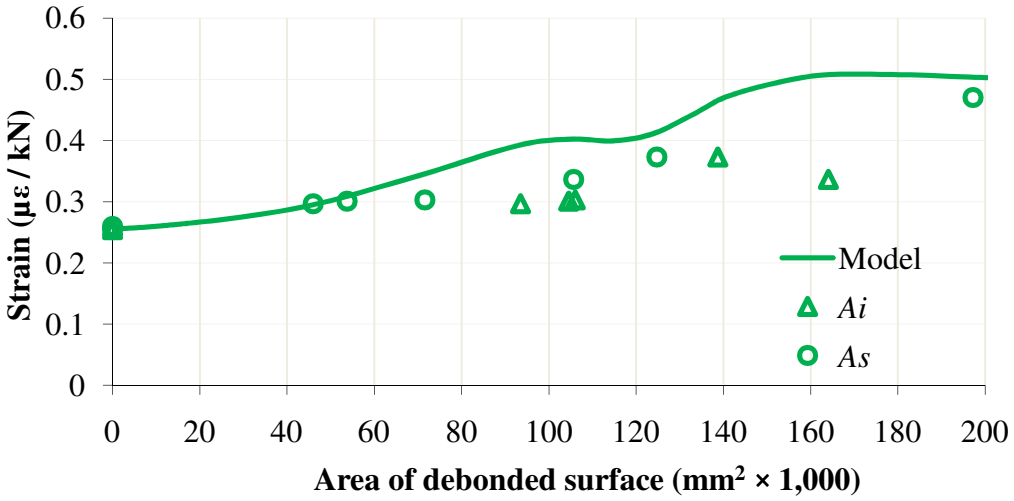

(a)

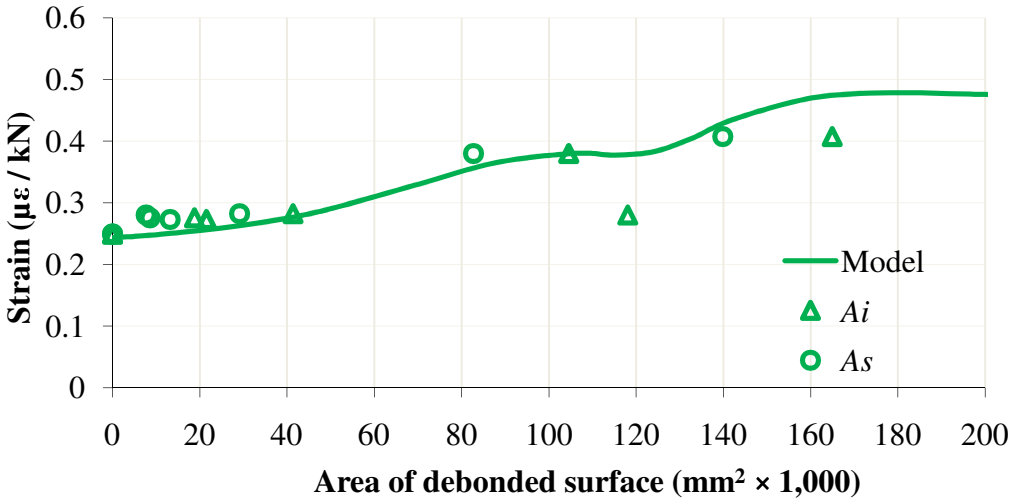

(b)

Figure 4.5: Predicted versus actual strain coefficients S2L and S2R as a function of debonding. (a) Supplier A. (b) Supplier B.

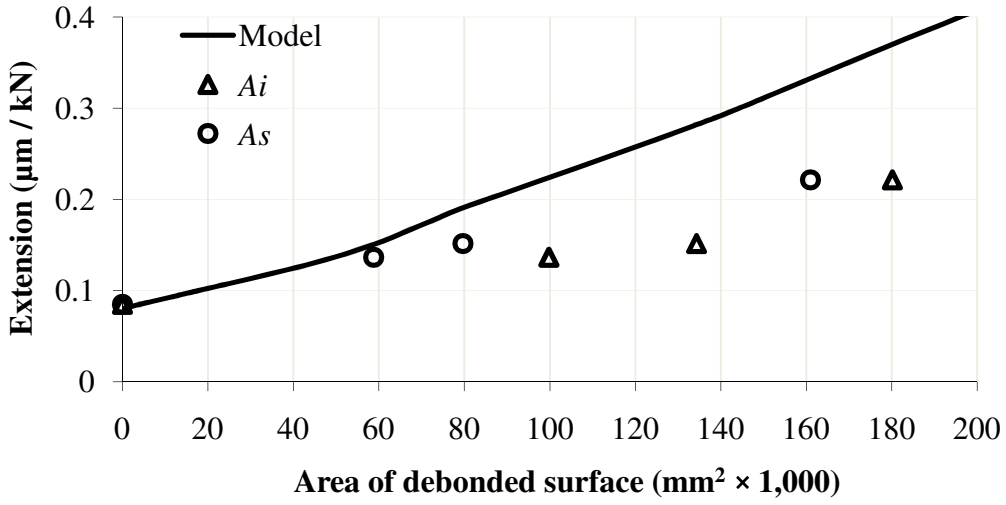

(a)

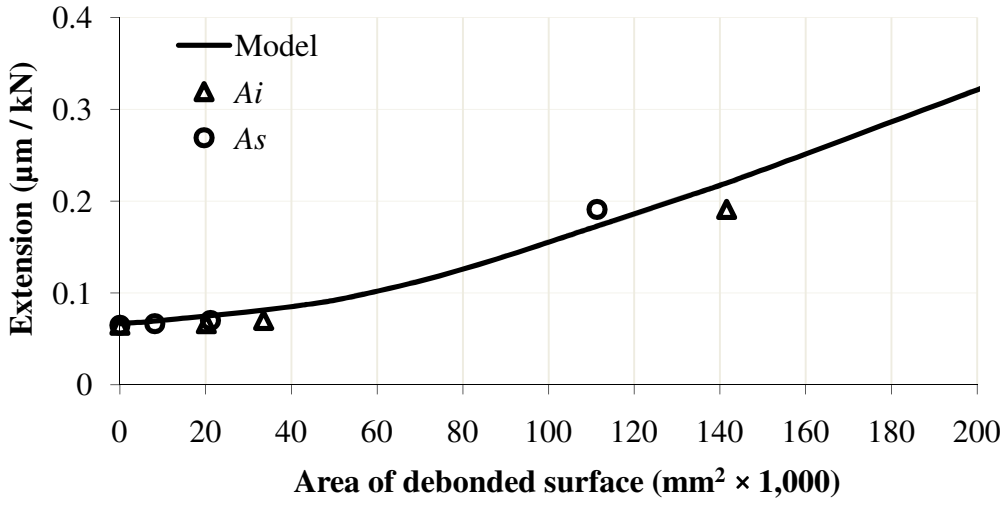

(b)

Figure 4.6: Predicted versus actual extension coefficient X as a function of debonding. (a) Supplier A. (b) Supplier B.

There is some subtlety in the presentation of S2L and S2R data (Figure 4.5). Recall from Chapter 3 that these two strain coefficients are primarily affected by debonding on the L or R end of the joint, respectively. For this reason, the S2L and S2R

data for each IJ are plotted separately. The values on the x-axis in Figure 4.5 are equal to two times the measured debonding on the appropriate half of the joint. For instance, a point (A_s = 20,000 mm^2, S2L = 0.30 με / kN) corresponds to 10,000 mm^2 of debonding on the L end of the joint. This is consistent with the use of these coefficients in the estimation algorithm of Chapter 3, which averages the debonding estimate from each coefficient to produce the estimate for the whole IJ.

Two phenomena are apparent in the results:

1.) The experimental data match the model more closely for insulated joints from Supplier B than Supplier A. Results for Supplier A show that deformation is less than predicted for all amounts of debonding (except the control specimen, which has no debonding).
2.) The experimental data match the model more closely when A_s, as opposed to A_i, is used as the measurement of debonding area.

Estimates of the debonded area using joint bar strain coefficients

Using the algorithm described in Chapter 3, it is possible to estimate the area of the debonded region for each test specimen using either joint bar strain coefficients (S1, S2L, and S2R) or the extension coefficient (X).

To estimate the debonded area from the joint bar strain coefficients:

1.) Compare S1 to some pre-determined value. If the measured S1 is below this cutoff value, then S1 should give a good estimate of debonding. Find the

measured S1 value on the y-axis of Figure 4.4a or 4.4b, and locate the corresponding point on the theoretical curve. The debonded area can be read from the x-axis of the figure at this location.

2.) If S1 is above the cutoff value, then S2L and S2R should be used. Find where the S2L and S2R values appear on the curve in Figure 4.5a or 4.5b, read the debonding values corresponding to these two points from the x-axis, and average them together to estimate the total debonded area.

For joints from Supplier A, the sensitivity analysis presented in Chapter 3 suggests that S1 should be used if it is less than 0.53 με / kN. A similar analysis of the finite element predictions for the slightly different joint bar shape used by Supplier B suggests a cutoff value for S1 of 0.51 με / kN. While the latter value seems to work well for Supplier B, 0.53 με / kN appears to be too high for Supplier A. S1 does not exceed 0.53 με / kN even in IJ's with large amounts of debonding. Based on the test data, a better cutoff value would be 0.50 με / kN for both types of IJ's.

The algorithm was modified in this manner and the estimated debonded area compared to both A_s and A_i (Table 4.2). The estimates are more accurate for IJ's from Supplier B because the finite element analysis predicted the deformation better for these specimens. Also note that the estimated debonding in most cases is closer to A_s than A_i.

Table 4.2: Estimated and actual debonded areas.

Specimen	A_i, $mm^2 \times 1{,}000$	A_s, $mm^2 \times 1{,}000$	Estimated from joint bar strains, $mm^2 \times 1{,}000$	Estimated from extension, $mm^2 \times 1{,}000$
CA1	0	0	0	7
CB1	0	0	0	0
TA1	100	59	23	52
TA2	134	80	60	62
TA3	180	161	115	101
TB1	34	21	15	12
TB2	20	8	21	0
TB3	142	111	129	125

Estimates of the debonded area using the rail gap extension coefficient

To estimate the debonded area from the rail gap extension coefficient X, locate the point on the curve in Figure 4.6a or 4.6b that matches the measured value of X, and read the debonded area from the x-axis. The results are included in Table 4.2.

Revised debonding estimates to account for bias

As noted previously, the debonding estimation algorithm appears to produce better results for IJ's from Supplier B than Supplier A. It would be preferable to analyze each population separately in order to quantify this difference, but there were too few samples of each. Instead, the analysis pooled all eight specimens together.

On the whole, the algorithm tends to produce estimates of the debonded area that are too low. A revised estimation algorithm that can account for this bias statistically will

both produce a more accurate result. Additionally, by removing the non-random component of the residuals, it will simplify error analysis.

Note that, if a statistical correction can be applied, the algorithm's original estimates need not match the actual debonded area, only correlate with it in a predictable manner. Figure 4.7 shows the correlation between the algorithm's estimates and the measured debonded area. Linear estimates of the correlation are given by dotted and dashed lines for A_i and A_s respectively. The slopes of these lines (ranging from 1.14 to 1.53) can be used to correct for systematic bias in the estimation algorithms. The revised debonding estimate is calculated by multiplying the original debonding estimate by the appropriate slope. For instance, for specimen TA1, the original estimate of the debonded area based on the rail gap extension coefficient was 52,000 mm^2. To estimate A_s, the revised algorithm multiplies this estimate by 1.18 to arrive at a new estimate of 61,000 mm^2. The revised estimates for each control and test specimen are shown in Table 4.3.

Table 4.3: Revised estimates of debonded area, accounting for bias.

Specimen	A_i from joint bar strains, mm^2 × 1,000	A_i from rail gap extension, mm^2 × 1,000	A_s from joint bar strains, mm^2 × 1,000	A_s from rail gap extension, mm^2 × 1,000
CA1	0	10	0	8
CB1	0	0	0	0
TA1	33	79	26	61
TA2	88	94	69	73
TA3	166	154	131	119
TB1	21	19	17	15
TB2	31	0	25	0
TB3	187	192	147	148

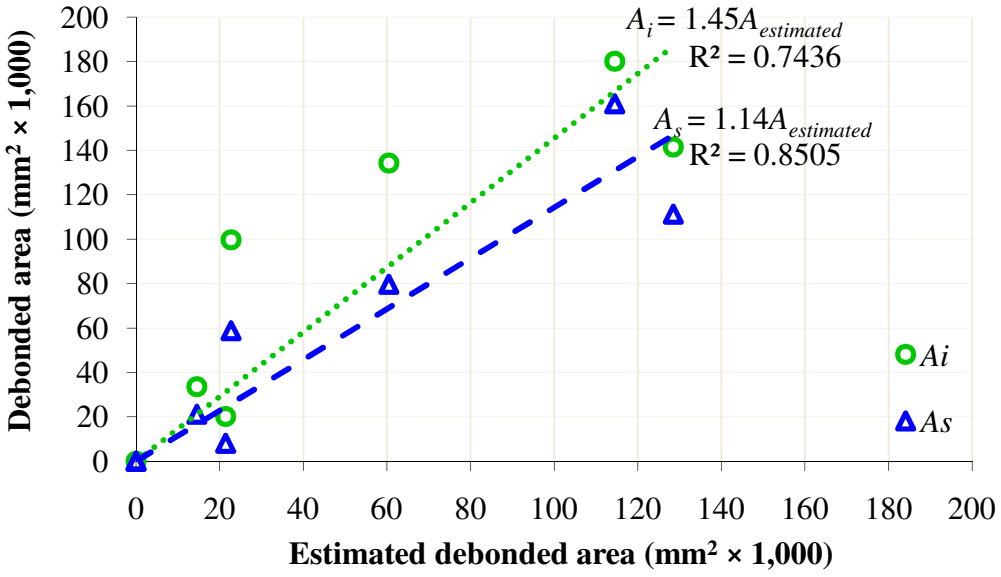

(a)

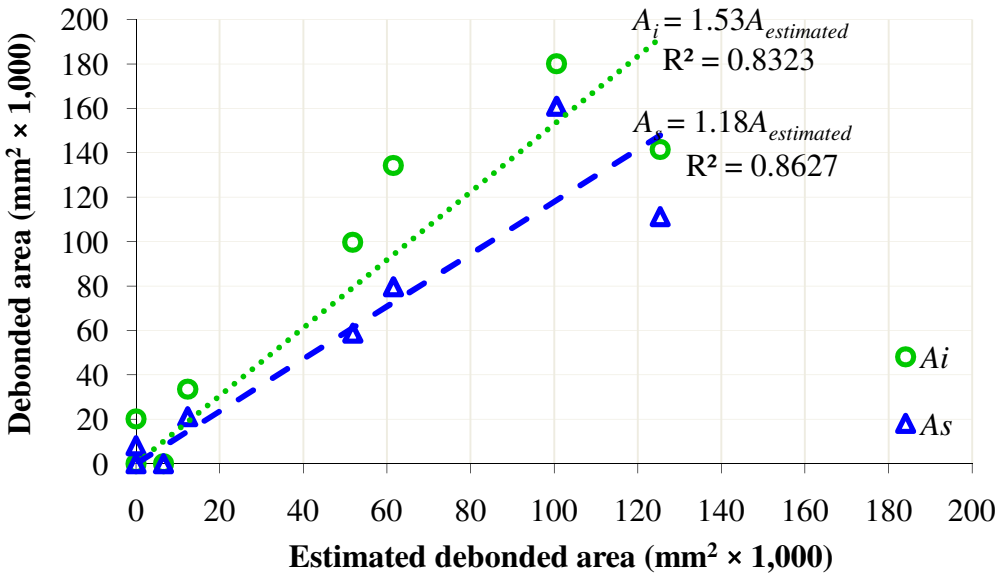

(b)

Figure 4.7: Correlation between estimated and actual debonding using (a) joint bar strains and (b) rail gap extension.

4.6 Error analysis

Confidence intervals

To produce a reliable confidence interval, the errors produced by the estimation algorithm must be random and independent. This was not the case for the original debonding estimates, which were routinely lower than the observed values. Revising the estimates to account for this bias mitigates the problem: when plotted, the residuals from the revised algorithm appeared to be randomly distributed.

Another assumption required to produce a confidence interval is that the residuals must be normally distributed. Strictly speaking this assumption is false. The algorithm never produces negative estimates of the debonding, so the actual error distribution will be asymmetrical. This technicality is believed to be relatively inconsequential and was ignored.

Assuming the errors produced by the revised estimation algorithm are random, independent, and normally distributed, confidence intervals can be calculated using Student's t-distribution and the standard deviation of the residuals (Table 4.4). Standard deviation in this case is calculated from the sum of squares, and degrees of freedom, of the residuals.

Table 4.4: 80% confidence intervals for various estimates of debonded area.

	Using joint bar strains	Using rail gap extension
A_i	± 63,000 mm^2	± 45,000 mm^2
A_s	± 40,000 mm^2	± 34,000 mm^2

There are 5 degrees of freedom of the residuals when joint bar strains are used and 6 when rail gap extension is used:

- 8 independent estimates are available, from the 8 control and test specimens.
- 1 model parameter (the stiffness of the epoxy layer) was chosen based on the test results of the control specimens, removing 1 degree of freedom from the error estimate.
- With joint bar strains, the algorithm uses a "cutoff value" of S1 to decide how to proceed. In Chapter 3, this value was chosen based on computer modeling, but in this chapter the value was revised based on the experimental data. This parameter therefore consumes one degree of freedom when joint bar strains are used for the estimation.
- The correlation between the original debonding estimate and the actual debonded area (Figure 4.7) also consumes one degree of freedom.

Effectiveness

The confidence intervals shown above are large enough that it is worth considering whether the estimates produced by the revised algorithm actually offer any insight into the state of the epoxy bond. One way to test this is to compare the accuracy of estimates produced by the algorithm to the accuracy of guesses made without knowledge of any strain or extension coefficients.

The mean values of A_i and A_s for the eight IJ specimens were 76,000 and 55,000 mm^2, respectively, and the standard deviations were 71,000 and 59,000 mm^2. Someone

who knew the mean values but had no knowledge about each joint's condition would guess that A_i and A_s are 76,000 and 55,000 mm^2 in each case. This uninformed guesser would have to allow intervals of ± 101,000 and ± 84,000 mm^2 in order to achieve 80% confidence. Note that these intervals are much wider than the ranges that were achieved using the revised estimation algorithm (Table 4.4). Therefore, the deformation measurements do in fact convey some information about the state of the epoxy bond.

On the other hand, Chapter 3 showed that careful visual inspection allows A_i and A_s to be estimated with 80% confidence to within ± 19,000 and 12,000 mm^2, respectively, which is considerably more accurate than the ± 34,000 to 63,000 mm^2 ranges achieved by the algorithm. While an automated measurement system has some operational advantages over visual inspection, the algorithm for estimating debonding from automated measurements was not able to achieve as much accuracy.

4.7 Discussion

Confidence intervals were calculated in section 4.6 using pooled results, because there were not enough data to analyze the different joint types separately. However, as noted in section 4.5, the experimental results matched the model more closely for IJ's produced by Supplier B than for those from Supplier A.

There are two possible explanations for why the results for Supplier A are less accurate: a weakness in the computer model, or problems with the measurements of the actual debonded area.

Chapter 2 noted that, even after an IJ has been disassembled, measurements of the debonded region are somewhat subjective, especially for IJ's from Supplier A. It is therefore possible that at least some of the discrepancy between model results and experimental results comes from misinterpreting the appearance of the disassembled IJ's.

It is likely, however, that the majority of the error lies with the computer model's deformation predictions rather than the debonding measurements. The computer model predicted that any IJ with more than 50,000 mm^2 of debonded area should have S1 values of at least 0.539 με / kN. Test specimens TA2 and TA3, with A_s measurements of 80,000 and 161,000 mm^2, had S1 values of 0.515 and 0.530 με / kN. Even if the measurements of debonding were imperfect, it is unlikely that these two specimens each had less than 50,000 mm^2 of debonding. Therefore, at least in this case, the model produced deformation estimates that were too high.

One possible reason for this discrepancy is the effect of friction in the debonded region. The computer model assumed a frictionless interface between the metal and the debonded epoxy, allowing no transfer of shear stress between the two. Any friction that does develop will act to reduce the effects of debonding, with the result that the estimation algorithm will underestimate the debonded area. Given that suppliers use different materials and assembly methods, it is possible that the debonded areas generate more friction in IJ's from Supplier A.

It should be stressed that for both suppliers the computer model correctly predicted the qualitative features and the approximate scale of the numerical relationship between debonding and deformation. The approach outlined in Chapter 3 seems to be

sound, and should only need further refinement to become useful. Such refinement would not necessarily require a more accurate computer model. Instead, more experiments of the type described in this chapter could be conducted to develop empirical versions of the curves shown in Figures 4.4 - 4.6. With more accurate curves, the algorithm described in Chapter 3 should be able to produce results that are considerably better than reflected in Table 4.3.

4.8 Conclusions

Chapter 3 described an algorithm whereby strain and extension measurements can be used to estimate the size of the debonded area. That algorithm relied on a finite element analysis of the effects of debonding on IJ deformation.

The laboratory tests described in this chapter were used to calibrate the finite element model and to test the accuracy of the debonding estimation algorithm. The results show that the algorithm, subject to the corrections described above, has the ability to estimate A_s to within about ± 40,000 $mm^{2,}$ and A_i to within ± 50,000 mm^2. Most error appears to be due to a mismatch between the experimental deformation measurements and the predictions of the finite element model for IJ's from Supplier A. Qualitatively, the relationships between deformation measurements and debonding seem to be sound. Empirical data from further experimentation of this sort could be used to refine, correct, or replace the finite element predictions, especially for Supplier A. This could increase the accuracy of the algorithm's debonding estimates.

CHAPTER 5: THE EFFECT OF PROGRESSIVE EPOXY DEBONDING ON THE RESPONSE OF INSULATED JOINTS TO STATIC VERTICAL LOADS

5.1 Introduction

Previous chapters focused on how to measure and quantify progressive epoxy debonding in a bonded insulated rail joint (IJ). It was proposed that knowledge about the state of the epoxy bond allows for improved scheduling of IJ maintenance or replacement. For this to occur, however, a second question must also be addressed: when should an IJ be replaced? The need to extract the maximum possible life from each installation must be balanced against the advantages of avoiding disruptive failure.

Even an IJ whose epoxy bond has failed completely is often able to perform its main structural and electrical functions for some time. However, joints with this degree of degradation are at increased risk of developing electrical problems (Davis et al. 2005) as well as potentially hazardous cracks. It is less clear what effect moderate amounts of progressive epoxy debonding have on a bonded joint. The epoxy serves an important structural function in reducing deformation under wheel loads. An IJ may have sufficient bond strength to prevent longitudinal slippage, but still suffer from degraded performance as a component in the track structure.

This chapter addresses one aspect of the performance of an insulated joint, namely, the stiffness of the joint in response to static vertical bending loads. Joint stiffness is an important factor in the rate at which the track substructure – especially the ballast and subgrade – degrades, and also affects the generation of dynamic loads. An IJ

that maintains its structural integrity but has lost stiffness will subject the ties, ballast, and subgrade below the joint to higher loads.

It has been noted that otherwise sound track often has local foundation problems near insulated joints (Davis et al. 2005). While the high-frequency impact loads at the discontinuity in the running service probably account for many of these problems, the increased track deflection due to low joint stiffness may also to be a contributing factor.

5.2 Literature review

Many different aspects of rail joint mechanics in general, and bonded joints in particular, have been studied. Some work focused specifically on the contact conditions that lead to plastic deformation and high impact loads at the rail gap (Chen and Kuang 2002, Wen et al. 2005, Steenbergen 2006). Because this type of damage results largely from high-frequency impact loads between the wheel and rail, these studies placed relatively little emphasis on the static stiffness of the track structure, instead emphasizing parameters such as the unsprung mass of the wheelset or the shape of the contact patch.

Another line of inquiry has taken the seminal work on rail joint mechanics performed by Jenkins et al. (1974) at British Rail and applied modern computing methods. These studies considered rail and substructure conditions in order to capture medium to low frequency aspects of the joint response. Several specifically addressed the dynamic effects of “dips” in the running surface resulting from plastic deformation of the rail head (Dukkipati and Dong 1999, Suzuki et al. 2005, Steenbergen 2006, Kabo et al. 2006). This work appears to be relevant for the problem considered here, because the

experiments described below show that epoxy debonding increases the effective dip at the joint under load. Some of these papers (Kabo et al. 2006) specifically focused on bonded insulated joints, but none considered the effects of debonding. There is also a lack of published experimental data to support many of these models, with the notable exception of work done by Suzuki et al. (2005) at the Railway Technical Research Institute.

Studies specifically related to the epoxy bond have to date focused largely on static load cases. For instance, a series of finite element models developed at the Virginia Polytechnic Institute and State University predicted the magnitude of stresses within the epoxy / insulator layer of a bonded IJ for several different joint and support configurations (Plaut et al. 2007, Himebaugh et al. 2007). These studies, along with experiments on epoxies, insulators, and the debonding process itself (Nicoli et al. 2007), offer some insight into why debonding occurs. However, these studies addressed only the causes of debonding, not its effect on IJ performance.

There are fewer published empirical studies of bonded IJ's than computational models. The Association of American Railroads studied various IJ designs in service at several locations on the North American rail network and at the Transportation Technology Center in Pueblo, CO, USA, publishing some data on load environment and service life (e.g. Li et al. 2006, Akhtar and Davis 2006, Davis et al. 2007). These field studies do not include any detailed investigation of IJ mechanics or how they might be influenced by debonding.

Of particular relevance to the current investigation is research by Cox and Kerr at the University of Delaware in the early 1990's (Cox 1993, Kerr and Cox 1999). They developed two simple, analytical models for describing the structural function of a rail joint, showed how to solve the corresponding differential equations for joints supported on an elastic foundation, and applied the models to the results of some simple laboratory tests of a single bonded IJ.

Cox and Kerr's tests were similar to those described in this chapter, but the larger number and greater diversity of test specimens used in my tests revealed some previously undetected aspects of IJ response. Additionally, the new tests allow the effect of debonding to be quantified and incorporated into one of the simple analytical models.

5.3 Test procedure

Specimens tested

The specimens used in the testing and the semantics of the specimen names are described in Chapter 3. One additional specimen that was not discussed in previous chapters, named TB4, was included in the vertical tests. This specimen differed from the others in that its epoxy bond had failed completely, leaving it held together only by its bolts. It provides a useful worst-case limit on the effects of epoxy debonding on joint stiffness.

Longitudinal tests

The longitudinal load tests described in Chapter 5 were conducted on the same set of test specimens before the vertical tests described in this chapter. It is possible that such loadings might have affected the specimens' response, and that different results might have been obtained had the order of testing been reversed. However, the load levels used in the longitudinal testing were well below those routinely experienced by an in-track IJ. They are therefore unlikely to have affected the vertical response of the test specimens, and any effect on the control specimens would make their behavior more, not less, representative of an in-track IJ.

Vertical loading

A specially constructed test frame was built from reusable steel W- and C-section members. A 530 kN hydraulic actuator was suspended from the frame. Test specimens were placed below the actuator, a load cell was placed between the specimen and the actuator, and the actuator piston was extended downward to apply a force to the top of the center of the joint (Figure 5.1). A simple electric pump was used to operate the actuator, with a single hand-operated valve giving a small degree of control over the loading rate. The effective loading rate was between 5 and 50 kN / s in most cases. Repeated tests on the same samples showed that the rate of loading had no measurable effect on the deformation results; therefore, except for any possible long-term creep effects, this can be considered quasi-static loading.

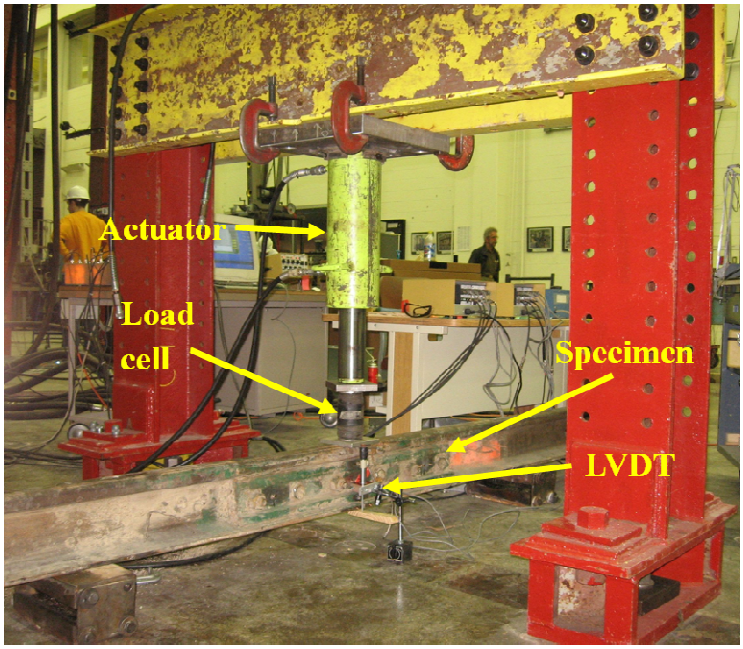

Figure 5.1: Vertical testing frame.

The specimen was supported vertically on rollers placed on the laboratory's "strong floor", 914 mm in each direction from the joint center. Loads of up to 250 kN were applied and released, with multiple cycles per specimen. These support conditions and load levels matched those used by Cox and Kerr (Cox 1993, Kerr and Cox 1999).

Two types of measurements were taken during the tests. A linear variable differential transformer (LVDT) was used to measure the displacement of the bottom of the rail relative to the floor at the center of the joint. For several specimens, strain gauges were also installed in the longitudinal direction along the sides of the rail head flush with the rail gap, in order to measure compressive stresses in the rail head and endpost.

Destructive disassembly of the test specimens

After load tests were complete, each test specimen was disassembled and inspected, and the debonded region was measured according to both Inclusive and Strict criteria, as described in Chapter 2.

5.4 Characterizing deflection behavior

Deflection at joint center

Displacement data from the LVDT at the center of the joint versus load magnitude for each control and test specimen were plotted (e.g. Figure 5.2). This revealed several features of the relationship between load and displacement:

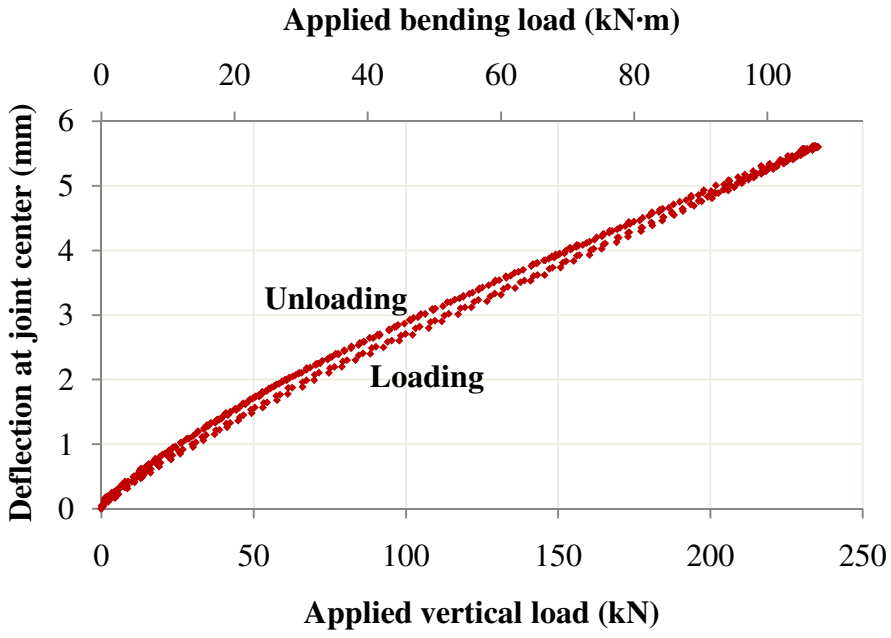

Figure 5.2: Deflection at center of joint bar, specimen CB1.

- For most samples, the marginal increase in deflection per unit load was higher at low load levels than at high load levels.
- There was some hysteresis. Deflections were higher during unloading than at the same applied force during loading.
- When the joint was completely unloaded, deflection returned to zero. No measurable plastic deformation occurred.

The fact that the unloading curve differs somewhat from the loading curve would be relevant in a dynamic analysis, and it suggests that existing linear elastic models of IJ deflection (e.g. Cox 1993, Kerr and Cox 1999, Kabo et al. 2006, Plaut et al. 2007, Himebaugh et al. 2007) do not capture the complicated behavior of the epoxy / insulator layer. Nonetheless, the primary purpose of these experiments was to determine how much an IJ will deflect under static loads. The amount of deflection is determined primarily by the loading curve. Therefore, this chapter will consider only the behavior of the joint under increasing vertical loads.

In most cases, the deflection versus load curve had a pronounced bilinear shape, with straight lines at low and high load levels connected with a curve of varying radius. In every case, the curve appeared straight below 35 kN and above 133 kN of applied load. (In most cases the straight portions of the curve extended well beyond these limits, but in no case were these regions curved.) Accordingly, for each specimen a straight line was fit to the data in each of regions using a least-squares curve fit (Figure 5.3). The slope of each line (called d_1 for low load values and d_2 for high load values), as well as the point of intersection (P_i, y_i), were used to characterize the deflection data for each specimen (Table 5.1).

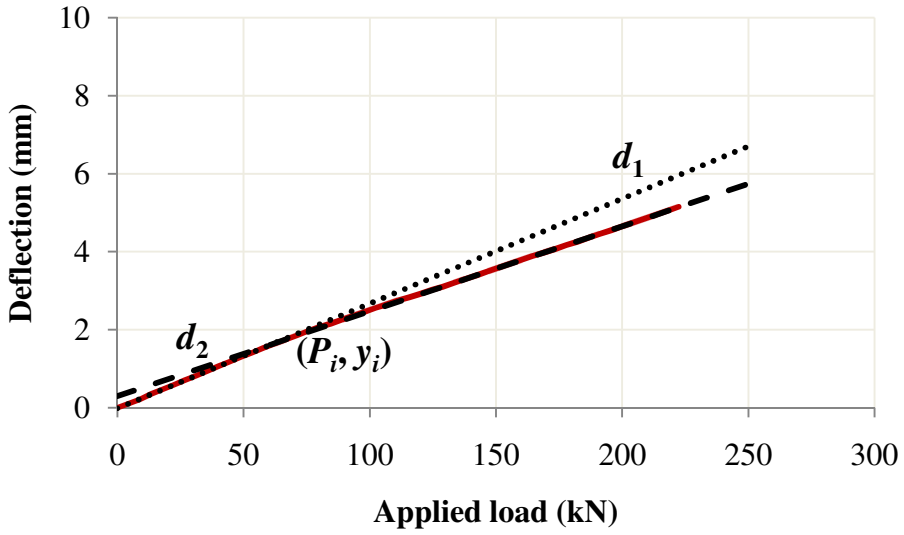

(a)

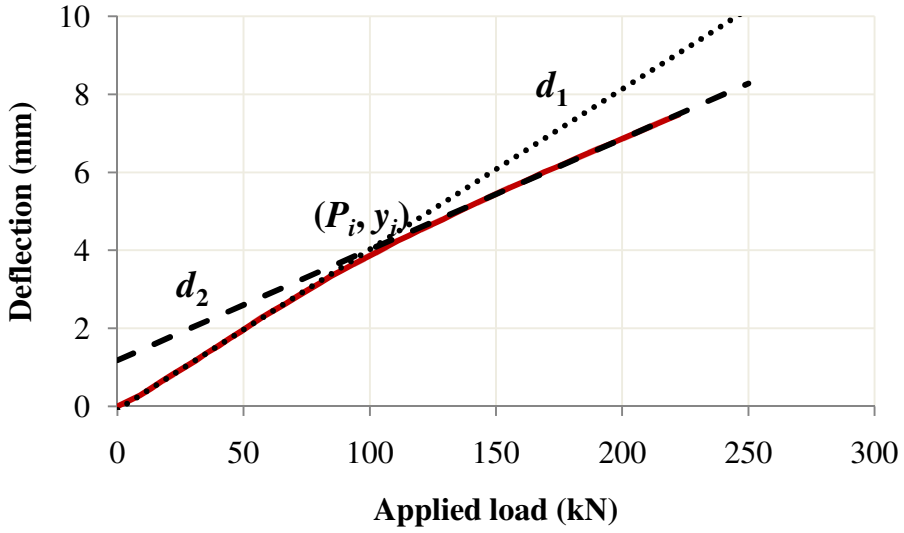

(b)

Figure 5.3: Fitting a bilinear model to the deflection data.
(a) Control joint CB1. (b) Test joint TA2.

Table 5.1: Vertical deflection at center of test specimens using the bilinear model.

Specimen	d_1 (mm / kN)	d_2 (mm / kN)	P_i (kN)	y_i (mm)
CA1	0.028	0.026	87	2.4
TA1	0.038	0.031	91	3.4
TA2	0.041	0.028	100	4.0
TA3	0.053	0.028	77	4.0
CB1	0.027	0.022	62	1.6
TB1	0.032	0.024	120	5.2
TB2	0.028	0.023	48	3.8
TB3	0.056	0.028	71	1.3
TB4	0.079	0.036	67	3.9

Applying Cox's rotational spring model to 3-point bending test results

Cox and Kerr developed two analytical models for rail joints subjected to static vertical loads. The more detailed "composite beam" model, which can be used to predict stresses and deflections in the joint bar, uses beams to represent the joint bars and the rails, with their interaction modeled as a distributed vertical spring (Cox 1993, Kerr and Cox 1999). The simpler "rotational spring" model, described only in Cox's unpublished M.S. thesis (1993), considers the entire joint to be a rotational spring holding the two sections of rail together. This model can be applied equally well to bolted or bonded joints. It has the advantage of characterizing joint stiffness as a single value between zero, where the rails are hinged and free to rotate relative to one another, and infinity, where the joint allows no rotation and behaves as a continuous beam. In some respects, this is a distillation of the metric of "joint efficiency" that was applied in the 1920's and 1930's by the American Railway Engineering Association's Special Committee on Stresses in Railroad Track (AREA 1980). "Joint efficiency" refers to the ratio of the bending moment carried in a rail joint under a given wheel load to the bending moment carried in continuous track

under the same conditions. A smaller spring stiffness in the rotational spring model will result in greater relative rotation, higher deflection, higher supporting loads on the crossties nearest the joint, lower bending moment in the joint, and lower joint efficiency. A spring stiffness of zero corresponds to a joint efficiency of zero, while infinite spring stiffness gives a joint efficiency of one.

The advantage of the rotational spring model is that it characterizes the joint with a single numerical value – namely, the spring stiffness. This parameter encompasses all the various interactions between rail and joint bar but is independent of support factors such as track modulus. The spring stiffness can be calculated directly from laboratory tests, and the results applied to any suitable beam-based track model model (such as the common "linear beam on elastic foundation" model) to predict behavior in the field.

A disadvantage of the rotation spring model, compared to the composite beam model (Kerr and Cox 1999), is that the distribution of bending moment between rails and joint bars within the region of overlap is not considered. This adversely affects the accuracy of the predicted deformations within the joint bar limits. However, as the composite beam model offers no simple way to account for debonding, this chapter uses the rotational spring model only.

The rotational spring model says that the bending moment in a rail joint is given by

$$M = s\Delta(y')$$

where $\Delta(y')$ is the relative difference in slope between the two rail ends. The governing differential equation is the beam bending equation,

$$EI_r y^{IV}(x) = u(x)$$

where E is the elastic modulus of the rail steel, I_r is the moment of inertia of the rail, y is the (positive downward) deflection of the rail, and u is the (positive downward) distributed load applied to the rail. To solve for general loading conditions, this equation is applied separately to each rail segment and continuity constraints are imposed to force the displacement y and the bending moment $EI_r y''$ to be equal on both sides of the joint. For symmetrical cases, including 3-point bending or a joint in track with a single wheel load directly over the joint, the equation can be solved for only one of the two rail sections.

Cox (1993) showed how to calculate the spring stiffness from the deflection versus load curve for the 3-point bending test with the load centered over the joint. In this case, $u(x) = 0$ and the four constraints needed to solve the governing differential equation are:

$y''(0) = (2sy'(0))/(EI_r)$	(spring reaction at joint)
$y'''(0) = P/(2EI_r)$	(load applied to joint center, ½ on each side)
$y(L/2) = 0$	(vertical support)
$y''(L/2) = 0$	(rotation unconstrained at vertical support)

where P = the applied load, L = the distance between supports, E = 207 GPa is the modulus of elasticity of the rail steel and $I_r = 39.2 \times 10^6$ mm^4 is the moment of inertia of RE136 rail (AREMA 2000b). Cox gave a solution for these conditions that can be used to calculate s from the ratio y/P.

Because my experimental measurements showed the relationship between y and P to be bilinear rather than linear, applying the model requires three parameters in place of the single spring stiffness s: one to describe stiffness at low loads, another to describe stiffness at high loads, and a third to identify the transition point between the two behaviors. As a first attempt, two spring stiffness values s_1 and s_2 are used to describe the stiffness of the joint at low and high loads, and a "critical rotation" r_c marks the transition between the two behaviors. The model for the rotational spring becomes

$$M = \begin{cases} s_1 \Delta(y'), & \Delta(y') \le r_c \\ s_1 r_c + s_2(\Delta(y') - r_c), & \Delta(y') > r_c \end{cases}$$

For the symmetrical case of 3-point bending, the relative rotation of the rail ends is $\Delta y' = 2y'(0)$. Therefore r_c is equal in magnitude to the value of $2y'(0)$, calculated using spring stiffness s_1, when the applied load is equal to P_i.

In order to understand the mechanics of the joints' response, it is helpful to characterize that response using independent parameters. There were strong correlations in the experimental data between the three parameters s_1, s_2, and r_c. Accordingly, the spring equation was rewritten using two new parameters, s_b (= s_1) and s_h (= $s_2 - s_1$):

$$M = \begin{cases} s_b \Delta(y'), & \Delta(y') \le r_c \\ s_b \Delta(y') + s_h(\Delta(y') - r_c), & \Delta(y') > r_c \end{cases}$$

s_b and s_h appeared to be independent of each other (Figure 5.4a), but r_c still correlated strongly with s_b. On other hand, the bending moment at which the transition occurs, $M_c = s_b r_c$, did appear to be independent of both s_b and s_h. (Figures 5.4b and 5.4c). This suggests that M_c is in fact a more fundamental characteristic of the joint, with r_c derived from it using the relationship $r_c = M_c / s_b$. M_c can be determined in the 3-point

bending test by noting that the moment at the center of the joint is $M = PL/4$; therefore, $M_c = P_iL/4$. The final equation for the bilinear spring stiffness model is:

$$M = \begin{cases} s_b\Delta(y'), & \Delta(y') \le M_c/s_b \\ s_b\Delta(y') + s_h(\Delta(y') - M_c/s_b), & \Delta(y') > M_c/s_b \end{cases}$$

A joint in track will have a deflection and a bending moment that varies depending on support conditions, but s_b, s_h, and M_c (Table 5.2) are assumed to be characteristics of the joint that are independent of support conditions.

Table 5.2: IJ parameters for rotational spring model.

Specimen	s_b (kN·m)	s_h (kN·m)	M_c (kN·m)
CA1	17,400	3,300	40
TA1	9,600	4,500	41
TA2	8,200	8,300	46
TA3	5,600	11,000	35
CB1	18,700	15,700	28
TB1	12,900	11,200	55
TB2	17,000	13,300	22
TB3	5,200	12,300	32
TB4	3,300	7,000	30

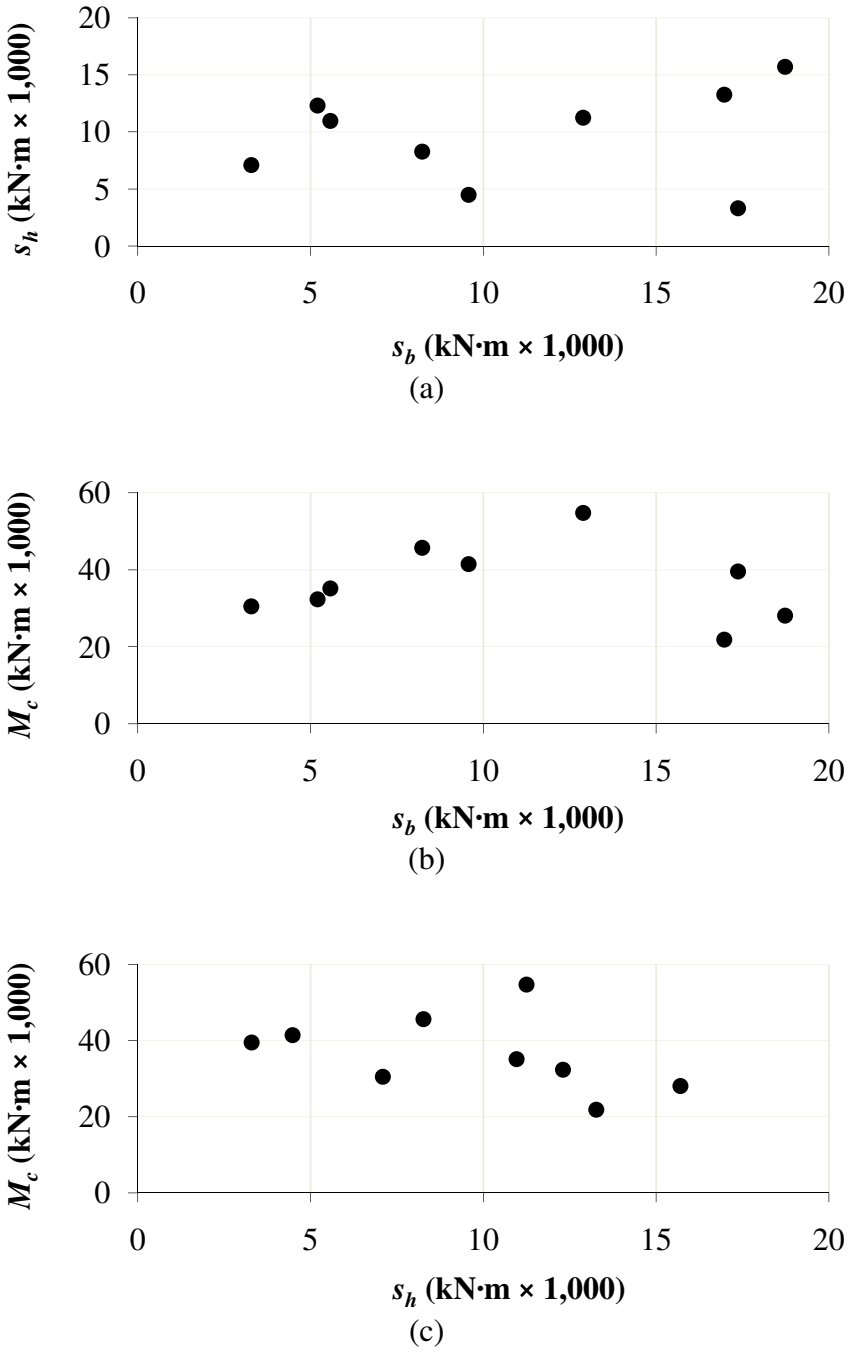

Figure 5.4: Independence of three IJ characteristics in the revised bilinear rotation spring model. (a) s_b versus s_h. (b) M_c versus s_b. (c) M_c versus s_h.

5.5 Mechanics of the bilinear deflection response

Previous studies of bonded insulated joints either ignored the large-scale vertical deflection of the rail base relative to the ground (Chen and Kuang 2002) or assumed that the elastic portion of the downward deflection is linear (Cox 1993, Kerr and Cox 1999, Dukkipati and Dong 1999, Kabo et al. 2006, Plaut et al. 2007, Himebaugh et al. 2007). The bilinear response therefore warrants further investigation.

One possible explanation for an increase in spring stiffness at higher load levels is that some new load-resisting mechanism engages only when the joint deformation reaches a certain magnitude. In the case of a bonded IJ, it is usually assumed that the entire bending load is transferred between the two rail sections via bending action in the joint bars (Kerr and Cox 1999, Himebaugh et al. 2007). But if bending moment could be transferred directly from one rail to the other through the endpost, then the joint bars would bend less and the relative rotation between rail ends would be smaller, resulting in higher spring stiffness. If such transfer happens only under large bending loads, it would explain the stiffening behavior.

To determine whether some bending moment might be transferred through the endpost, strain gauges were added to the rail heads of specimens CB1, TA1, TA3, TB1, and TB3. One 6.35 mm gauge was placed longitudinally on the vertical surface of each side (field and gauge) of one rail end, halfway down the head and flush with the rail / endpost interface (Figure 5.5). This location was chosen to be as far as possible from both the point of applied loading and the rail / joint-bar interface, so that strain should reflect only the longitudinal stress at the rail-head / endpost interface. The average of the two

strain readings can therefore be taken as indicative of the average longitudinal stress at that particular height on the rail head. Because the endpost is unlikely to transmit tensile stresses, no strain gauges were placed on the rail base.

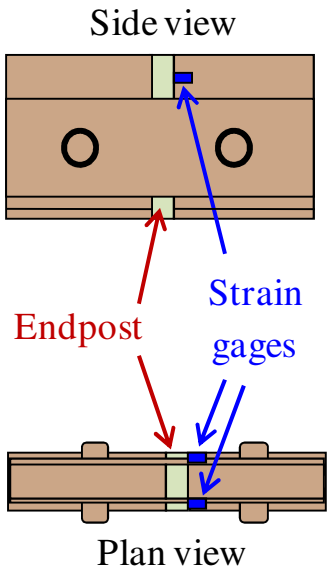

Figure 5.5: Location of strain gauges for measuring compression in rail head.

The results strongly suggest that the reason for the bilinear nature of static IJ deflection is due to forces transmitted through the endpost. It appears that in many cases some play exists between the rail end and the endpost. As the bending action of the joint brings the two rail heads closer together, full contact with the endpost develops and the endpost begins to absorb some of the system's bending moment. The load at which compression develops in the rail head correlates with the point at which the spring stiffness of the joint starts to increase, and the magnitude of compression correlates with the amount of stiffening as indicated by the parameter s_h. For example, specimen TB3

developed compression in the rail head at approximately P = 60 kN (Figure 5.6a), close to the previously described transition point of P_i = 72 kN (Table 5.1). The compressive strains are relatively large, in keeping with its large s_h value of 12,300 kN·m. By contrast, specimen TA1 has a low s_h value of 3,300 kN·m, indicating that relatively little stiffening occurs as load is increased. This is explained by noting that far less compression develops in the rail head at any load level (Figure 5.6b). For this specimen, rail-to-endpost stresses had little effect on deflection.

Thus it appears that the stiffness at low loads s_b is indicative of the resistance to deformation provided by bending action of the joint bar, while the stiffening factor s_h results from compressive forces in the two rail heads and endpost.

Deflection under combined vertical and longitudinal loadings

All the data in Table 5.1 were gathered using simple 3-point bending tests in a laboratory setting. Since the bilinear deflection response is due to contact pressures developing between the end of the rail head and the endpost, the results might change if longitudinal loads were simultaneously applied to the joint. In North America, IJ's are generally kept in a state of relatively high tension throughout most of the year (Li et al. 2006). Such tension might prevent the endpost from developing compressive stresses, resulting in a lower stiffening factor s_h or a higher transition point M_c between low-load and high-load behavior. The likely result would be higher deflections than predicted using the bilinear parameters derived from laboratory tests. Therefore, the assumption made in other studies, that the endpost does not transmit forces, may be a reasonable, conservative

approximation of actual behavior. Further testing would be needed to determine the effect of longitudinal forces on the development of endpost stresses and joint stiffness.

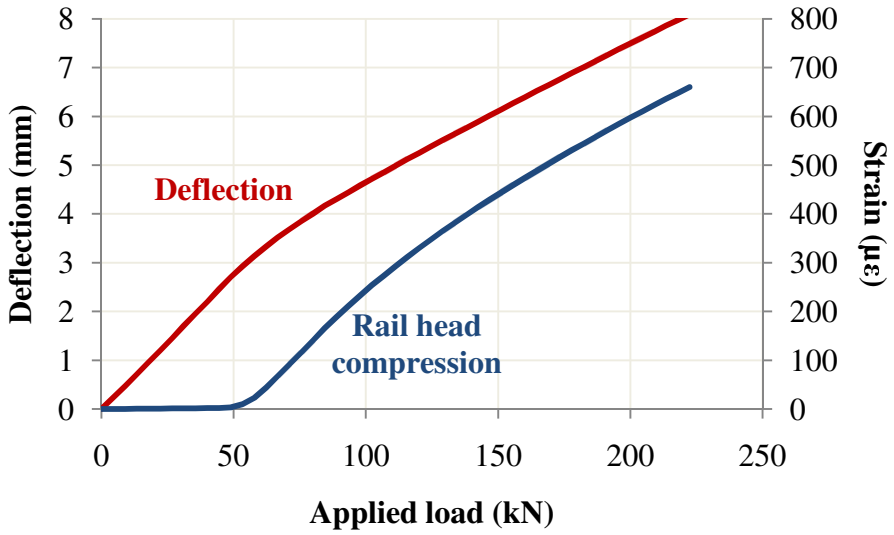

(a)

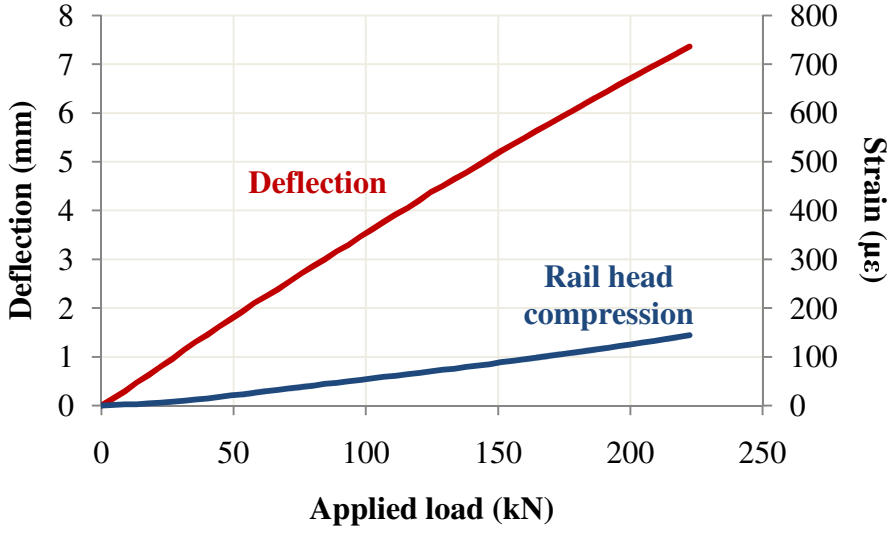

(b)

Figure 5.6: Relationship between compressive strain in the railhead and joint stiffening behavior. (a) Test specimen TB3. (b) Test specimen TA1.

5.6 Effect of progressive epoxy debonding on IJ stiffness

Cox (1993) showed that bonded insulated joints deflect less in a 3-point bending test than bolted joints, even when the bolted joint's bars have a higher moment of inertia than the bonded joint's. Since the epoxy bond increases stiffness, it seems likely that progressive epoxy debonding might lead to a decrease in IJ stiffness.

The nine specimens had varying amounts of epoxy debonding. The two control specimens had no debonding, six specimens were debonded over a portion of the rail / joint-bar interface, and one specimen has a complete failure of the epoxy bond. Destructive disassembly of specimen TB4 revealed that all four rail / joint-bar interfaces were covered with heavy rust, so the joint was assigned a debonded area (both the Inclusive area A_i and the Strict area A_s) equal to the total area of all four interfaces (322,000 mm^2). Note that "complete failure of the epoxy bond" as defined in Chapter 1 can occur even if two of the rail / joint-bar interfaces remain bonded. Because no other such specimens were tested, it remains unknown whether a joint with one or two intact bond surfaces performs differently from a joint with none.

All three parameters of IJ stiffness (s_b, s_h, and M_c) were plotted versus debonding (Figure 5.7). As might be expected, the only parameter that correlates with debonding is s_b, the stiffness that results from bending action in the joint bars. Debonding allows greater relative motion between rails and joint bars, so that more rail rotation is required to generate the same joint bar deformation and reactive moment.

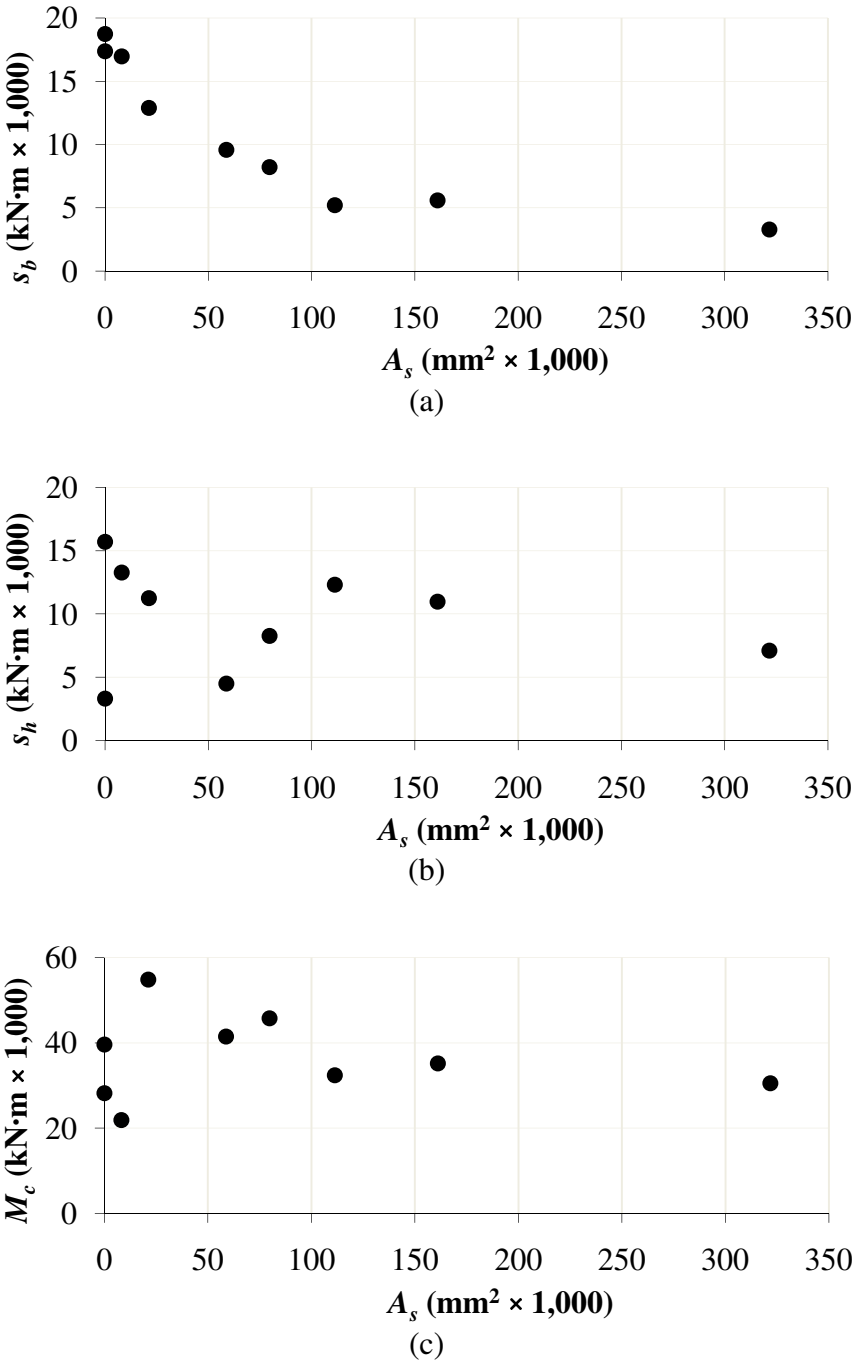

Figure 5.7: IJ characteristic parameters as a function of A_s. (a) Joint-bar-related bending stiffness s_b. (b) Rail-head-compression-related bending stiffness s_h. (c) Moment M_c at which rail head compression begins.

Even an IJ with no epoxy bond (such as test specimen TB4) develops bending moments in the joint bars. The epoxy bond simply adds additional stiffness to what

would otherwise be a bolted joint. The joint-bar-related stiffness s_b can be broken into two parts:

$$s_b = s_u + s_e$$

where s_u ("unbound" stiffness) is the stiffness the joint would have with no epoxy bond, and s_e is the increase in stiffness due to the epoxy. s_u, like s_h, should be independent of the state of the epoxy bond, while s_e will depend on the size of the debonded area. For this analysis, s_u was assumed to be identical for all of the control and test specimens, although in fact some variation would be expected, especially between joints from different suppliers. This constant value of s_u, 3,300 kN·m, is estimated from tests on specimen TB4: because this specimen had no epoxy bond, $s_e = 0$ and $s_u = s_b$. Every other specimen's s_e value is calculated by subtracting the fixed value s_u from the measured value s_b (Table 5.3).

Table 5.3: Stiffness s_e due to epoxy for each specimen.

Specimen	s_e (kN·m)
CA1	14,100
TA1	6,300
TA2	4,900
TA3	2,300
CB1	15,400
TB1	9,600
TB2	13,700
TB3	1,900
TB4	0

The relationship between the total debonded area of the joint and its epoxy-related stiffness s_e is nonlinear. Epoxy resists shearing displacements and separation between the rail and the joint bars. It is most effective at increasing stiffness when placed where such displacements tend to develop under bending loads. Epoxy located near the center of the joint thus makes a greater contribution to stiffness than epoxy located farther out from the joint center. The central region is also the first to experience progressive epoxy debonding, so small amounts of debonding have a disproportionate effect on s_e. More generally, the epoxy that works most effectively to resist bending seems to be the most likely to deteriorate, so that the effect of debonding on stiffness starts out large but tapers off as the useful epoxy debonds. This makes it appropriate to fit a model of exponential decay to the stiffness versus debonding curve (Figure 5.8):

$$s_e = C_1 e^{-C_2 A} + r$$

where A is the debonded area (A_i or A_s), C_1 and C_2 are constants developed through least-squares curve-fitting (Table 5.4), and r is a normally distributed random variable representing experimental error. C_1 is the increase in stiffness due to epoxy for a fully-bonded IJ over; C_2 quantifies the relative importance of debonding near the joint center versus debonding farther out on the joint bars.

Table 5.4: Parameters for model $s_e = C_1 e^{-C_2 A} + r$.

Debonding criteria	C_1 (kN·m)	C_2 (mm^{-2} × 10^{-3})
Inclusive	15,000	0.0102
Strict	14,700	0.0150

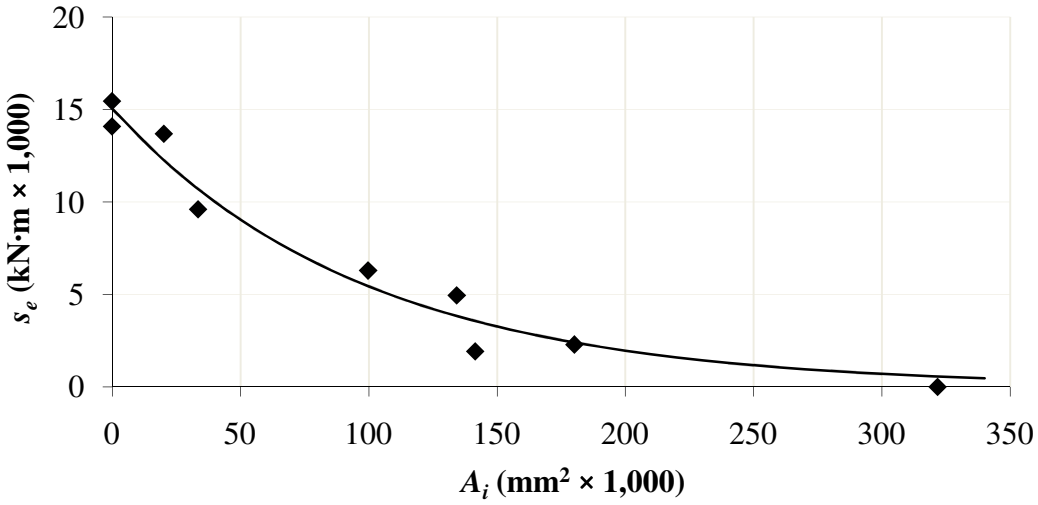

(a)

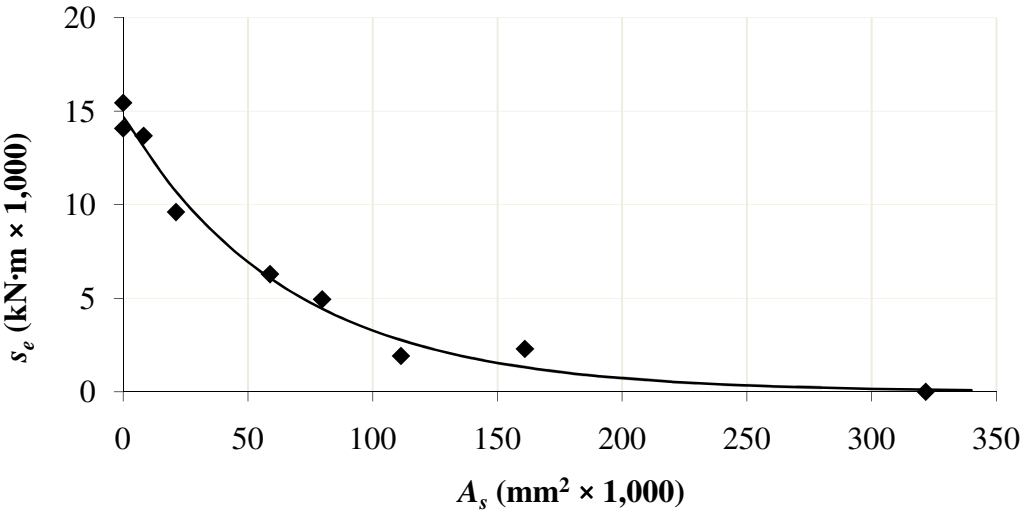

(b)

Figure 5.8: Correlation between s_e, the joint stiffness due to the epoxy, and debonding. (a) Inclusive debonded area A_i. (b) Strict debonded area A_s.

5.7 Confidence intervals

The differences between the values of s_e calculated from the data and the values predicted from the regression relation appear to be random and independent (Figure 5.9). It is

reasonable to assume that they are normally distributed, which allows confidence intervals to be constructed using Student's t-distribution. The sample standard deviation is calculated from the sum of squares of the residuals divided by the degrees of freedom. Of the nine original degrees of freedom from the nine data points, two are used to estimate the two regression coefficients C_1 and C_2. In addition, one degree of freedom is used to estimate the stiffness s_u of a joint with no epoxy bond, which is needed to calculate s_e. This leaves six degrees of freedom for the residuals.

Only one of the test specimens had complete epoxy failure. It is therefore not possible to calculate a confidence interval for the parameter s_u.

For higher loads, the stiffness s_h due to rail head compression must also be considered. As noted previously, s_h does not appear to correlate with epoxy debonding, and therefore must be estimated by a single average value. A confidence interval can be calculated using the t statistic, this time with 8 degrees of freedom. A similar approach gives a confidence interval for the critical bending moment M_c.

The confidence intervals for the joint stiffness parameters are summarized in Table 5.5. The wide range of possible values for s_h and M_c suggest that further study is needed to understand the factors that affect the development of compressive forces in the rail head.

Table 5.5: 80% confidence intervals for IJ stiffness parameters.

Parameter	Estimated value (kN·m)	Range (kN·m)
s_e based on A_i	$15{,}000e^{-0.0102Ai}$ (1)	± 1,800
s_e based on A_s	$14{,}700e^{-0.0150As}$ (1)	± 1,300
s_u	3,300	N/A
s_h	9,600	± 5,800
M_c	36.6	± 13.9

(1) A_i and A_s measured in mm^2 × 1,000

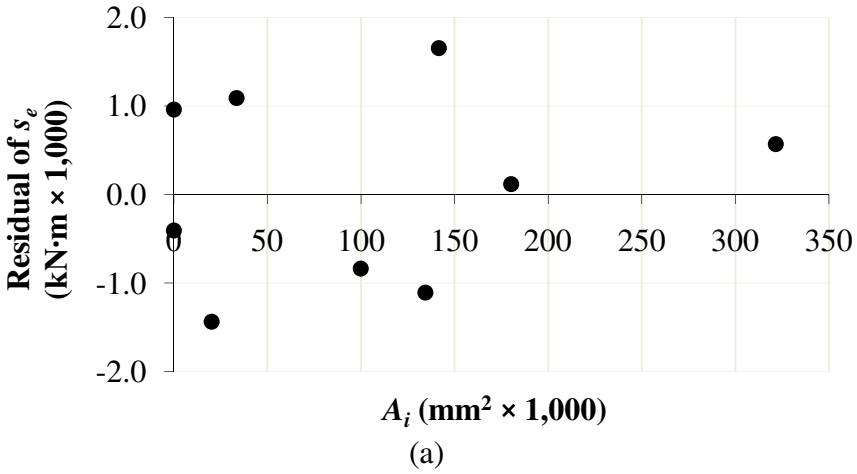

(a)

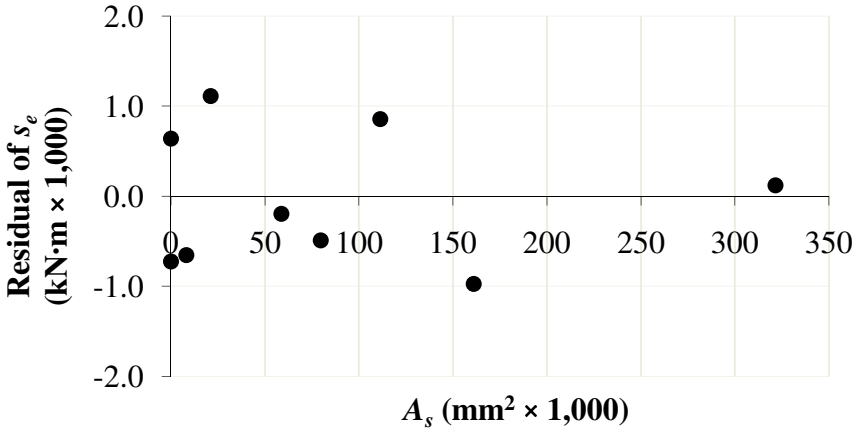

(b)

Figure 5.9: Error in exponential model for s_e. (a) Inclusive debonding. (b) Strict debonding.

5.8 Behavior in a Linear Beam On Elastic Foundation model

Method

Simple track analysis can be done using the Linear Beam On Elastic Foundation (BOEF) model, usually attributed to Winkler (1867) and widely used in various forms throughout the railroad engineering literature. In the BOEF model, the load applied to the track at any given location is directly proportional to the vertical displacement of the track at that point. Typically this analysis is done on a single rail at a time, rather than on the entire track structure. The AREA Special Committee on Stresses in Railroad Track applied this single-rail analysis to staggered rail joints (AREA 1980), implicitly assuming that the increased deflection at a joint in one rail had negligible effect on the opposite rail. The appropriateness of this approach might be questionable, especially for today's stiffer track and crossties. For insulated joints, however, it seems appropriate. IJ's generally appear almost directly opposite each other in the railroad track, so increased deflections are likely to occur under both rails at the same location. Therefore this analysis will use a single wheel load applied to an insulated joint on one rail.

Cox (1993) gives a general method for combining the rotational spring model of a joint with the BOEF track model, but a simpler model with a single static load centered over the rail joint is sufficient for illustrating many of the effects of debonding on IJ stiffness. In the simplified model, the rail extends infinitely in both directions, but due to symmetry only one half of the joint needs to be considered and a single differential equation with four constraints suffices. Let k be the track modulus (expressed in units of force per unit length per unit length, or, equivalently, force per unit area); the distributed

load along the half-infinite beam is $u = -ky$. The constraint equations are similar to those for the 3-point bending test:

$$y''(0) = (2sy'(0))/(EI_r) \quad \text{(rotational spring reaction at joint)}$$

$$y'''(0) = P/(2EI_r) \quad \text{(1/2 of load applied to each rail end)}$$

$$\lim_{x\to\infty} y = 0 \quad \text{(no rigid-body motion)}$$

$$\lim_{x\to\infty} y'' = 0 \quad \text{(no rigid-body rotation)}$$

where P represents a single vertical wheel load.

Two particular quantities of interest can be computed from the solution to these equations: the concentration of load on the crossties nearest to the joint, and the relative rotation between the two rails' running surfaces. Load concentration is of interest because of its possible effect on substructure damage, while rotation plays a role in the development of dynamic loads.

Because of the bilinear response of the test specimens, the rotational spring model must be adapted to account for the two different spring stiffness values. The approach used is as follows:

1. Given the track stiffness parameter k, and a spring stiffness s_b, calculate the maximum wheel load P_c that could be supported without exceeding the critical moment M_c.
2. If the actual wheel load is less than P_c, solve the equation with $s = s_b$.
3. If the actual wheel load is greater than P_c, first solve the problem using spring stiffness s_b. Then solve again using spring stiffness ($s_b + s_h$) and wheel load $P - P_c$.

Because the model is linear in all but spring stiffness, the two solutions may be added together to produce the overall solution.

Values of P_c for the experimental specimens and several different track stiffness (Table 5.6) show that a static wheel load of 159 kN, the maximum value commonly used for North American freight operations, will not greatly exceed P_c in most cases, even on relatively soft track. Therefore spring stiffening due to compressive stress in the rail head will have little influence on IJ response to static loads. However, dynamic loads of up to 220 kN, attributed to impact loads from out-of-round wheels, are not uncommon (Li et al. 2006). These load levels may exceed P_c on normal railroad track.

Table 5.6: Critical wheel loads for in-track IJ's.

	P_c (kN)	
Specimen	k = 10 MPa	k = 50 MPa
CA1	138	222
TA1	163	272
TA2	186	316
TA3	161	283
CB1	88	139
TB1	202	330
TB2	77	123
TB3	153	270
TB4	175	323

The bilinear deflection model is based on static loadings, and it is unknown whether it accurately characterizes deflection under impact loadings. Additionally, as noted above, the tensile forces commonly found in IJ's in track may increase M_c and P_c. For design purposes, these difficulties are reasonably avoided by conservatively assuming an infinite value of P_c and ignoring the possibility of stiffening. This is the

approach taken in the sections of this chapter that describe the effect of debonding on insulated joints in track. However, when performing experiments or measurements on IJ's, it may be necessary to consider the effect of compressive stresses in the rail head.

Effect of debonding on crosstie loads

The beam action of the rail distributes wheel loads across multiple crossties, helping to keep pressures at the rail / tie, tie / ballast, and ballast / subgrade interfaces within acceptable limits. A reduction in the bending stiffness of a rail impairs this distribution function, concentrating the loads on fewer ties. Any rail joint with a finite rotational stiffness therefore represents a potential for localized damage to the track substructure.

The BOEF model can be used to estimate the forces on the ties near the rail joint. This estimate will be limited in accuracy, because it smoothes out details that are important in analyzing such a local problem, but it nonetheless provides a simple and useful method for describing the potential effects of debonding on load concentration. Two cases will be investigated: a "supported" joint centered over the midline of a crosstie, and a "suspended" joint centered over the midline of a crib. In both cases, ties are assumed to be spaced t = 508 mm apart, center-to-center.

For the supported joint the maximum tie load occurs when the load is directly over the joint, so that the downward displacement y can be calculated from the symmetrical equations given previously. The tie under the joint experiences a load $P_{sup} = \int_{-t/2}^{t/2} kydx = 2k \int_{0}^{t/2} ydx$. Assuming that the wheel load does not exceed P_c, the

percentage of the wheel load that is transmitted to the support tie, given soft track support (k = 10 MPa), varies from 18.7% for unbroken rail with no joint to 25.5% for an IJ with complete epoxy failure (Figure 5.10). On stiff track (k = 50 MPa), the corresponding values are 27.4% for no joint and 38.8% for complete epoxy failure. A fully bonded joint increases the load on the support tie by 13% - 15% over a continuous rail; epoxy failure can increase that factor to 37% - 41%. With a moderate debonded area of 80,000 mm^2 (equal to about ¼ of the original total bond area) the increase in tie load is about 20% - 31%. This is for static loads only, and does not take into account the increased dynamic load factors often found at joints.

Calculations for a suspended joint are complicated by the fact that the maximum tie load may not always occur when the static wheel load is centered over the joint. For instance, when the joint has infinite stiffness, making it equivalent to an unbroken section of rail, the maximum load on the support tie will occur when the wheel is placed over the tie – a distance of $t/2$ away from the joint center. Because the load is no longer symmetrical, the more complicated equations given by Cox (1993) must be used. These show that, for joints with low stiffness (less than 14,000 kN·m when k = 10 MPa, less than 8,000 kN·m when k = 50 MPa), the maximum tie load will occur when the load is centered over the joint. For stiffer joints, the maximum tie load will occur when the load is located somewhere between the center of the joint and the midline of the support tie.

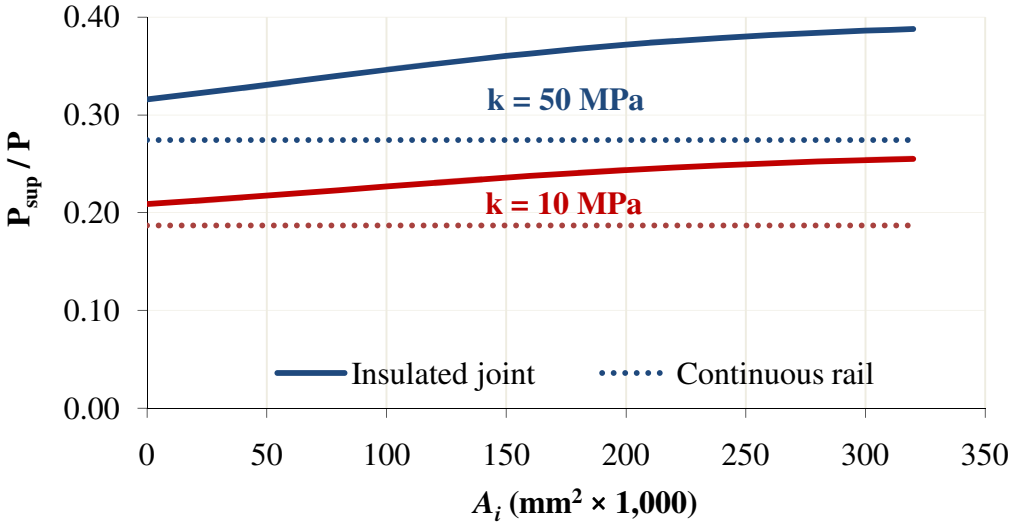

(a)

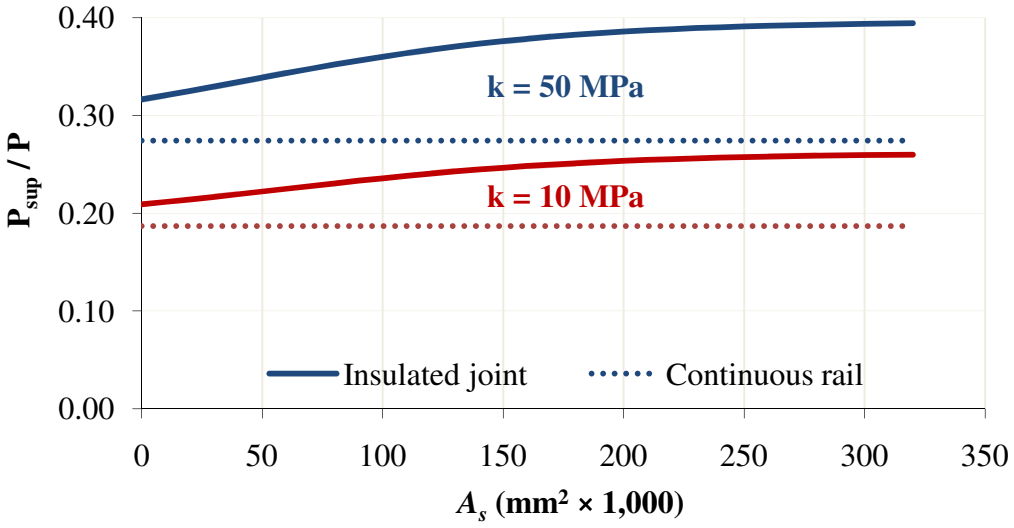

(b)

Figure 5.10: Fraction of single static wheel load carried on single crosstie for a supported joint and effect of debonding. (a) Inclusive debonding. (b) Strict debonding.

Using conventions similar to those used by Cox, the load is placed at a distance a to the right of the joint, and the displacement function y is broken into segments y_1, y_2, and y_3 representing the rail to the left of the joint, between the joint and the load, and to

the right of the load respectively. The load taken by a tie centered *t*/2 to the right of the joint is $P_{sus} = \int_0^t kydx = k\int_0^a y_2 dx + k\int_a^t y_3 dx$. For a given spring stiffness and track modulus, the point of load application that produces the maximum tie load can be calculated by differentiating this expression with respect to *a* and solving numerically for *a*. That value of *a* is then used to calculate the maximum P_{sus}.

The results show that the effect of debonding on tie loads near a suspended joint (Figure 5.11) is similar to a supported joint. The increase in load concentration between continuous rail and rail with a fully bonded joint is only about 7% in this case (compared to 15% for the supported joint), but debonding can increase that number to about 26%. A suspended joint with 80,000 mm^2 of debonding will cause load concentrations 13% - 14% higher than continuous rail. Again, these numbers represent the response to static loads only.

These results are useful for understanding the effects of debonding on substructure stresses. They should not necessarily be interpreted to conclude that supported joints experience higher tie loads than suspended joints. The generalized nature of the BOEF model and the absence of dynamic load factors prevent this analysis from answering such questions. What it shows instead is that, in each case, a moderate 80,000 mm^2 of debonding leads to an additional tie load of around 15% of the static wheel load compared to a joint with no debonding.

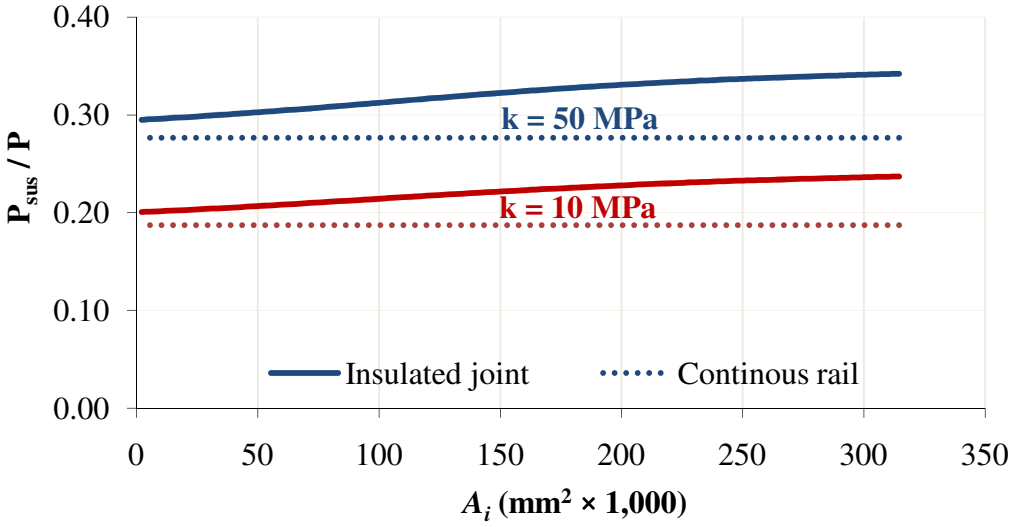

(a)

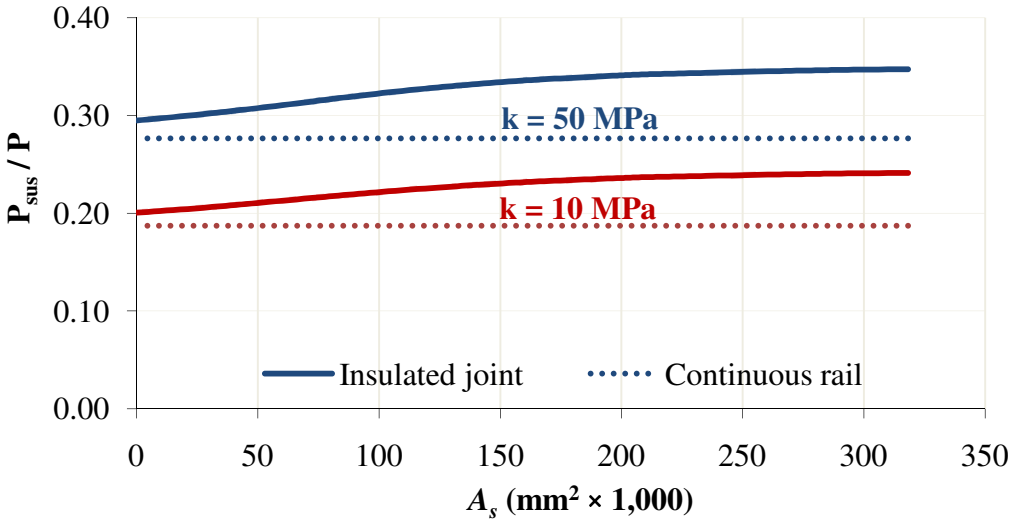

(b)

Figure 5.11: Fraction of single static wheel load carried on single crosstie for a suspended joint and effect of debonding. (a) Inclusive debonding. (b) Strict debonding.

Effect of debonding on joint angle

Jenkins et al. (1974) noted that, for a given track structure, the peak dynamic forces in a joint "are [to a close approximation] proportional to the product of the total joint angle

(2α) and the [train] speed", where "joint angle" refers to the sum of the angles of each rail end with the horizontal. This angle results partly from permanent deformation of the rail ends, and partly from the dynamic downward deflection of the joint under the wheel load. A lower joint stiffness results in a greater joint angle under load; thus, debonding has the potential to increase dynamic loads. A dynamic analysis is beyond the scope of this thesis; however, it is easy to estimate the joint angle using the rotational spring model: $2\alpha = \tan^{-1}(\Delta y') \approx \Delta y'$, where $\Delta y'$ is the change in slope from the left side of the joint to the right. This estimation suffers from the same limitations as the preceding section on crosstie loads: the dynamic behavior of a wheel at a joint depends on the precise geometry of the gap in the rail, which cannot be determined using the rotational spring and BOEF models. Nevertheless, the model shows that debonding has a strong affect on the dynamic portion of the joint angle (Figure 5.12). 100,000 mm^2 of debonding is generally enough to increase this portion of the joint angle by a factor of two; complete bond failure may cause it to triple.

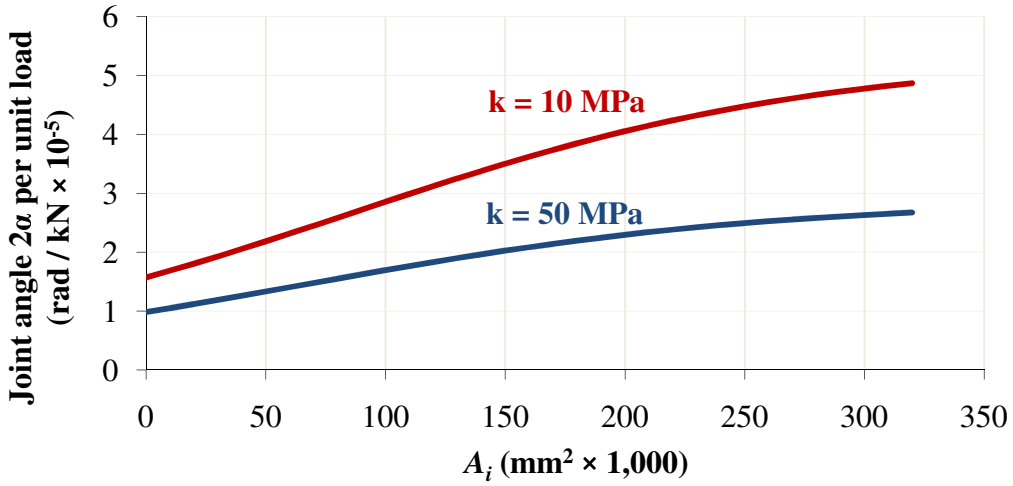

(a)

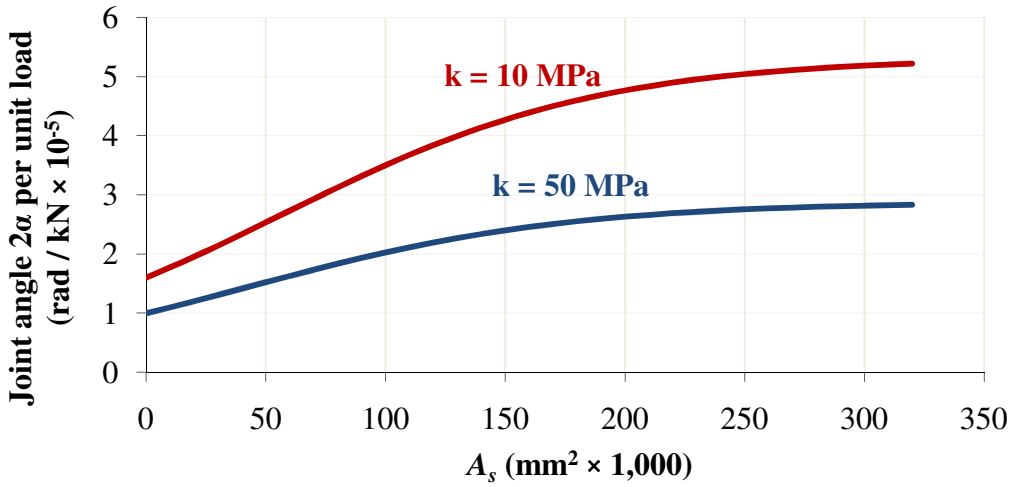

(b)

Figure 5.12: Joint angle as a function of debonding. (a) Inclusive debonding. (b) Strict debonding.

5.9 Conclusions

The bending stiffness of a bonded insulated joint is largely dependent on the soundness of the epoxy bond. Stiffness can be quantified using a simple model in which a rotational spring connects the two sections of rail. For a fully bonded IJ, the stiffness measured in this way was around 17,000 kN·m, while a joint with complete epoxy failure had a

stiffness of around 3,000 kN·m. The effectiveness of the epoxy in enhancing joint stiffness had a negative exponential relationship with the area of the debonded region, with modest amounts of debonding having a disproportionate influence on stiffness.

The rotational spring model for the joint combined with the BOEF model for the track suggested that a debonded area of 80,000 mm^2 (equal to approximately 25% of the original bonded area) could increase the static load on the nearest crosstie by 9 – 14% compared to a fully bonded joint, and could increase the dynamic portion of the joint angle 2α by a factor of 1.7 – 2.2. The accuracy of these models in predicting such localized behavior is limited, but the results strongly suggest that progressive debonding has the potential to damage the track substructure.

If sufficient bending moment develops in the joint, due to a combination of a high wheel load and soft track support, the rails may begin to transfer compressive bending forces directly from one rail head to the other through the endpost, in addition to the bending moment that is carried through the joint bars. This stiffens the joint and reduces deflections somewhat. The bending moment at which this phenomenon begins and the amount of stiffening that occurs appeared to be independent of the debonded area. This phenomenon was clearly visible in laboratory bending tests, but its applicability to in-track joints may depend on the dynamic response of the joint and the amount of longitudinal force in the rails.

CHAPTER 6: GENERAL FINDINGS AND FUTURE RESEARCH OPPORTUNITIES

The previous chapters describe experiments designed to answer particular questions about progressive epoxy debonding and its effects. Those experiments also produced data that may be relevant to other important questions about the deterioration of bonded insulated rail joints. In the first section of this chapter, some findings tangential to the central conclusions of this thesis are described.

The second part of this chapter places the previous chapters in a larger context by describing additional experiments that would further advance understanding of progressive epoxy debonding and efficient maintenance of deteriorating IJ's.

Finally, the chapter concludes with a general suggestion on how to approach IJ design and maintenance.

6.1 General findings

Interpreting debonding measurements

Visual inspections of disassembled joints (Chapter 2) showed that it can be difficult to determine the exact boundaries of the debonded region. Parts of the rail / joint-bar interface were ambiguous, showing some but not all of the expected signs of debonding. Because of this ambiguity, two different debonded areas (A_s and A_i) were reported for each test specimen, with the Inclusive definition of debonding resulting in areas that were, on average, about 50% larger than the Strict definition.

The experiments described in this thesis were designed under the assumption that the debonded area would be determinable from an inspection of the disassembled joint. They did not address the question of whether the epoxy was in fact debonded in the ambiguous areas. However, it is possible to offer some speculation based on the experimental data.

First, as mentioned in Chapter 2, the ambiguous regions (those included in A_i but not in A_s) generally were adjacent to areas that clearly were debonded. Based on this observation, it is reasonable to conclude that some amount of deterioration had occurred in these regions. Therefore, it is likely that the bond strength in these ambiguous regions was lower than that of a pristine area with no discoloration. When considering the longitudinal strength of the IJ and the likelihood of complete bond failure, the areas included A_i but excluded from A_s probably have some relevance.

The experiments in this thesis, however, did not measure longitudinal bond strength. They measured three things: visible signs of deterioration along the upper edge of the epoxy / insulator layer, elastic deformation of the IJ under small to moderate longitudinal loads, and elastic stiffness of the joint under small to moderate vertical loads. In each case, it was shown that the observed behavior correlated better with A_s than A_i. This suggests that any deterioration of the epoxy bond in the ambiguous areas had relatively little effect on the response of a joint to loads that do not cause complete bond failure.

Longitudinal strength

Because the specimen IJ's were not tested to failure in longitudinal loading, it was not possible to determine the effect of debonding on longitudinal strength. To estimate IJ longitudinal strength based on these experiments, one must make the assumption that the shear strength of each rail / joint-bar interface is proportional to the area of the remaining intact epoxy bond on that interface. The remaining bonded area can be estimated visually from the V_d metric for that interface (Figure 2.6b or 2.6d). If the longitudinal strength of a fully bonded joint is known, the remaining longitudinal strength of each interface can be calculated from the debonded area. The longitudinal strength of the joint overall would be equal to the sum of the strengths of the two weakest interfaces.

Because debonding tends to be approximately equal on the field and gauge sides, the two weakest interfaces will usually lie on the same end of the joint. Therefore, if the debonding is extensive enough to cause a change in the S2 strain coefficient, longitudinal strength can also be estimated using the data in Figure 4.5.

However, given that stress concentrations occur near the edges of the intact epoxy bond (Himebaugh et al. 2007) and at the bolt holes, it might be incorrect to assume that bond strength is directly proportional to bond area. While there is undoubtedly a strong relationship between debonded area and loss of longitudinal strength, the exact relationship requires further study.

Effects of debonding on joint bar cracks

Although cracked joint bars account for a relatively small percentage of IJ failures (Davis et al. 2005), the potentially dangerous consequences of undetected joint bar cracks make them worthy of extra consideration. The relationship between progressive epoxy debonding or complete bond failure and joint bar fatigue cracks is unclear. In a derailment investigated by the National Transportation Safety Board, it was found that both joint bars on a bonded IJ cracked near the endpost after suffering progressive epoxy debonding (NTSB 2005). On the other hand, Li et al. (2006) described a joint bar crack in an IJ that had no obvious signs of debonding.

The experiments described in Chapter 5 showed that the bending stiffness of an IJ decreases as the debonded area increases. A reduction in joint stiffness changes several aspects of an IJ's response to static vertical loads. Lower stiffness leads to increased deflection, which depresses the closest crossties farther into the ballast and causes higher reaction forces at those ties. The increased deflection essentially moves the reaction forces closer to the joint, reducing the effective beam length of the rail and decreasing the bending moment carried by the joint bars. From the point of view of a static load and a Linear Beam On Elastic Foundation (BOEF) model, epoxy debonding is likely to reduce the bending stresses in a joint bar, theoretically slowing fatigue crack growth.

On the other hand, there are other possible effects of debonding on joint bar fatigue damage. The analysis in Chapter 5 suggested that dynamic load factors at an IJ probably increase as the joint loses stiffness, offsetting some or all of the reduction in bending moment due to tie load concentration. If the relative movement between joint

bars and rail increases with debonding, there may also be increased load concentrations on the top and bottom edges of the joint bar, where the rail edge presses into the surface of the bar.

Joint bar cracks and epoxy debonding may also have a non-causal correlation. Fatigue cracks and epoxy debonding may co-occur in part because they are both functions of time, traffic, poor track support, or other factors.

6.2 Future research opportunities

Effect of progressive epoxy debonding on IJ longitudinal strength

Many IJ failures are attributable to complete failure of the epoxy bond under longitudinal tensile forces. It is widely assumed that progressive epoxy debonding reduces the total shear strength of the epoxy bond, making it weaker under such loads. The tools described in Chapters 2 through 4 make it possible to estimate the area of the debonded region. Knowledge of the relationship between debonded area and bond shear strength would make it possible to estimate the ability of an IJ to resist longitudinal loads.

Experiments similar to those described in this thesis could be used to determine the relationship between debonded area and bond strength. Such an experiment would consist of gathering control and test specimens with varying amounts of debonding and applying tensile loads until the rails slip visibly relative to the joint bars.

Because insulated joints with little or no debonding have high longitudinal strength, the tensile test frame and the fixtures used to attach the specimen to the frame

would have to be capable of delivering very high forces, possibly up to 4 MN. If this proves impractical, a direct-shear test such as the one recommended by the American Railway Engineering and Maintenance-Of-Way Association as a "Longitudinal Compression Test (For Qualification Only)" (AREMA 2000b) could be substituted. This test specifies that the IJ be sawed in half through the endpost and each end tested separately. This allows the shear force to be applied in a compression test frame rather than a tension frame, which simplifies the fixtures needed. Because the two rail / joint-bar interfaces with the most debonding generally occur on the same end (Chapter 2), such a test should be a reasonably good substitute for actual tensile loads.

Verification of existing IJ models

In Chapters 3 and 4, references were given to a number of theoretical studies of various aspects of rail joint behavior. Of those reviewed, only three appear to have been supported by physical tests: Jenkins et al. (1974), Cox and Kerr (Cox 1993, Kerr and Cox 1999), and Suzuki et al. (2005). Of these, only Cox and Kerr considered bonded insulated joints, and then only for static loads.

Chapter 3 describes a finite element model that could be used to make predictions of the internal stresses in a bonded IJ under longitudinal loads. This model's internal stress estimates have not been verified. There are also no verified models for either the stresses within the epoxy layer or the dynamic response of the joint under wheel loads. While it would be difficult to measure critical internal stresses like the epoxy shear stress directly, some confidence could be gained if a theoretical model could be shown to

predict measurable quantities such as the strains on external surfaces or the relative displacements of the rails and joint bars. This was done to some extent in the experiments described in Chapter 4, but only for static, longitudinal loads.

Development and verification of models for response of an IJ with progressive debonding

Chapter 3 described a finite element model capable of predicting the effects of debonding on certain deformations in an IJ subjected to longitudinal tensile loads. This is believed to be the only theoretical model of the effects of debonding. In Chapter 5 a simple analytic model is used to draw conclusions about the effect that a loss of stiffness would have on a joint's static deflection, but that model is not sufficient for understanding all the implications of progressive debonding. A verified analytical or numerical model that could predict the effects of debonding on an IJ's dynamic response would yield better predictions of IJ failure. Ideally that model would include the following outputs: stresses near the bolt holes and at the upper and lower edges of the joint bars; loads delivered to the tie plates, cross ties, and ballast; relative displacement of various components under load (which might impact insulator wear rates); and rail-end batter. Even a relatively simple analytical model, similar to the "composite beam" model used for analyzing fully-bonded IJ's by Kerr and Cox (1999), would be an improvement over the "rotational spring" model used in Chapter 5.

A related topic is the effect of localized ballast degradation and settlement on the dynamic behavior of bonded IJ's. Because dynamic loads are higher at joint locations, it can be expected that ballast will degrade faster in the immediate vicinity. Field

investigation to determine the magnitude of this degradation and the effect (if any) on the local stiffness of the substructure would be useful. If in fact the stiffness in the immediate vicinity of the joint varies significantly from that of the surrounding track, this should be incorporated into any IJ models.

Electrical failures

This thesis has focused on the mechanical deterioration of insulated joints and IJ components. However, the most common reason for removing IJ's from service may be inability to reliably prevent electrical interference between adjacent track circuits (Davis et al. 2005). Many electrical failures clearly result from mechanical problems, such as broken bolts or excessive rail-end batter. Many others may not have an obvious direct mechanical cause, but nonetheless occur in joints with extensive debonding or complete bond failure. On the other hand, some railroaders have also observed cases in which joints with little visible debonding or end batter developed electrical problems. It appears that the causes of electrical failure, and the relationship between mechanical deterioration and loss of insulating ability, are complicated and not well understood.

Research on electrical failures is difficult for a number of reasons. First, while it is usually assumed that a drop in IJ resistance results from contact between two steel components that are supposed to be separated, there is no reliable way to detect where this contact occurs. "Sectioning" the joint by cutting it into pieces and checking the resistance within each section is unreliable, as the cutting process is likely to shift the relative positions of the components and eliminate or relocate the contacting region.

Second, removing a joint from track to study it can change the phenomenon being studied. Electrical failure is often intermittent, and may be linked to a particular stress state in the rail or in the joint itself.

These difficulties complicate any effort at post-mortem failure analysis. They do not, however, preclude a statistical study in which electrical failure is compared to various mechanical properties of the joint and the load environment, in order to determine the correlation between certain types of deterioration (such as progressive epoxy debonding) and the likelihood of electrical failure. On the other hand, such a study would be hampered by difficulty in collecting the necessary data. Electrical failures are suspected to begin as intermittent or transient drops in IJ resistance. There are no technologies available at the moment to detect such intermittent problems. Several devices can measure either the total resistance between rail ends, including the path through the ballast (S&C 2008), or the current flowing directly through the joint components (House 2005). However, because these devices cannot be left in place, and because redundancies in the system often prevent IJ electrical problems from causing signal problems, the electrical state of a joint is unknown except at the particular point in time when an inspection is performed.

The situation is similar to trying to study the mechanical deterioration of the joint without having reliable, frequent measurements of the size of the debonded area. A logical next step for research into electrical failures would be the development of a leave-in-place sensor system that could measure insulated joint resistance, or some proxy thereof, without requiring human intervention.

One approach would be to use a high-resistance voltmeter to measure the voltage between the two ends of the joint. IJ's come in pairs. Generally speaking, as the resistance of one of the two IJ's drops, the voltage across the endpost of that joint drops. The voltmeter could be placed in the signal cabinet and connected to the track cables. Assuming that such a device could be designed to avoid interfering with the correct operation of the track circuits, the main research challenge would be identifying the effect of the IJ resistance while filtering out other possible variables that could cause a change in voltage.

6.3 Closing thought

Railroad maintenance is sometimes treated as an ongoing effort to repair or replace defective systems and components that have the potential to disrupt safe and efficient train operation. In recent years, the railroad research community has supplemented this approach by considering ways in which the "stress state of the railroad" can be reduced, reducing the occurrence of damage-causing loads and extending component life.

This newer approach might be beneficial to those considering the economics of various approaches to mitigating IJ-related problems. Projects to improve IJ performance are primarily judged by the resulting increase in IJ service life, and many of the efforts in this area have involved the use of stronger materials or larger components. I believe, however, that consideration ought to be given to the effect of insulated joints on dynamic load factors and track substructure damage. These effects should be considered along with IJ service life in evaluating significantly new designs like the AAR "tapered joint"

(Akhtar and Davis 2006) or support configurations such as suspended versus supported joints.

Based on the results of Chapter 5, it appears that these factors might also be worth considering in the evaluation of IJ's with epoxy debonding. A full analysis of the appropriate replacement schedule for a deteriorating IJ should consider not only the possibility of disruptive failure, but also the near-certainty of increased damage accumulation in the substructure.

REFERENCES

Akhtar, M., and Davis, D. (2006). "Development of an Improved Performance Bonded Insulated Joint for HAL Service," Transportation Technology Center, Inc., Pueblo, CO, Technology Digest TD-06-012.

Akhtar, M., and Davis, D. (2007). "Preliminary Results of Prototype Insulated Joint Tests at FAST," Transportation Technology Center, Inc., Pueblo, CO, Technology Digest TD-07-013.

American Railway Engineering and Maintenance of Way Association (AREMA) (2000a). *2000 Communications & Signals Manual*, Part 8.6.35. The American Railway Engineering and Maintenance of Way Association, Landover, MD, USA.

American Railway Engineering and Maintenance of Way Association (AREMA) (2000b). *2000 Manual for Railway Engineering*, Chapter 4. The American Railway Engineering and Maintenance of Way Association, Landover, MD, USA.

American Railway Engineering Association (AREA) (1980). *Stresses In Railroad Tracks – the Talbot Reports*. AREA, Washington, DC, USA.

Berry, A.; Gibert-Serra, X.; McNew, D.; Nejikovsky, B.; and Tajaddini, A. (2007). "High Speed Joint Bar Inspection Using Advanced Image Collection and Processing Techniques," *Proceedings of the AREMA 2007 Annual Conference*, Chicago, IL, USA.

(CFR 2007a) "Continuous welded rail (CWR); general," *U.S. Code of Federal Regulations* Title 49, Pt. 213.119.

(CFR 2007b) "On-track safety procedures for lone workers," *U.S. Code of Federal Regulations* Title 49, Pt. 214.337.

Chen, Y.C. and Kuang, J.H. (2002). "Contact Stress Variations Near the Insulated Rail Joints," *Proceedings of the Institution of Mechanical Engineers, Part F: Journal of Rail and Rapid Transit*, v 216 n 4, p 265-274.

Cox, J.E. (1993). *Rail Joint Mechanics*, Master's Thesis, Department of Civil Engineering, University of Delaware, Newark, DE, USA.

Davis, D.; Akhtar, M.; Bosshart, J.; Kohake, E.; and O'Connor, T. (2007). "Evaluation of Improved Designs for Bonded Insulated Joints in HAL Service," Transportation Technology Center, Inc., Pueblo, CO, Technology Digest TD-07-020.

Davis, D.; Akhtar, M.; Kohake, E.; and Horizny, K. (2005) "Effects of Heavy Axle Loads on Bonded Insulated Joint Performance," *Proceedings of the AREMA 2005 Annual Conference*, Chicago, IL, USA.

Dukkipati, R.V. and Dong, R. (1999). "The Dynamic Effects of Conventional Freight Car Running Over A Dipped-Joint," *Vehicle System Dynamics*, v 31 n 2, p 95-111.

Hay, W.W. (1982). *Railroad Engineering*, 2nd ed., John Wiley & Sons, New York, NY, USA.

Himebaugh, A.K.; Plaut, R.H.; and Dillard, D.A. (2007) "Finite Element Analysis of Bonded Insulated Rail Joints," *International Journal of Adhesion and Adhesives*, v 28 n 3, p 142-150.

House, M. (2005). "Taking Care of Insulated Joints: Track Maintenance Has a Direct Impact on the Electrical Performance of Insulated Joints, So C&S and M/W Must Work Closely Together," *Railway Track and Structures*, v 101 n 5, p 33-36.

Jenkins, H.H.; Stephenson, J.E.; Clayton, G.A.; Morland, G.W.; and Lyon, D. (1974). "The Effect of Track and Vehicle Parameters on Wheel/Rail Vertical Dynamic Forces," *Railway Engineering Journal* v 3 n 1, p 2-16.

Kabo, E.; Nielsen, J.C.O.; and Ekberg, A. (2006) "Prediction of Dynamic Train-Track Interaction and Subsequent Material Deterioration in the Presence of Insulated Rail Joints," Vehicle System Dynamics, v 44 suppl., p 718-729.

Kerr, A.D. and Cox, J.E. (1999). "Analysis and Tests of Bonded Insulated Rail Joints Subjected to Vertical Wheel Loads," *International Journal of Mechanical Sciences*, v 41 n 10, p 1253-1272.

Kerr, A.D. (2003). *Fundamentals of Railway Track Engineering*, Simmons-Boardman, Omaha, NE, USA.

Li, D.; Meddah, A.; Davis, D.; and Kohake, E. (2006). "Performance of Insulated Joints at Western Mega Site," Transportation Technology Center, Inc., Pueblo, CO, Technology Digest TD-06-28.

National Transportation Safety Board (NTSB 2005). "Derailment of Union Pacific (UP) Freight Train ZLAMN-16 Near Pico Rivera, California, October 16, 2004," Railroad Accident Brief, NTSB Accident No. DCA-05-FR-002.

Nicoli, E.; Dillard, D.A.; Campbell, J.; Dillard, J.; Turner, M.A.; Davis, D.D.; and Akhtar, M. (2007) "Characterizing and Improving Insulated Joints Performance," *Proceedings of the SEM Annual Conference and Exposition on Experimental and Applied Mechanics*, Springfield, MA, USA.

Plaut, R.H.; Lohse-Busch, H.; Eckstein, A.; Lambrecht, S.; and Dillard, D.A. (2007). "Analysis of Tapered, Adhesively Bonded, Insulated Rail Joints," *Proceedings of the Institution of Mechanical Engineers, Part F: Journal of Rail and Rapid Transit*, v 221 n 2, p 195-204.

(S&C 2008). "Insulated Joint Testing," S&C Distribution Company, http://www.sandcco.com/insulatedjointtesting.htm. Modified June 27, 2008; accessed Aug 14, 2008.

Sawadisavi, S.V.; Edwards, J.R.; Resendiz, E.; Hart, J.M.; Barkan, C.P.L; and Ahuja, N. (2008). "Machine-Vision Inspection of Railroad Track." (Paper submitted to the Transportation Research Board 88th Annual Meeting, Washington, DC, USA, 2009.)

Socie, D. and Barkan, C. (2008). "Smart Sensor System for Monitoring Railcar Braking Systems," IDEA Program Final Report, Project HSR-51, Transportation Research Board, National Academies, Washington, DC, USA.

Steenbergen, M. (2006). "Modelling of Wheels and Rail Discontinuities in Dynamic Wheel-Rail Contact Analysis," *Vehicle System Dynamics*, v 44 n 10, p 763-787.

Suzuki, T.; Ishida, M.; Abe, K.; and Koro, K. (2005). "Measurement on Dynamic Behaviour of Track Near Rail Joints and Prediction of Track Settlement," *Quarterly Report of RTRI* v 46 n 2, p 124-9.

Wen, Z.; Jin, X.; and Zhang, W. (2005). "Contact-Impact Stress Analysis of Rail Joint Region Using the Dynamic Finite Element Method, *Wear*, v 285 n 7-8, p 1301-1309.

Winkler, E. (1867). *Die Lehre von der Elasticität und Festigkeit*. H. Dominicus, Prague.

APPENDIX A: DATA AND CALCULATIONS FOR CHAPTER 2

Actual debonding

Extent of epoxy debonding along the nine different measurement lines, in millimeters, starting at the top of the rail / joint-bar interface and moving downwards. This measurement is repeated once for each interface of specimen. The two sides of the specimen are labaled A and B, and the two ends L and R.

Supplier A, Inclusive

Specimen	Interface	Line 1	Line 2	Line 3	Line 4	Line 5	Line 6	Line 7	Line 8	Line 9
TA1	AL	280	280	280	240	30	130	150	170	180
TA1	AR	300	140	110	100	100	100	150	180	190
TA1	BL	30	60	80	90	150	50	60	120	110
TA1	BR	80	80	90	250	340	40	140	190	190
TA2	AL	190	250	250	230	230	250	250	280	300
TA2	AR	410	320	190	170	90	100	100	130	150
TA2	BL	420	360	250	170	170	180	200	220	240
TA2	BR	150	170	180	170	100	120	130	150	190
TA3	AL	210	200	180	160	150	150	230	250	250
TA3	AR	290	300	330	320	270	290	310	330	330
TA3	BL	240	200	180	160	170	170	250	270	270
TA3	BR	330	370	360	300	270	290	360	380	360

Supplier B, Inclusive

Specimen	Interface	Line 1	Line 2	Line 3	Line 4	Line 5	Line 6	Line 7	Line 8	Line 9
TB1	BL	40	40	30	60	40	40	50	90	110
TB1	BR	40	10	0	40	40	30	30	50	80
TB2	BL	60	80	60	60	10	0	10	10	0
TB2	BR	100	110	90	40	10	0	0	0	20
TB3	AL	240	230	230	200	180	250	250	250	280
TB3	AR	230	200	180	120	130	150	180	170	200
TB3	BL	230	200	220	200	200	250	250	270	290
TB3	BR	250	230	150	140	150	170	160	180	200

Supplier A, Strict

Specimen	Interface	Line 1	Line 2	Line 3	Line 4	Line 5	Line 6	Line 7	Line 8	Line 9
TA1	AL	90	60	60	60	30	60	100	130	130
TA1	AR	80	80	100	90	30	60	130	160	200
TA1	BL	60	30	30	50	40	30	40	110	110
TA1	BR	70	70	90	90	80	10	130	180	180
TA2	AL	170	170	170	150	140	120	160	160	160
TA2	AR	110	100	90	60	50	60	70	90	130
TA2	BL	170	180	170	170	130	130	140	150	180
TA2	BR	100	100	100	50	40	50	50	100	150
TA3	AL	210	200	170	160	150	150	180	220	130
TA3	AR	300	290	290	290	270	260	290	330	330
TA3	BL	240	190	170	150	170	170	170	270	250
TA3	BR	460	310	250	260	270	270	270	270	320

Supplier B, Strict

Specimen	Interface	Line 1	Line 2	Line 3	Line 4	Line 5	Line 6	Line 7	Line 8	Line 9
TB1	BL	40	40	10	0	0	30	50	90	110
TB1	BR	10	0	0	0	0	0	30	40	80
TB2	BL	60	60	30	10	0	0	0	10	0
TB2	BR	100	100	0	0	0	0	0	0	0
TB3	AL	230	210	210	170	150	220	240	200	200
TB3	AR	150	130	120	90	90	100	130	120	150
TB3	BL	200	200	200	180	190	200	200	200	200
TB3	BR	130	130	120	100	100	100	130	140	150

The average extent of debonding along the top, center, and bottom portions of the interface are labeled *H*, *W*, and *B*, respectively, and are calculated as follows:

H = (Line 1 + Line 2 + Line 3) / 3

W = (Line 3 + Line 4 + Line 5 + Line 6 + Line 7) / 5

B = (Line 7 + Line 8 + Line 9) / 3

Debonded area is calculated by dividing the interface into eight parallel strips. The first strip is bounded on the top by Line 1 and the bottom by Line 2; the next strip by Line 2 and Line 3, etc.

The debonded area for each strip is measured by calculating the average of the debonding at the top and bottom of the strip, and multiplying by the height given in the following table:

Supplier	1 - 2	2 - 3	3 - 4	4 - 5	5 - 6	6 - 7	7 - 8	8 - 9
A	10	19	25	25	19	19	23	32
B	10	19	25	25	19	19	23	36

So, for instance, the Strict debonded area A_s for the AL interface of specimen TA1 is calculated as $A_s = ((90 + 60) / 2) \times 10 + ((60 + 60) / 2) \times 19 + \ldots + (130 + 130) / 2) \times 32$.

ANOVA tests of debonding distribution

Four specimens (TA1, TA2, TA3, and TB3) had all four rail / joint-bar interfaces available for measurement. First, debonding measurements were converted from area values to proportions:

		Inclusive	
Specimen	Side	End C	End D
TA1	A	0.31	0.24
	B	0.16	0.30
TA2	A	0.33	0.20
	B	0.29	0.19
TA3	A	0.19	0.30
	B	0.20	0.32
TB3	A	0.29	0.20
	B	0.29	0.21

Strict

Specimen	Side	End C	End D
TA1	A	0.23	0.30
	B	0.16	0.31
TA2	A	0.33	0.17
	B	0.33	0.17
TA3	A	0.18	0.32
	B	0.21	0.30
TB3	A	0.32	0.18
	B	0.31	0.19

Both two-factor (End and Side) and one-factor (end only) anaylses were conducted on the four simples individually, then pooled together.

Inclusive, 2-factor

Specimen	SSQ Side	SSQ End	SSQ err
TA1	0.0023	0.0011	0.0111
TA2	0.0006	0.0124	0.0003
TA3	0.0003	0.0132	0.0000
TB3	0.0000	0.0076	0.0000
POOLED	0.0032	0.0342	0.0115

Strict, 2-factor

Specimen	SSQ Side	SSQ End	SSQ err
TA1	0.0010	0.0124	0.0010
TA2	0.0000	0.0266	0.0000
TA3	0.0000	0.0125	0.0004
TB3	0.0000	0.0168	0.0000
POOLED	0.0010	0.0683	0.0015

Inclusive, 1-factor

Specimen	SSQ End	SSQ err
TA1	0.0011	0.0134
TA2	0.0124	0.0009
TA3	0.0132	0.0003
TB3	0.0076	0.0001
POOLED	0.0342	0.0147

Strict, 1-factor		
Specimen	SSQ End	SSQ err
TA1	0.0124	0.0020
TA2	0.0266	0.0000
TA3	0.0125	0.0004
TB3	0.0168	0.0000
POOLED	0.0683	0.0025

Visual inspection confidence intervals

Total debonded area for each joint can be estimated using the equations in Table 2.8. The coefficients in these equations came from simple least-squares fir of the (V_d, A_i) and (V_d, A_s) data to the linear model A_i (or A_s) = $C \times V_d + r$, where r represents the normally-distributed random error. The resulting model estimates and residuals (in mm^2 × 1,000) were:

Specimen	A_i (actual)	A_i (est)	r	A_s (actual)	A_s (est)	r
CA1	0	0	0	0	0	0
CB1	0	0	0	0	0	0
TA1	99	63	37	58	49	10
TA2	134	109	26	79	85	-5
TA3	180	201	-20	160	156	5
TB1	34	46	-12	21	36	-15
TB2	20	24	-3	8	18	-10
TB3	140	14	-2	111	112	-1

The sums of squares of the residuals were 2.62×10^9 mm^4 and 4.58×10^8 mm^4 for A_i and A_s, respectively. Because the linear fit was constrained to pass through the origin, it had only one parameter, and consumed only one degree of freedom. The residual therefore had seven degrees of freedom and the standard deviations were 19,000 and 8,000 mm^2. The critical t value for 80% confidence with 7 degrees of freedom is ±1.415, resulting in confidence intervals of ±1.415 × 19,000 = 27,000 mm^2 for A_i and ±1.415 × 8,000 = 11,000 mm^2 for A_i.

APPENDIX B: DATA AND CALCULATIONS FOR CHAPTER 4

Confidence intervals for revised debonding estimation algorithm

The residuals (in $mm^2 \times 1{,}000$) are calculated from Tables 2.1 and 4.3. The confidence interval is based on the standard deviation of the residuals, as shown:

Specimen	A_i, joint bar strains	A_i, rail gap extension	A_s, joint bar strains	A_s, rail gap extension
CA1	0	10	0	8
CB1	0	0	0	0
TA1	-67	-20	-33	2
TB1	-12	-15	-5	-7
TB2	11	-20	16	-8
TB3	45	50	36	37
TA2	-46	-40	-11	-7
TA3	-14	-26	-30	-42
SSQ	9,124	5,967	3,653	3,355
DOF	5	6	5	6
STDEV	43	32	27	24
$t_{critical}$ for 80%	±1.476	±1.440	±1.476	±1.440
80% interval	±63	±45	±40	±34

Confidence intervals with no knowledge of IJ deformation

For comparison, these confidence intervals were compared to those based only on the mean and standard deviation of the sample data. The sample standard deviation was 71 and 59 $mm^2 \times 1{,}000$ for A_i and A_s, respectively. This has 7 degrees of freedom (8 sample points, minus one to calculate the mean), so $t_{critical} = \pm 1.415$ and the 80% confidence intervals are ±76 and ±55.

APPENDIX C: DATA AND CALCULATIONS FOR CHAPTER 5

Exponential decay curve-fitting and confidence intervals for s_e

The model used for s_e assumed that errors in the model's estimates were normally distributed in the original dataspace:

$$s_e = C_1 e^{-C_2 A} + r$$

Because the errors are not assumed to be normally distributed in logspace, it is not possible to transform the curve-fitting problem into a linear logspace problem. Instead, the curve fitting was done iteratively. The final iteration is shown below, with stiffnesses in kN·m × 1,000 and areas in mm^2 × 1,000.

	Inclusive $C_1 = 15$, $C_2 = 0.0102$		Strict $C_1 = 14.7$, $C_2 = 0.0150$	
	Model est	r	Model est	r
CA1	15.0	1.0	14.7	0.6
CB1	15.0	-0.4	14.7	-0.7
TA1	5.5	-0.8	6.1	-0.2
TB1	10.7	1.1	10.7	1.1
TB2	12.3	-1.4	13.0	-0.7
TB3	3.6	1.7	2.8	0.9
TA2	3.8	-1.1	4.4	-0.5
TA3	2.4	0.1	1.3	-1.0
TB4	0.6	0.6	0.1	0.1
SSQ		9.3		4.6
DOF		6		6
STDEV		1.3		0.9
$t_{critical}$ for 80%		±1.440		±1.440
80% interval		±1.8		±1.3